10.1.3. FSI-PfS-3x (Three-dimensional geometry)

Similar to the flow around a cylinder the flow behind a single truncated cone exhibits a von Kàrmàn vortex street. Several studies (Piccirillo and van Atta, 1993; Narasimhamurthy et al., 2009; Jagadeesh, 2009) describe different vortex shedding frequencies along the cone axis according to the three-dimensional geometry. This leads to a splitting of vorticies (or vortex dislocation) in the wake behind the cone depicted in Fig. 159 and therefore to a complex and fully three-dimensional flow.

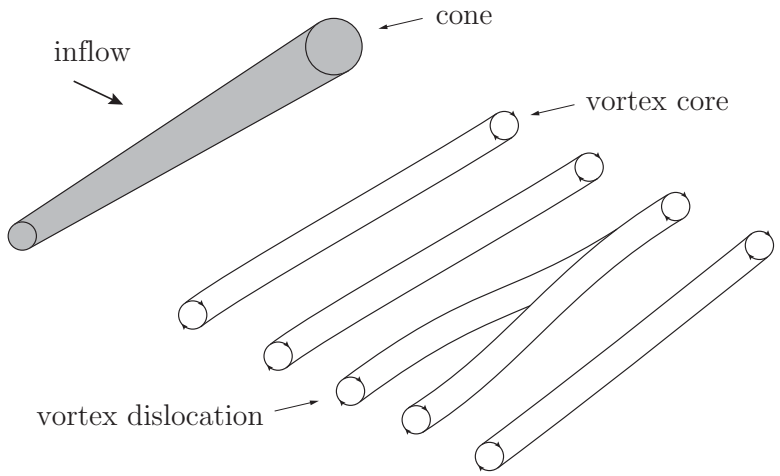

Figure 159: Vortex dislocation in the wake of a cone.

Furthermore, the size of the vorticies are directly depending on the local cone diameter. In the present cases the flexible plate acts like a splitter plate (Anderson and Szewczyk, 1997) and modifies the flow behavior in a significant way. The plate itself and its movement suppresses the different vortex shedding frequencies along the cone leading to only one shedding frequency like in the wake of a cylinder. Nevertheless, the influence of the linearly increasing cone diameter is still present in the flow field. The three-dimensional flow with large vorticies behind the large cone diameter and smaller vorticies on the other side, induces inhomogeneous pressure forces on the flexible plate. Due to the periodic and alternating shedding of vorticies this effect is also time-dependent and generates a quasi-periodic, wavelike three-dimensional deformation of the rubber plate in both investigated test cases. The material used for the flexible plate is an EPDM rubber (FSI-PfS-3a) or a para-rubber (FSI-PfS-3b) which are already applied in FSI-PfS-1a and FSI-PfS-1c as well as in FSI-PfS-2x.

Owing to the three-dimensional deformation of the rubber material within the reference period a more complex phase-averaging procedure (in comparison to the two-dimensional test cases FSI-PfS-1x and 2x) has to be applied for both cone configurations. The first part of the method is similar to the description in Section 7.4.1 (i.e., estimation of neutral points in the $y-$displacement time series, period length detection, calculation of the mean period length, phase-averaging of the x- and y-displacements based on the mean period length, re-sampling of the phase-averaged structural results to 23 equidistant phase angles, sort of the flow field measurements to their corresponding phase angle, phase averaging of the flow fields over equal phase angles). While in the two-dimensional test cases the structural information only in one plane are available, now structural data on the three xy-measuring planes $(z/D)_{\text{large}} = -2.72$,

$(z/D)_{\text{middle}} = 0$ and $(z/D)_{\text{small}} = 2.72$ and the yz-profiles along the line $x/D = 3.13$ are usable. In both cases of FSI-PfS-3x the beginning and end of the reference period is defined by the deflection of the rubber material (the rubber material passes the neutral point) at the large cone diameter at $(z/D)_{\text{large}} = -2.72$. Based on this definition all other structural and flow data are arranged in the reference period. To visualize the three-dimensional shape of the deformed rubber plate, a further post-processing step is necessary. By extra- and interpolating (second-order accurate cubic spline extra- and interpolation method) the structural information (xy-profiles and yz-profiles) the entire structure in its respective deformation state is approximated. This procedure is only valid for deformations of the rubber plate in the first bending mode (present in both test cases), since more complex structural deflections require more xy- and yz-profiles to describe the entire structure. While in x- and y-direction enough data points are delivered from the LLT sensor, in z-direction greater effort would be required to achieve reasonable results for large and/or complex deformed structures[17]. For the present test cases a sufficiently accurate representation of the structural deflection is achieved.
In the following paragraphs the results of the experimental investigations are presented.

FSI-PfS-3a - Structural results

The first test configuration attaches an EPDM rubber to the fixed cone and excites the structure by the flow with an inflow velocity of $u_{\text{inflow}} = 0.969$ m/s. To quantify the structural deformations of the flexible EPDM plate, three measurement points along the trailing edge are chosen. The three points (see Fig. 160) are located at a distance of 2 mm ($x/D = 3.13$) upstream of the extremity of the rubber plate and at $(z/D)_{\text{large}} = -2.72$, $(z/D)_{\text{middle}} = 0$ and $(z/D)_{\text{small}} = 2.72$ in z-direction, respectively.

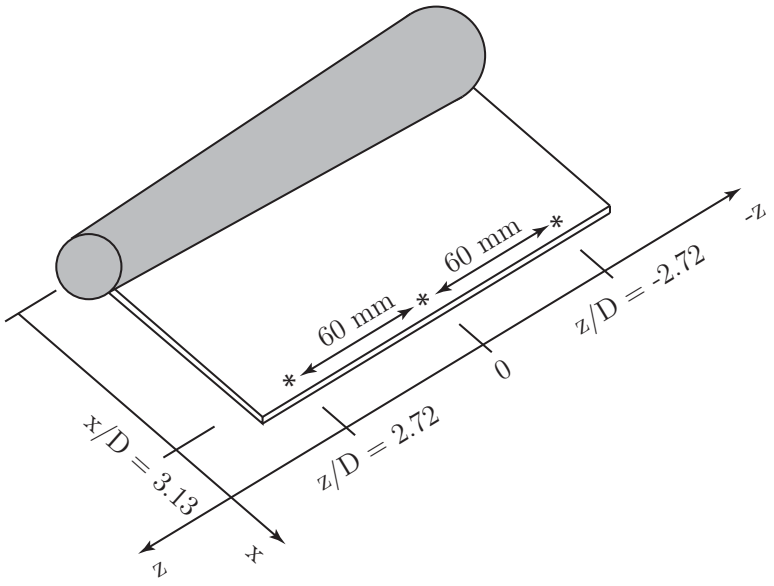

Figure 160: Measurement points of the structural deformations of FSI-PfS-3x.

[17] A stereoscopic measurement system based on high-speed camera recordings could meet the requirements.

In Fig. 161 the average[18] structural response of these three measurement points is presented as a function of the linearly increasing inflow velocity u_{inflow}. The start of the structural deflections is visible at an inflow velocity of $u_{\text{inflow}} = 0.60$ m/s. From the very beginning a strong three-dimensional deformation of the structure is observed. The deflections at $(z/D)_{\text{large}} = -2.72$ (downstream of the large cone diameter) are large, while the deflections behind the medium and small cone diameters reach smaller maximum displacements. This trend is present over a wide range of inflow velocities and responsible for the three-dimensional deformation of the rubber plate. With increasing inflow velocities the deflections also increase till $u_{\text{inflow}} = 0.90$ m/s to values of $(y/D)_{\text{large}} = \pm 0.59$, $(y/D)_{\text{middle}} = \pm 0.51$ and $(y/D)_{\text{small}} = \pm 0.37$. In the further course the deflections at $(z/D)_{\text{large}}$ and $(z/D)_{\text{middle}}$ continuously increase till $u_{\text{inflow}} = 1.85$ m/s to values of $(y/D)_{\text{large}} = \pm 0.74$ and $(y/D)_{\text{middle}} = \pm 0.66$, while the displacements at $(z/D)_{\text{small}}$ decrease to $(y/D)_{\text{small}} = \pm 0.30$. A transition phase between $u_{\text{inflow}} = 1.85$ m/s and $u_{\text{inflow}} = 2.10$ m/s is characterized by highly fluctuating amplitudes of the maximum and minimum structural displacements. At about $u_{\text{inflow}} = 2.10$ m/s the previously symmetrical movement turns into an asymmetric state. Here, the entire flexible structure is locked at one side behind the cone and does not move back to the opposite side. Due to this state the oscillatory motion is almost stopped. The investigations show that this process takes place arbitrarily on both sides independent on the accelerating or decelerating inflow velocities.

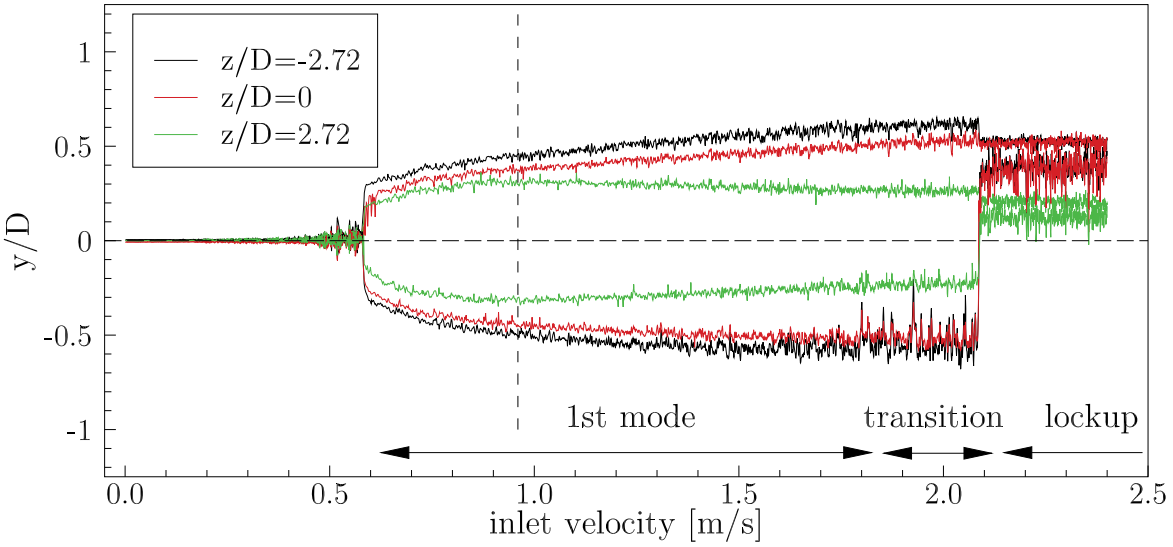

Figure 161: FSI-PfS-3*a*: Averaged maximal/minimal structural deflections as a function of the inflow velocity.

In addition to the displacement response (Fig. 161) to the inflow velocity, in Fig. 162 the corresponding frequency response is presented. The fluid-structure interaction starts at $u_{\text{inflow}} = 0.60$ m/s with an oscillation frequency of $f = 4.08$ Hz (St = 0.15) and increases linearly until the beginning of the irregular lockup effect at $u_{\text{inflow}} = 2.10$ m/s with a frequency of $f = 11.51$ Hz (St = 0.12) representing a frequency gradient of $\delta f/\delta u = 4.95$ Hz/(m s^{-1}). Similar to the displacements the fluctuation level of the frequency also increases with u_{inflow},

[18] Based on 10 measurement series.

especially in the transition region beyond $u_{\text{inflow}} > 1.85$ m/s. Since the first eigenfrequency of the entire structure $f_{3a,1st} = 19.00$ Hz (calculated in Section 8.3) is found to be much larger than the measured swiveling frequencies, a resonance-induced mode transition does not take place. In Fig. 163 several characteristic moments of the structural deformations at several inflow velocities are illustrated. The snapshots depict the three-dimensional deformations of the rubber plate.

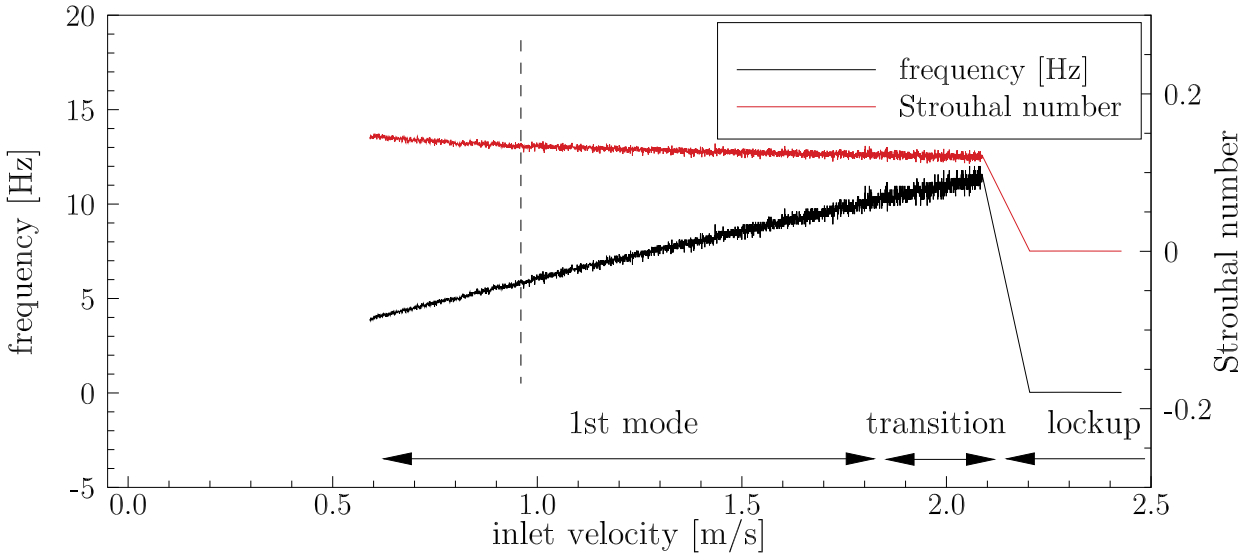

Figure 162: FSI-PfS-3*a*: Averaged frequency and Strouhal number as a function of the inflow velocity.

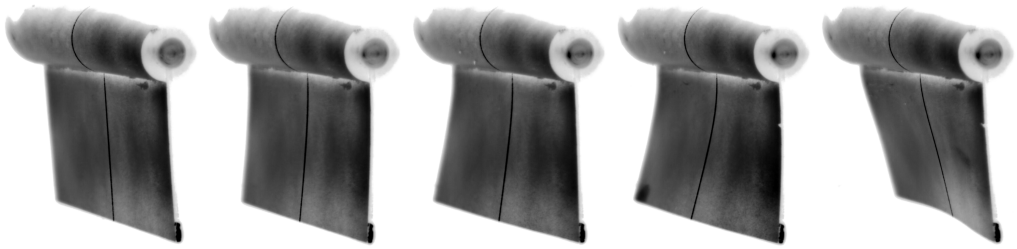

Figure 163: FSI-PfS-3*a*: Characteristic moments of the structure deformation at several inflow velocities.

The final inflow velocity of $u_{\text{inflow}} = 0.969$ m/s for this test case is chosen owing to the moderate quasi-periodic displacements at all three measurement planes and their corresponding low fluctuation levels. In Fig. 164 the displacements of the structure within a time interval of one second (raw data) are presented. The plot is based on the displacements of three measurement points at the surface of the rubber plate introduced in Fig. 160.

The three time histories of the displacements reveal cycle-to-cycle variations regarding the displacement amplitude and the swiveling frequency. Furthermore, the phase shift mentioned above is clearly visible. The structure at the large cone diameter is leading the structural motion. The structure in the middle of the domain follows with a phase shift of about 10

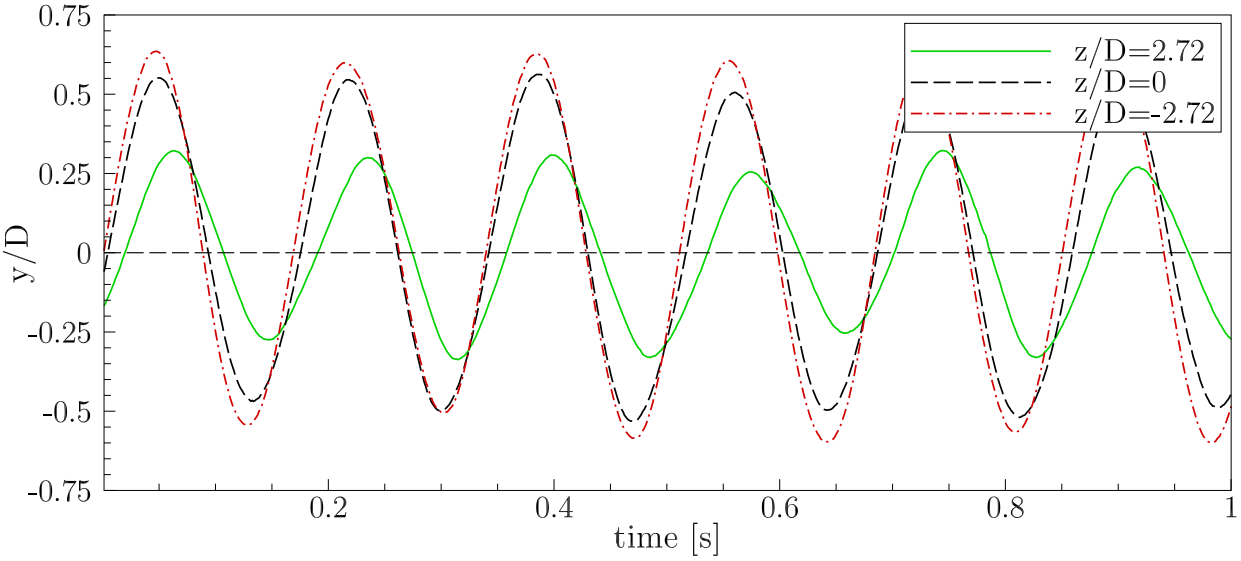

Figure 164: FSI-PfS-3*a*: Experimental structural results: Time history of the structural deflections (extract) for the three measurement points at $x/D = 3.13$ at the measurement planes $(z/D)_{\text{large}} = -2.72$, $(z/D)_{\text{middle}} = 0$ and $(z/D)_{\text{small}} = 2.72$.

degrees. Finally, the structure at the small diameter reaches the same state with a phase delay of about 33 degrees with respect to the large diameter. That means that the deformation velocity in spanwise direction is not constant. It can be assumed that the strong forces towards the large cone diameter quickly overcome the deformation resistance of the rubber plate, while the forces decrease towards the small cone diameter and the resulting deformation velocity slows down.

In order to allow a quantitative comparison between the experimental results and numerical data, all results are phase-averaged as explained in the introduction of this section. The results for the structure are presented in Fig. 165 for the three measurement points and in Fig. 166 for the entire spanwise line along the extremity. Based on the phase-averaged period of the deflections depicted in Fig. 165 the phase shift between the different planes is even more clearly visible. As already mentioned the phase difference between the small and the middle diameter is significantly larger than between the middle and the large diameter. Furthermore, also the amplitudes visibly differ between the small and the middle diameter compared to the middle and the large diameter.

The mean extrema of the displacements at the three measurement points along the truncated cone are presented in Table 20. For each measuring point on the surface of the flexible plate the displacements are nearly symmetric. The remaining deviations from symmetry are most likely caused by the slightly anisotropic material behavior of the rubber and asymmetries in the clamping of the flexible structure in the front body. The deflections are found to be large at $(z/D)_{\text{large}} = -2.72$ and decrease towards the small cone diameter, while their standard deviations increase, respectively. The frequency of the FSI phenomenon, i.e., the frequency of the y-displacements, is about $f = 5.77$ Hz, $\sigma(f = 0.12\ (2.08\%))$ which corresponds to Strouhal numbers of $\text{St}_{\text{large}} \approx 0.20$, $\text{St}_{\text{middle}} \approx 0.17$ and $\text{St}_{\text{small}} \approx 0.13$, respectively.

In Fig. 166 the phase-averaged deflections along the entire line at $x/D = 3.13$ close to the

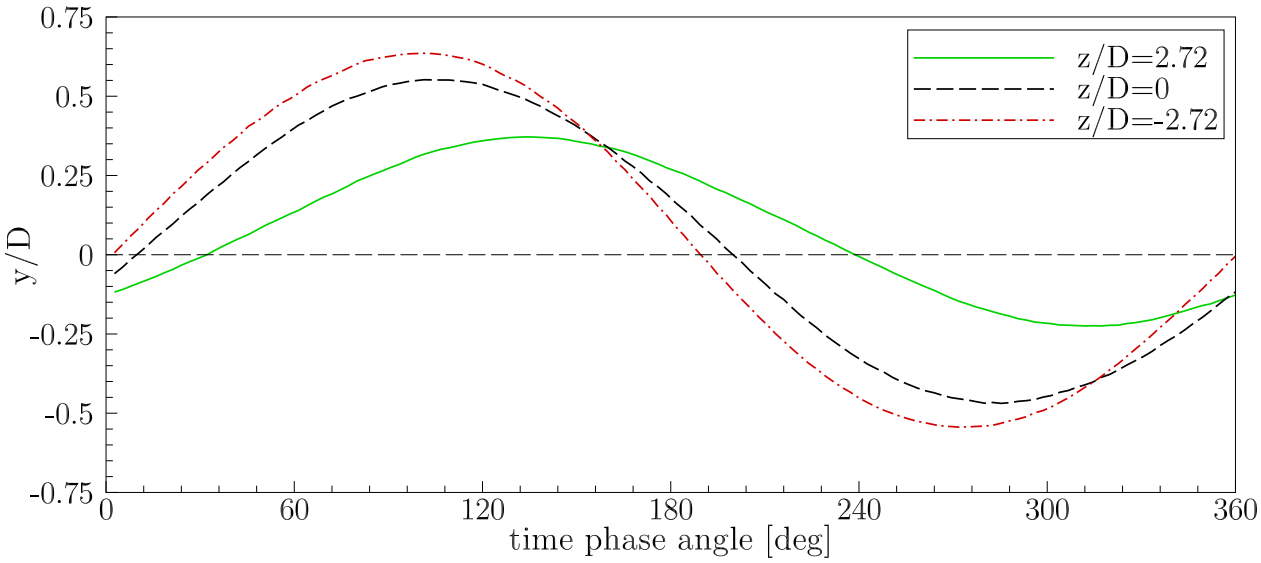

Figure 165: FSI-PfS-3*a*: Experimental structural results: Phase-averaged reference period of the structural deflections at the three measurement points at $x/D = 3.13$.

plane	$(y/D)_{\max}$ large	$(y/D)_{\min}$ large	$(y/D)_{\max}$ middle	$(y/D)_{\min}$ middle	$(y/D)_{\max}$ small	$(y/D)_{\min}$ small
y-displacement	0.538	−0.540	0.462	−0.459	0.227	−0.221
standard deviation σ	0.0387 (7.16%)	0.0378 (7.00%)	0.0283 (6.13%)	0.0305 (6.65%)	0.0275 (12.11%)	0.0330 (14.93%)

Table 20: FSI-PfS-3*a*: Measured mean y-displacements y/D and their corresponding standard deviations σ at the three measurement points at $x/D = 3.13$.

extremity illustrate the three-dimensional deformation of the rubber plate within the reference period. At a phase angle of 16 degree the deflections are small all over the rubber plate. During the further movement until 78 degree the displacements at the larger diameter nearly reach their maximum, where in positive z/D-direction (small cone diameter) only small deflections are noticeable. This part catches up at the phase angle shown for 141 degree, where the displacements on the extremity are almost constant in z-direction. The following phase angles depict similar states of the structure movement in the opposite direction.

FSI-PfS-3a - Flow field

In Fig. 167 the time-averaged flow fields at the three planes at $z/D = -2.72$, $z/D = 0$ and $z/D = 2.72$ are shown. In all three flow fields the characteristic physical phenomena (a stagnation point in front of the cone, acceleration areas on the upper and lower side of the structure, shear layers evolving out of the separated boundary layers, a recirculation area downstream of the cone and a broad wake area behind the structure) are found. By comparing all three planes to each other, it is noticeable that there is a tendency regarding the scales from the large to the small side of the cone. This tendency is visible, i.e., for the acceleration areas which are larger at the plane $z/D = -2.72$ than at the planes at $z/D = 0$ and $z/D = 2.72$. The wake downstream of the structure has an y-expansion of about $4 \cdot D$ at $z/D = -2.72$,

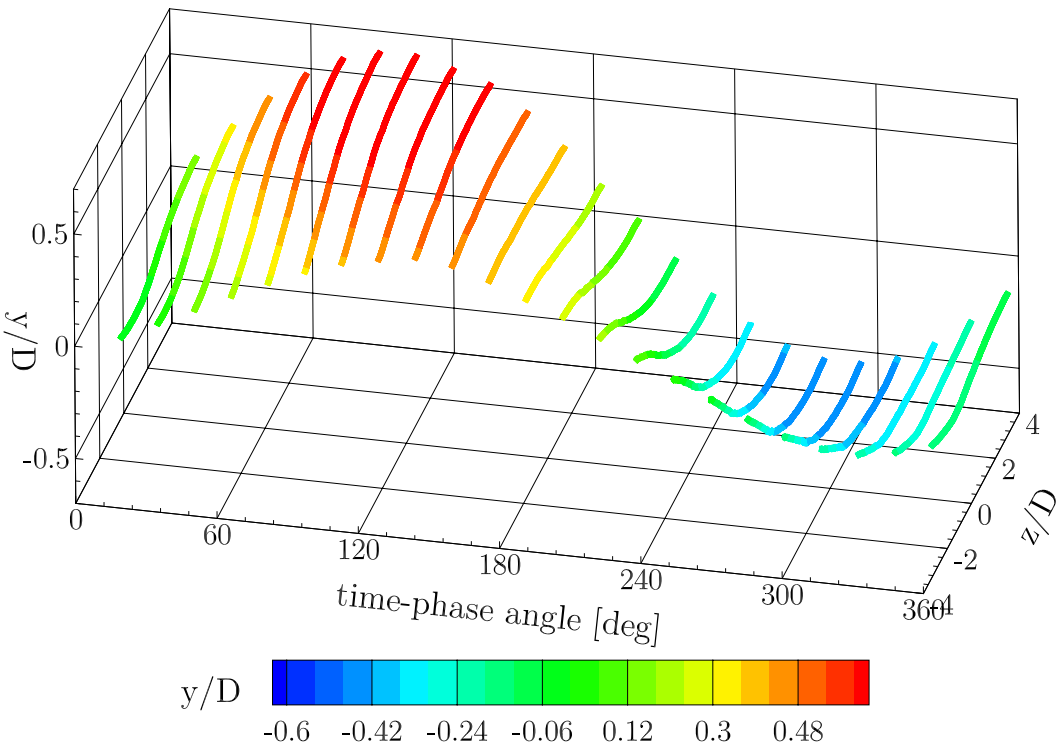

Figure 166: FSI-PfS-3a: Phase-averaged structural results for the reference period; entire line close to the extremity of the flexible structure at $x/D = 3.13$.

$3 \cdot D$ at $z/D = 0$ and $1.5 \cdot D$ at $z/D = 2.72$, respectively. However, it can be assumed that flow is not linearly distributed between the three measurement planes. In comparison to the mean results of the rigid configuration (see Section 8.1.2) only minor deviations are found. That means that the mean flow (including all mentioned phenomena) is rather unaffected by the motion of the flexible plate. Compared to the two-dimensional test cases FSI-PfS-1x and 2x the influence of the increased front body diameter is visible. Close to the small end of the cone at $z/D = 2.72$ the ratio between the plate length and the front body cylinder is almost equal to the cylindrical configuration ($l/D_{\text{small}} = 2.45$ for FSI-PfS-3a in comparison to $l/D = 2.73$ for FSI-PfS-1x and 2x). Here, the large differences in the time-averaged flow (reduced wake expansion and acceleration areas) can be explained by the decreased inflow velocity of FSI-PfS-3a. More similar to the mean velocity distribution of FSI-PfS-1x or 2x is the time-averaged flow in the midplane of the channel at $z/D = 0$. Apparently, the increased front-body cylinder ($D_{\text{middle}} = 1.25 \cdot D$) of FSI-PfS-3$a$ compensate the lower inflow velocity.

A selection of phase-averaged flow fields is depicted in Figs. 168 and 169. These six states of the mean period of the FSI problem illustrate the significant three-dimensional characteristics of the flow. The shed vorticies are convected downstream leading to an alternating vortex pattern in the wake of the structure. In the wake the characteristic recirculation areas are observed. Finally, the shed vorticies leave the region of interest. All planes ($(z/D)_{\text{large}} = -2.72$, $(z/D)_{\text{middle}} = 0$ and $(z/D)_{\text{small}} = 2.72$) at a single phase angle show the distinctive behavior of these vortical structures. Nevertheless, compared to each other the three planes differ in the size of the vorticies and the area of the wake influenced. The shed vortex at the plane $(z/D)_{\text{large}} = -2.72$ is much larger in size and velocity magnitude than on the plane

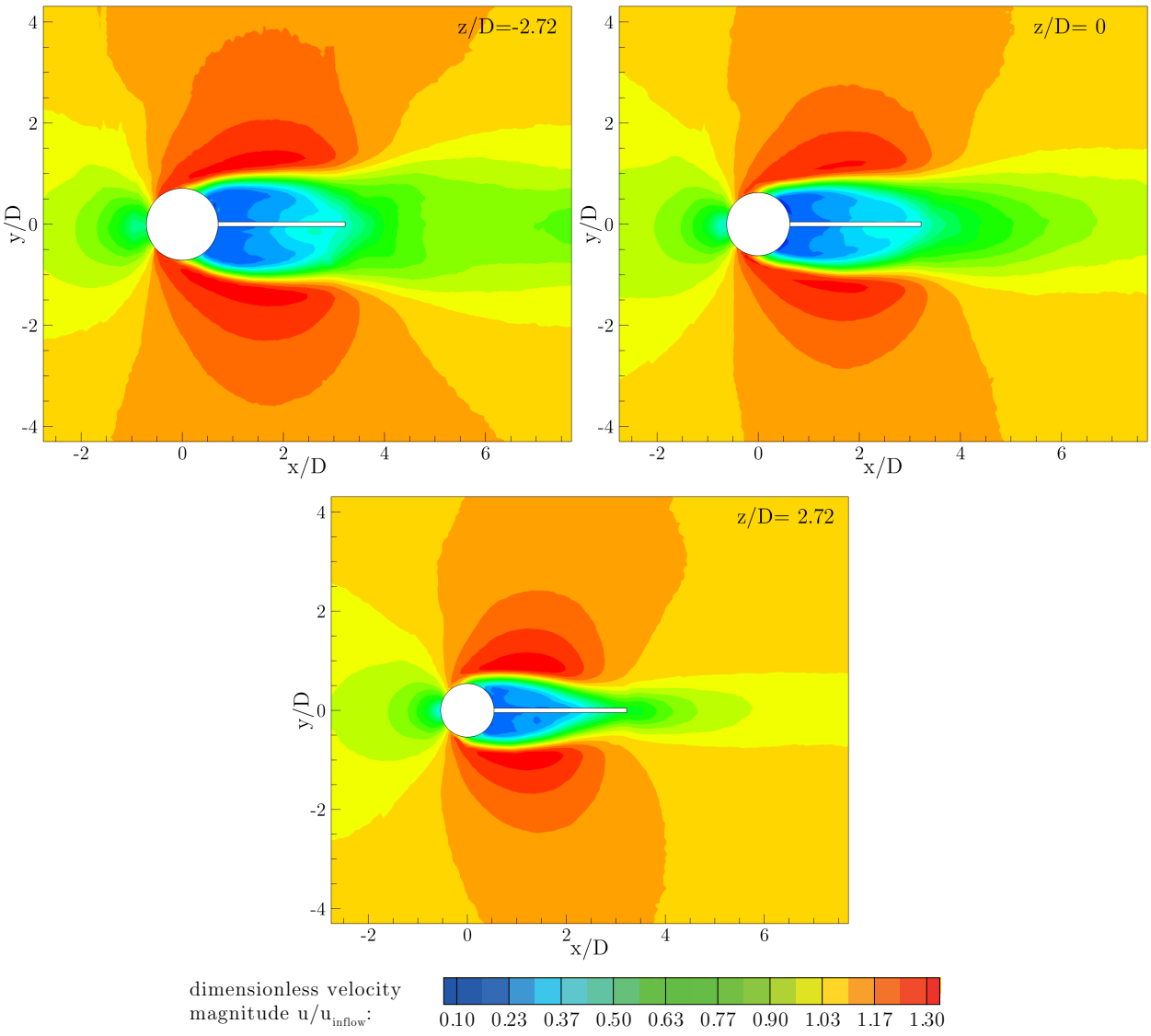

Figure 167: FSI-PfS-3a: Experimental flow and structural results, time-averaged over all measured periods at the three measurement planes $z/D = -2.72$, 0 and 2.72.

$(z/D)_{\text{small}} = 2.72$. Also the mentioned phase shift between the large and the small cone diameter is visible due to the staggered location of the vortex centers.
In the first picture at a phase angle of 16 deg the EPDM rubber plate is nearly in its initial position. The lateral sides of the plate appear slightly shifted since the small end is located in the positive y-direction while the large end points are shifted in the negative y-direction. At this phase angle the acceleration areas located in the positive y-direction have a large expansion and strongly grow, while in the negative y-direction only small acceleration areas and a previously shed vortex are observed. During the phase interval until the next picture at 78 deg the entire rubber plate moves in the positive y-direction and reaches its maximal deflection at the planes $z/D = -2.72$ and $z/D = 0$. Here, the deflections downstream of the large cone diameter are larger than the deflections in the midplane at $z/D = 0$. Due to the phase delay the extremity at $z/D = 2.72$ reaches its maxima about 33 deg later and the value is significantly smaller. In the phase interval between 78 deg to 141 deg the structure moves

back in the opposite (negative y-) direction and a vortex is shed from the cone in the positive y-direction visible in the measurement planes $z/D = -2.72$ and $z/D = 0$, while at $z/D = 2.72$ the shed vortex is first visible at the picture of 203 deg. At the passage of the extremity at $z/D = -2.72$ of the neutral line at $y/D = 0$ the first half of the phase-averaged period is over. Within the following half period the flow including the pressure forces and the resulting structural deformations are reversed with respect to the first half of the period. The presented flow measurements indicate that a fully three-dimensional expanded vortex street is formed downstream of the structure.

The volumetric flow results based on the V3V measurements support the assumption of a fully three-dimensional flow. The spatial restriction of the V3V system allows an analyzable flow volume of $x/D = 3.20$ to 9.40, $y/D = -3.55$ to 3.55 and $z/D = -2.86$ to 2.95. That means the flow regions, in which the flexible structure oscillates and its lateral sides, are not included. In Fig. 170 the phase-averaged result at the phase angle of $\phi = 313$ deg is presented for two different perspectives. The iso-surfaces depict the velocity magnitude at $u/u_{\text{inflow}} = 0.79$ showing two shed vorticies downstream of the flexible plate. While in the two-dimensional test cases the shed vorticies are almost equally expanded in z-direction, now a contraction from the large cone to the small cone diameter can be observed. Furthermore, this effect increases with the distance to the structure as the vortex near the structure is only slightly contracted, while the vortex further downstream shows a significant three-dimensional expansion. It can be assumed that the linearly increasing velocity distribution in z-direction is responsible for this phenomenon. Furthermore, a vortex dislocation (refer to the explanation in Section 6.3.3) as reported in the studies of Piccirillo and van Atta (1993), Narasimhamurthy et al. (2009) and Jagadeesh (2009) is not observed downstream of the cone. It can assumed that the rubber plate still acts like a splitter plate and alters the flow to an uniform vortex shedding frequency in spanwise direction. That means the discrete steps in the vortex shedding frequency are hindered and the generated vorticies are expanded but inclined all over the spanwise expansion of the cone. An indication that the three-dimensional geometry still has an enormous effect on the system is obvious from the phase delay in the structural motion and the fluid flow (i.e., the moment of the vortex shedding differs in time along the z-direction).

The POD analysis for this test case is carried out based on the PIV measurements in the midplane ($z/D = 0$) of the channel. Figures 171a and b correspond to the kinetic energy of the streamwise velocity u, while the cross-flow velocity component v is presented in Figs. 171c and d. The analysis shows that the energy rises in the areas, where the vorticies detach from the cone and form the antisymmetric pattern according to the alternating vortex shedding at the bluff body. In comparison to the fixed configuration the kinetic energy is now more concentrated in the vicinity of the moving plate. This is proved by the POD analysis based on the vorticity (Figs. 171e and f). Here, the energy levels at all relevant flow structures rise due to the increased disturbances of the FSI coupling.

The quantitative analysis of the POD reveals a strong decrease of the kinetic energy from the large cone diameter to its small end. While the entire kinetic energy is calculated to $k_{\text{abs,all,large}} = 934.30$ m^2/s^2 ($k_{\text{rel,all,large}} = 100\%$) at $(z/D)_{\text{large}} = -2.72$, the kinetic energy at $(z/D)_{\text{small}} = 2.72$ yields only a sixth with $k_{\text{abs,all,small}} = 147.23$ m^2/s^2 ($k_{\text{rel,all,small}} = 100\%$). In the midplane at $(z/D)_{\text{middle}} = 0$ the kinetic energy amounts $k_{\text{abs,all,middle}} = 595.11$ m^2/s^2

($k_{\mathrm{rel,all,middle}} = 100\%$). Similar to the two-dimensional test cases the first two POD modes contain most of the kinetic energy. In the case of FSI-PfS-3a the first two modes stores together 72.37% ($(z/D)_{\mathrm{large}} = -2.72$), 59.62% ($(z/D)_{\mathrm{middle}} = 0$) and 34.57% ($(z/D)_{\mathrm{small}} = 2.72$) of its corresponding total energy content.

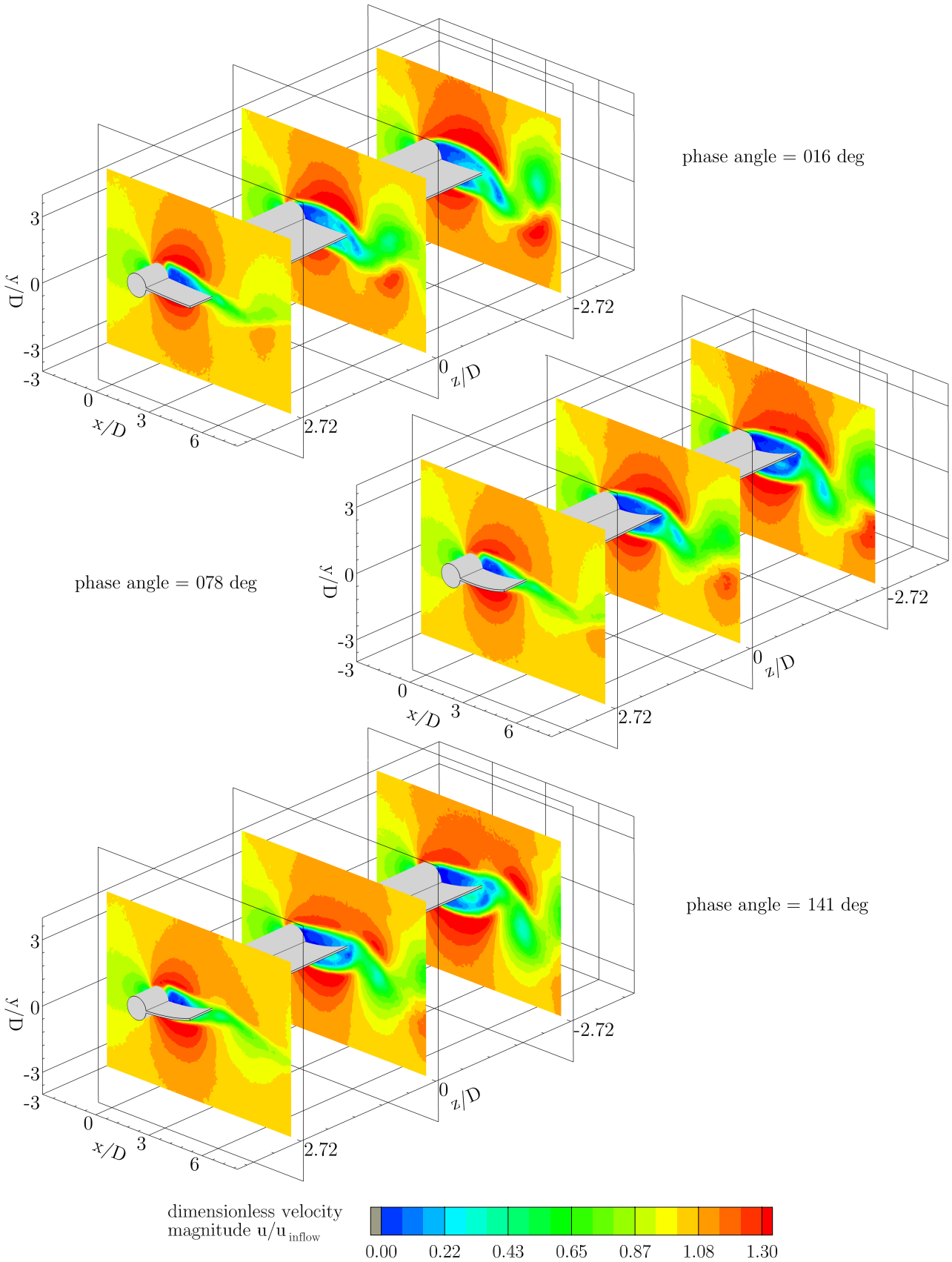

Figure 168: FSI-PfS-3*a*: Experimental phase-averaged flow and structural results for the first half of the reference period at three measurement planes at $(z/D)_{\text{large}} = -2.72$, $(z/D)_{\text{middle}} = 0$ and $(z/D)_{\text{small}} = 2.72$.

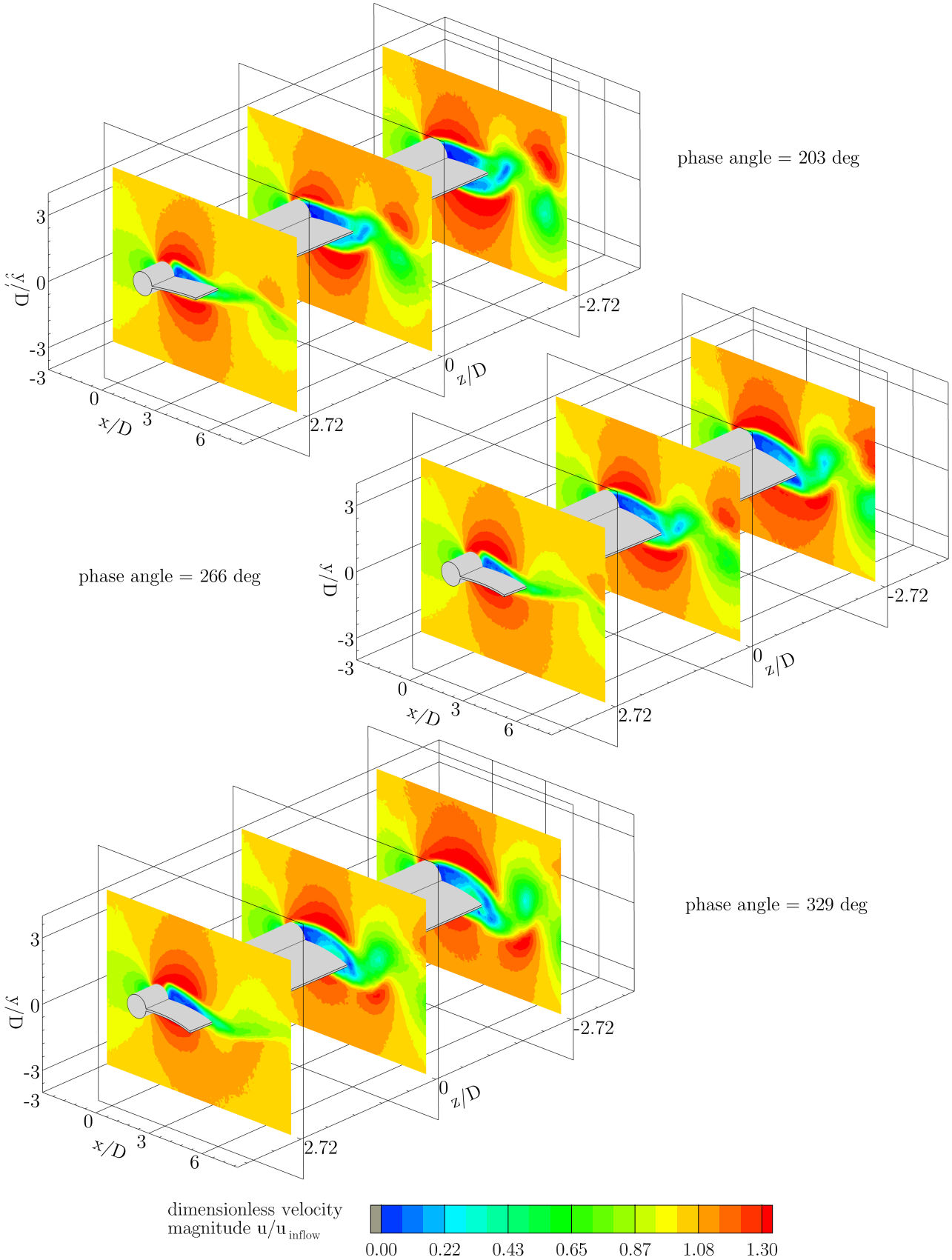

Figure 169: FSI-PfS-3*a*: Experimental phase-averaged flow and structural results for the second half of the reference period at three measurement planes at $(z/D)_{\text{large}} = -2.72$, $(z/D)_{\text{middle}} = 0$ and $(z/D)_{\text{small}} = 2.72$.

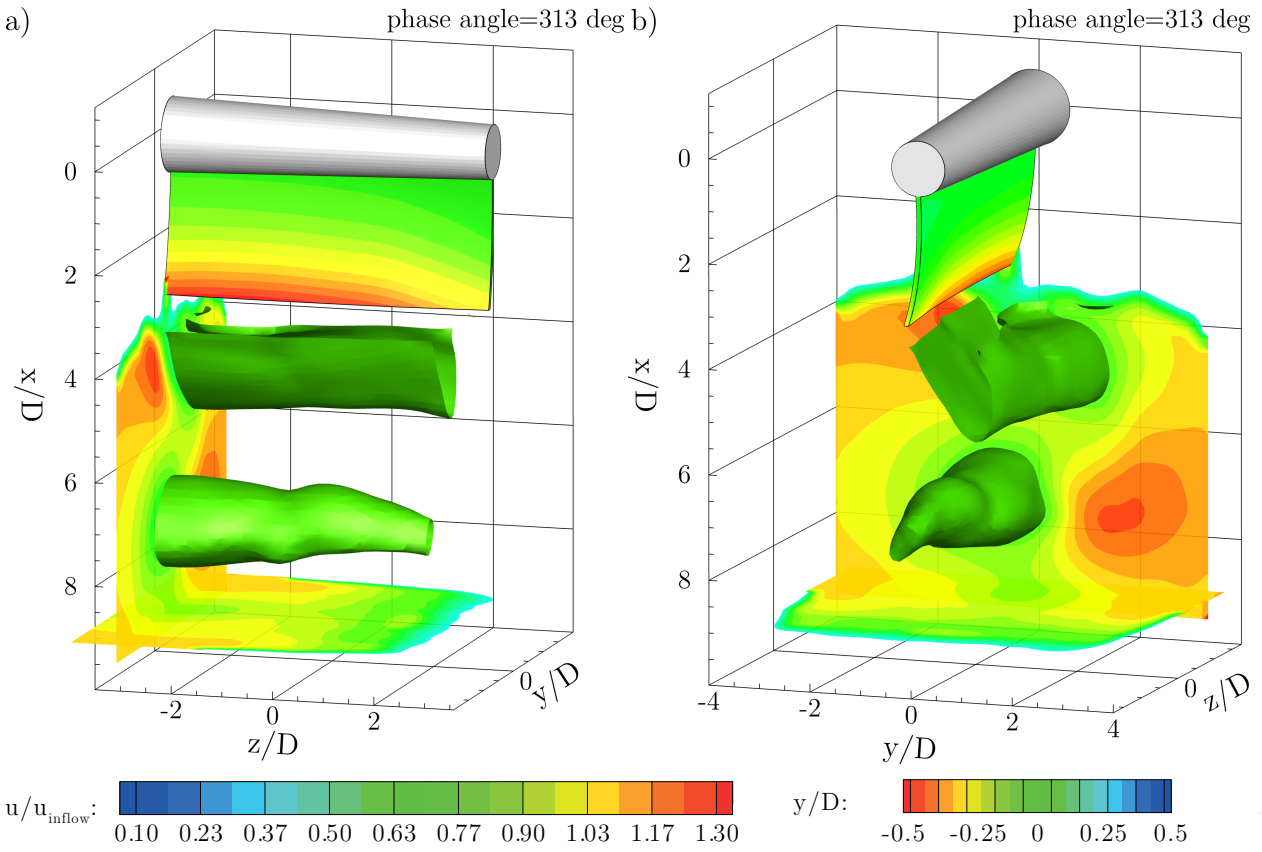

Figure 170: FSI-PfS-3*a*: Experimental flow results (velocity magnitude) based on the V3V system and the structural results (extra- and interpolated), phase-averaged data at the phase angle of $\phi = 313$ deg, iso-surfaces depict the velocity magnitude at $u/u_{\text{inflow}} = 0.79$.

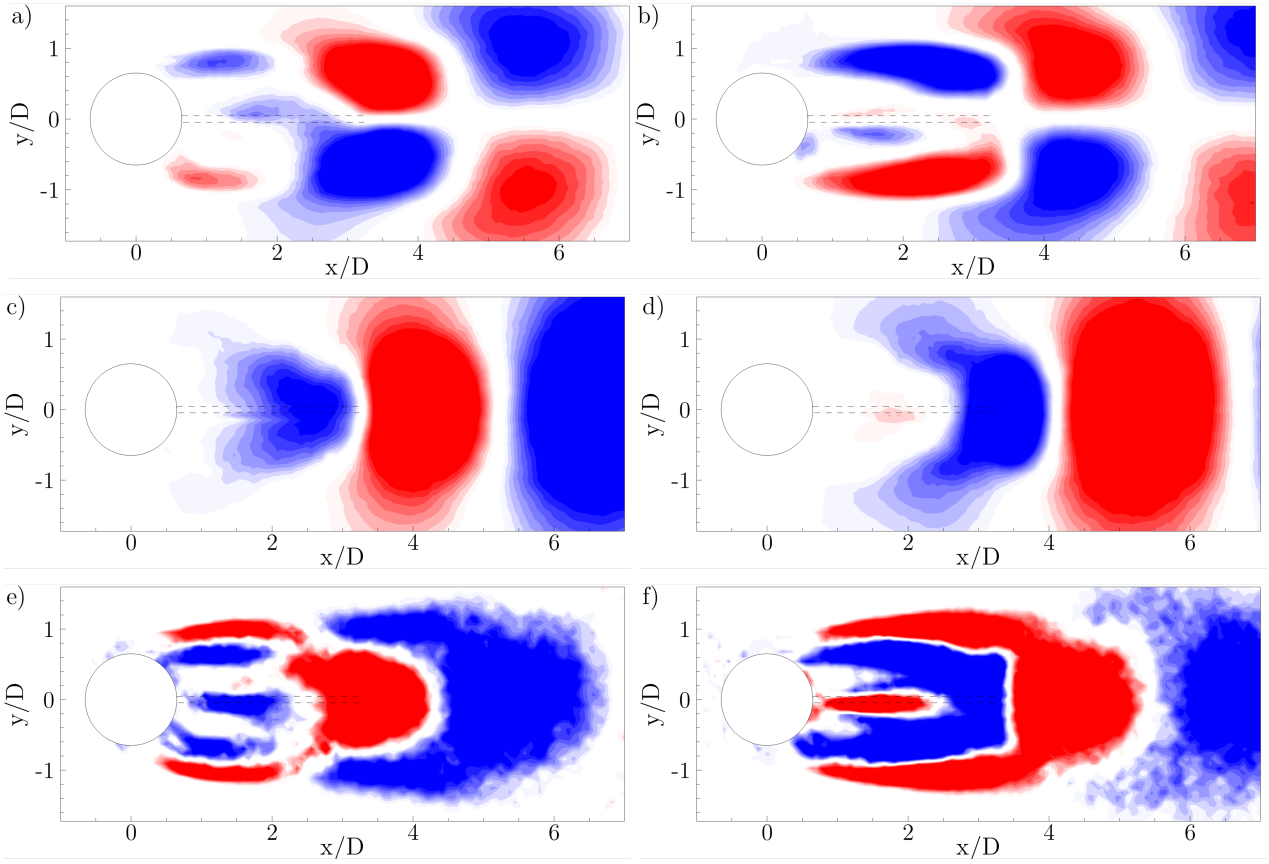

Figure 171: FSI-PfS-3*a*: POD analysis of the two-dimensional flow fields in the midplane ($z/D = 0$): a) velocity component u, first mode; b) velocity component u, second mode; c) velocity component v, first mode; d) velocity component v, second mode; e) vorticity component ω_z, first mode; f) vorticity component ω_z, second mode.

FSI-PfS-3b - Structural results

In the second three-dimensional test case FSI-PfS-3*b* the soft para-rubber plate is attached to the cone and the inflow velocity is reduced to 0.549 m/s, which will be motivated below.
In Fig. 172 the maximal and minimal deflections at $(z/D)_{\text{large}} = -2.72$, $(z/D)_{\text{middle}} = 0$ and $(z/D)_{\text{small}} = 2.72$ (all at $x/D = 3.13$, refer to Fig. 160) are plotted as a function of the inflow velocity (averaged results based on a series of 10 single measurements). Beyond an inflow velocity of $u_{\text{inflow}} = 0.15$ m/s the interaction between the structure and the fluid starts with tiny displacements all over the flexible plate. Till $u_{\text{inflow}} = 0.24$ m/s a strong increase in the peak deflections at all three points is noticeable. Even during this short initial phase significant differences of the displacements between the three measurement positions are visible. As assumed the deflections at $z/D = 2.72$ (small cone diameter) are smaller than those present at $z/D = 0$ and $z/D = -2.72$. The largest deflections are reached at $z/D = -2.72$ (large cone diameter). This increasing deformation behavior along the z-elongation from the small to the large cone diameter is typical for this test case. In the limited range of inflow velocities up to $u_{\text{inflow}} = 0.83$ m/s the maximal and minimal peaks increase continuously to values of $(y/D)_{\text{small}} = \pm 0.29$, $(y/D)_{\text{middle}} = \pm 0.57$ and $(y/D)_{\text{large}} = \pm 0.71$. Beyond $u_{\text{inflow}} = 0.83$ m/s the oscillation switches from a quasi-periodic to an irregular behavior characterized by chaotic three-dimensional deformations of the rubber plate (see Fig. 174). While in the quasi-periodic state until $u_{\text{inflow}} = 0.83$ m/s a deformation of the rubber plate similar to the motion of FSI-PfS-3*a* is present, in the irregular phase an uncorrelated deformation along the trailing edge is observable. At an inflow velocity of $u_{\text{inflow}} = 1.25$ m/s the structural deflections are dominated by the flow. The deflections decrease to $|(y/D)_{\text{small}}| < 0.22$, $|(y/D)_{\text{middle}}| < 0.39$ and $|(y/D)_{\text{large}}| < 0.50$ and are highly unsteady.

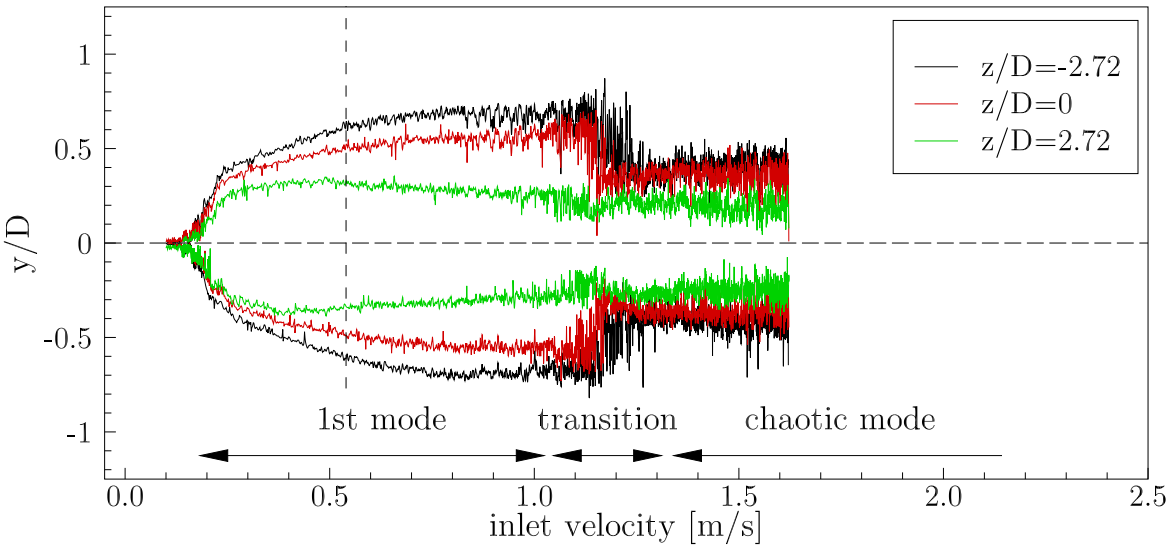

Figure 172: FSI-PfS-3*b*: Averaged maximal/minimal structural deflections as a function of the inflow velocity.

In Fig. 173 the oscillation frequency distribution over the inflow velocity range from $u_{\text{inflow}} = 0$ m/s to 1.63 m/s is depicted. The fluid-structure interaction begins at an oscillation fre-

quency of $f = 1.15$ Hz (St $= 0.168$) at $u_{\text{inflow}} = 0.15$ m/s. Up to $u_{\text{inflow}} = 0.83$ m/s the frequency increases linearly with the velocity ($\delta f / \delta u = 4.84$ Hz/(m s^{-1})). With the beginning of the transition phase the frequency continues to increase linearly but higher fluctuations are noticed. The transition to the irregular mode is visible at $u_{\text{inflow}} = 1.15$ m/s. The frequency of $f = 5.48$ Hz is followed by a large increase of the frequency accompanied by high fluctuations. After the transition the frequencies are almost doubled (i.e., $f = 13.07$ Hz at $u_{\text{inflow}} = 1.36$ m/s) but the fluctuations remain on a high chaotic level. In contrast to FSI-PfS-3*a* the first eigenfrequency $f_{3b,1st} = 9.42$ Hz (refer to Section 8.3) of the entire structure is reached in the transition regime. Due to the high fluctuations there and in the following state, no proven statement whether this transition is resonance-induced or just affected by the flow can be made.

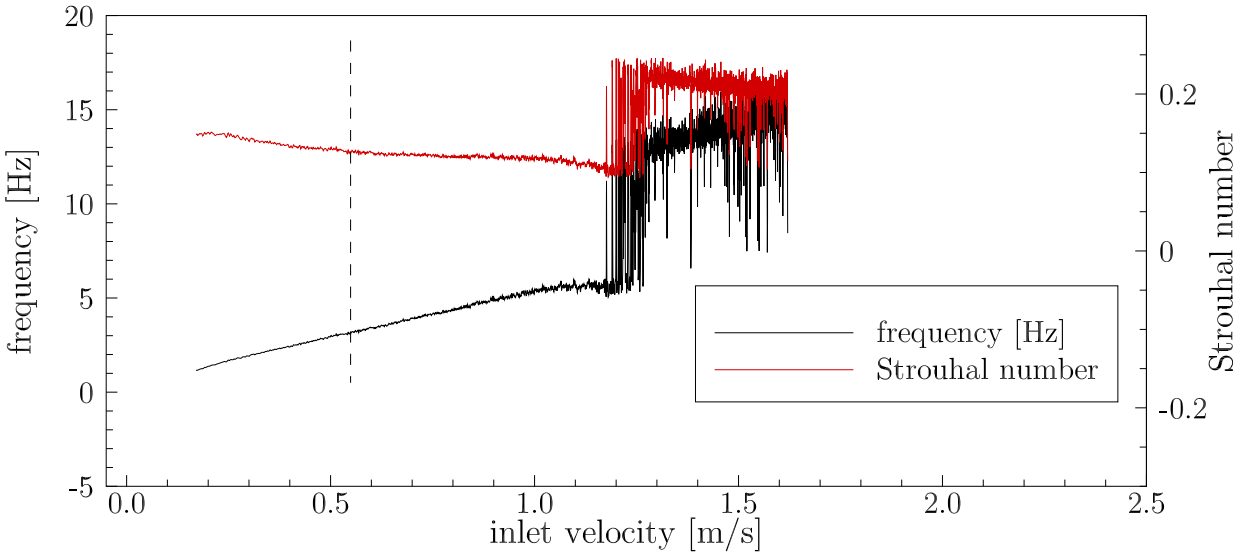

Figure 173: FSI-PfS-3*b*: Averaged frequency and Strouhal number as a function of the inflow velocity.

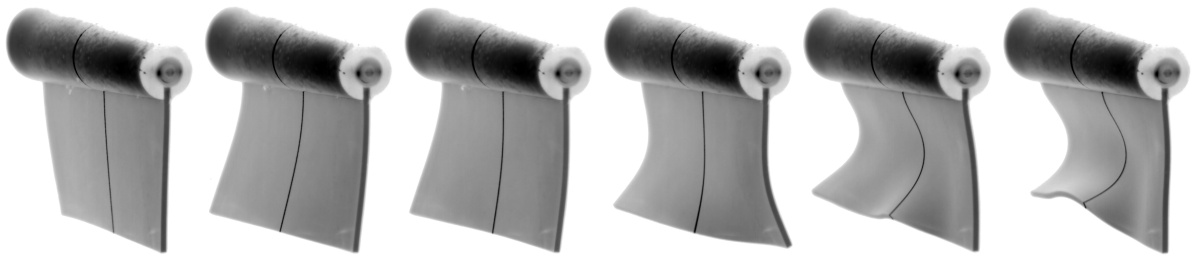

Figure 174: FSI-PfS-3b: Characteristic moments of the structure deformation at several inflow velocities.

Based on these preliminary studies the final inflow velocity for this test case is set to $u_{\text{inflow}} = 0.549$ m/s. Here, the FSI phenomenon is quasi-periodic but fully three-dimensional with large structural deformations in negative z-direction (large cone diameter) and smaller deflections in positive z-direction (small cone diameter). In Fig. 175 the displacements of the structure at the three measurement points ($x/D = 3.13$) within a time interval of one second (raw data) are

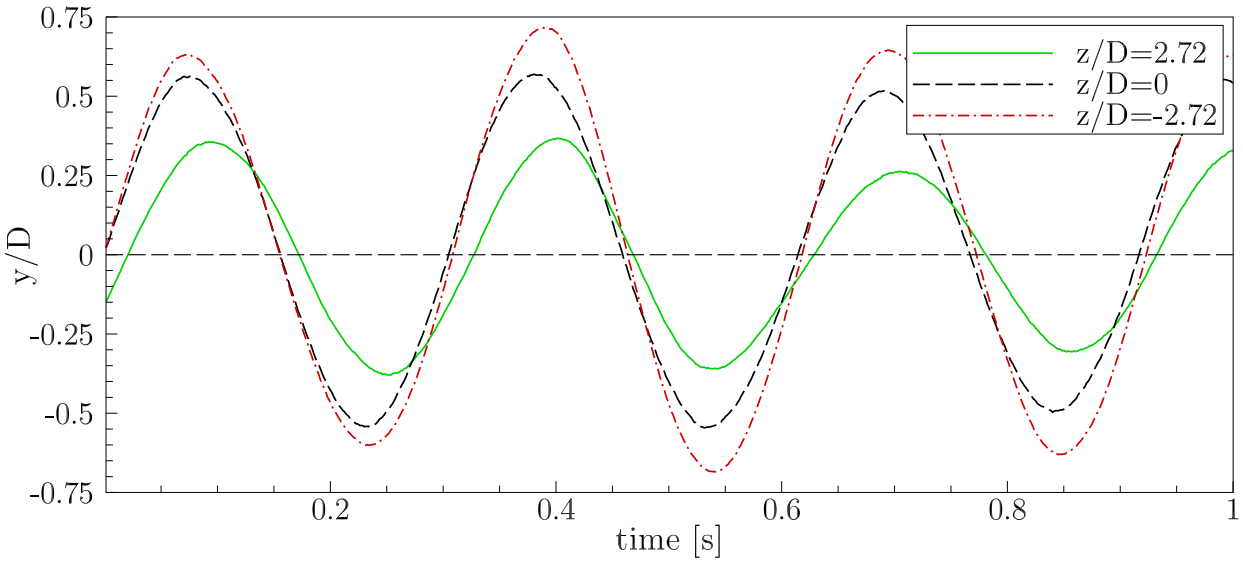

Figure 175: FSI-PfS-3*b*: Experimental structural results: Time history of the structural deflections (extract) for the three measurement points at $x/D = 3.13$ at the measurement planes $(z/D)_{\text{large}} = -2.72$, $(z/D)_{\text{middle}} = 0$ and $(z/D)_{\text{small}} = 2.72$.

presented. The time histories of these three points reveal cycle-to-cycle variations regarding the displacement amplitudes, the swiveling frequency and the phase shift between the three measured deflections. Similar to FSI-PfS-3*a* the deformation of the structure at the large cone diameter is dominating the structural motion. The structure in the middle of the domain precedes the deflection downstream of the large cone with a phase shift of about 6 degrees, while the deflection past the small diameter follows with a phase delay of about 7 degrees with respect to the deflections in the midplane. That means that the swiveling motion present in this test case differs from the swiveling mode in FSI-PfS-3*a*. While in the case 3*a* a wave-like motion starts at the large cone diameter and moves through the flexible rubber material until it reaches the small cone diameter, here the para-rubber plate first deflects in its middle followed by its lateral sides, respectively. This kind of deflection is also observed in FSI-PfS-1*a* with the difference that the phase delays are much shorter and the deformation is almost two-dimensional (the lateral sides move almost simultaneously). In the present case the middle of the rubber plate is followed by the plane downstream of the large cone diameter (larger deflection extrema) and the plane at the small cone diameter even later (smaller deflection extrema). This deflection behavior can be explained by the soft para-rubber material. While in FSI-PfS-3*a* the stiff EPDM rubber possesses a strong deformation resistance and therefore a large local dependence on the overall deflection of the entire structure, now the soft para-rubber is locally more unconstrained. It can be assumed that the local integral pressure forces have a crucial influence on the temporal deformation within the reference period.

The phase-averaged results for the structure are presented in Fig. 176 for the three planes and in Fig. 177 for the entire line in z-direction along the extremity. The phase averaged values of the peak deflections are $(y/D)_{\text{large}} \approx \pm 0.66$, $(y/D)_{\text{middle}} \approx \pm 0.56$ and $(y/D)_{\text{small}} \approx \pm 0.33$ (see Table 21). Similar to FSI-PfS-3*a* the tendency of the different scales as a function of the local cone diameter is also present for the phase-averaged deflections in this test case.

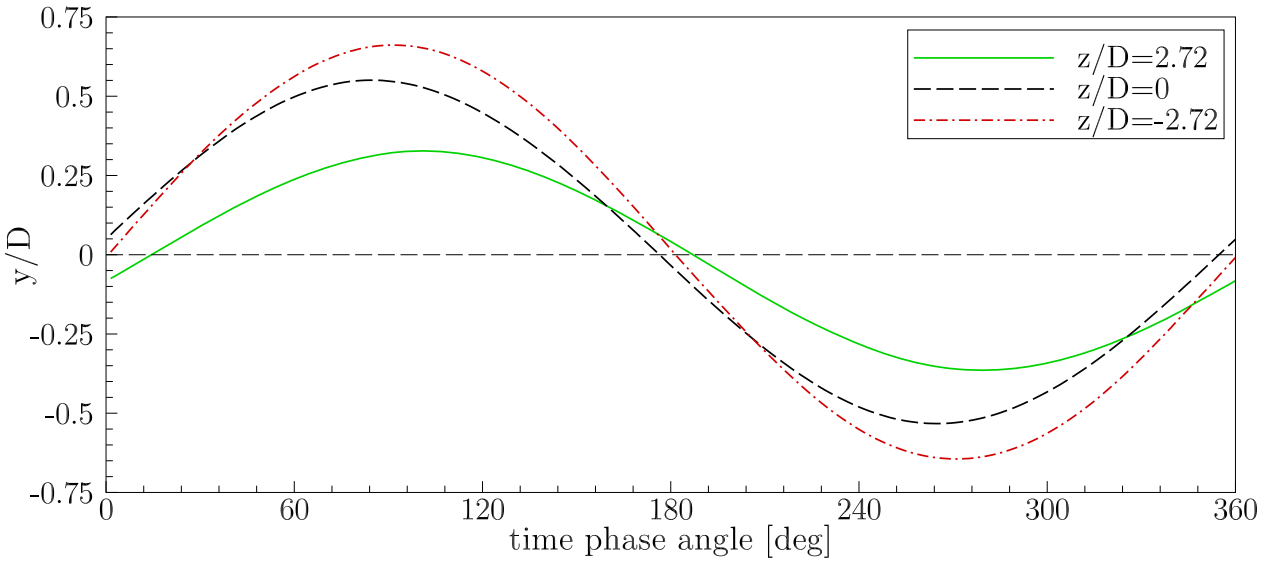

Figure 176: FSI-PfS-3*b*: Experimental structural results: Phase-averaged structural deflections for the three measurement points at $x/D = 3.13$ at the three measurement planes $(z/D)_{\text{large}} = -2.72$, $(z/D)_{\text{middle}} = 0$ and $(z/D)_{\text{small}} = 2.72$.

While the displacements decrease towards the small cone diameter, the standard deviations increase which again can be assigned to the uniform vortex shedding frequency in spanwise direction which eventually generates increased flow fluctuations in the region downstream of the small cone end. As already mentioned for the test case FSI-PfS-3*a* the plate motion forces the system to an uniform vortex shedding frequency which may results in a sensitive coupling of the structure and the fluid especially in the region behind the small cone diameter where a much higher vortex shedding frequency would be present in the fixed case. The frequency of the FSI phenomenon, i.e., the frequency of the y-displacements, is about $f = 3.20$ Hz with $\sigma(f) = 0.0928$ (2.90%).

plane	$(y/D)_{\text{max}}$ large	$(y/D)_{\text{min}}$ large	$(y/D)_{\text{max}}$ middle	$(y/D)_{\text{min}}$ middle	$(y/D)_{\text{max}}$ small	$(y/D)_{\text{min}}$ small
y-displacement	0.66	−0.66	0.57	−0.55	0.30	−0.30
standard deviation σ	0.0353 (5.30%)	0.0358 (5.46%)	0.0483 (8.50%)	0.0333 (6.02%)	0.0331 (10.82%)	0.0302 (9.93%)

Table 21: FSI-PfS-3*b*: Measured mean y-displacements y/D and their corresponding standard deviations σ at the three measurement points at $x/D = 3.13$.

The Strouhal numbers are calculated to $\text{St}_{\text{large}} \approx 0.16$, $\text{St}_{\text{middle}} \approx 0.13$ and $\text{St}_{\text{small}} \approx 0.10$ related to their individual cone diameter, respectively. As already mentioned Fig. 177 illustrates the displacements of the entire line in z-direction measured along the extremity at $x/D = 3.13$. This figure shows the short phase delay along the spanwise direction. Each section of the flexible structure reaches its extrema within a phase interval of 13 deg.

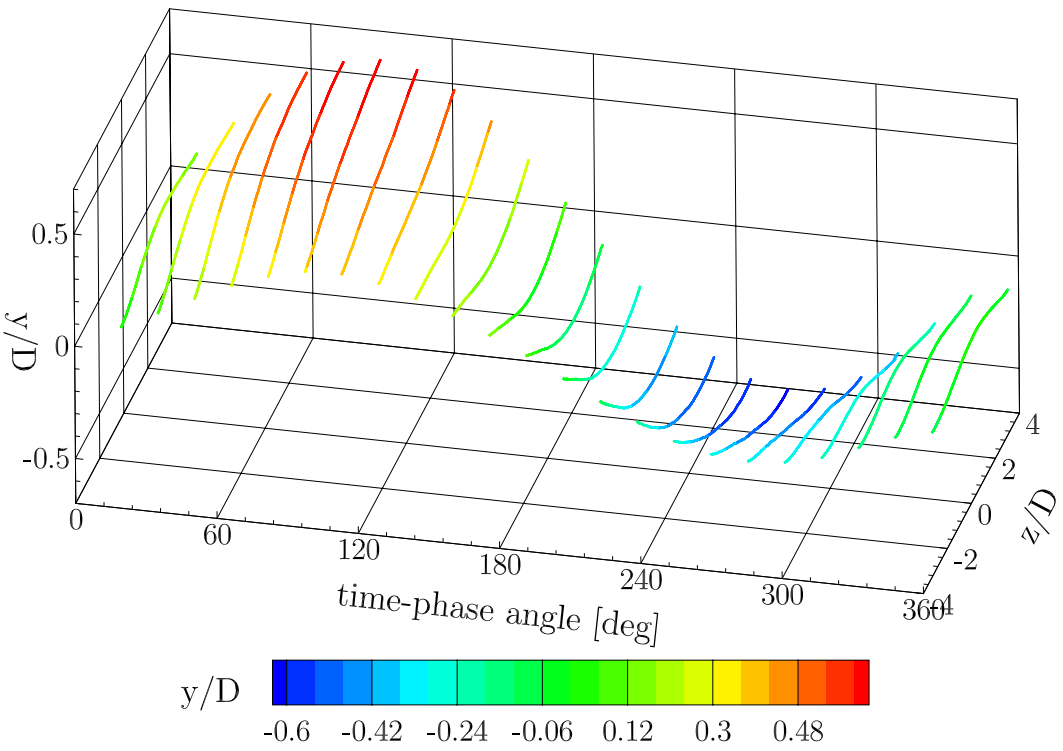

Figure 177: FSI-PfS-3*b*: Phase-averaged structural results for the reference period; entire line in z-direction close to the extremity of the flexible structure at $x/D = 3.13$.

FSI-PfS-3b - Flow field

In Fig. 178 the averaged flow field of the three planes at $(z/D)_{\text{large}} = -2.72$, $(z/D)_{\text{middle}} = 0$ and $(z/D)_{\text{small}} = 2.72$ are shown. In all three flow fields the characteristic physical phenomena (a stagnation point in front of the cone, acceleration areas on the upper and lower side of the structure, shear layers evolving from the cone, a recirculation area downstream of the cone and a broad wake area behind the structure) are again observed. By comparing all three planes to each other it is noticeable that there is a tendency regarding the scales from the large to the small side of the cone. The acceleration areas as well as the wake area are larger in the plane $(z/D)_{\text{large}} = -2.72$ (large cone diameter) than at $(z/D)_{\text{middle}} = 0$ and $(z/D)_{\text{small}} = 2.72$ (small cone diameter).

A selection of phase-averaged flow fields is depicted in Figs. 179 and 180. The phase-averaged flow results are rather similar to the results of FSI-PfS-3*a*. The present variations mainly refer to the lower vortex shedding frequency as a consequence of the decreased inflow velocity and the shorter phase delay of the structural deformations in comparison to FSI-PfS-3*a*.
In the first picture at a phase angle of 16 deg the flexible plate is nearly in its initial position. While the entire plate is moving in the positive y-direction, the acceleration areas at the upper side of the cone strongly grow while at the opposite side only small acceleration areas and a previously shed vortex are observed. During the phase interval until the next picture at 78 deg this vortex is convected further downstream and the para-rubber plate reaches its maximal deflection at all planes within ±10 deg. This short phase delay is also noticeable for the present flow structures in the different planes. While in FSI-PfS-3*a* a significant temporal

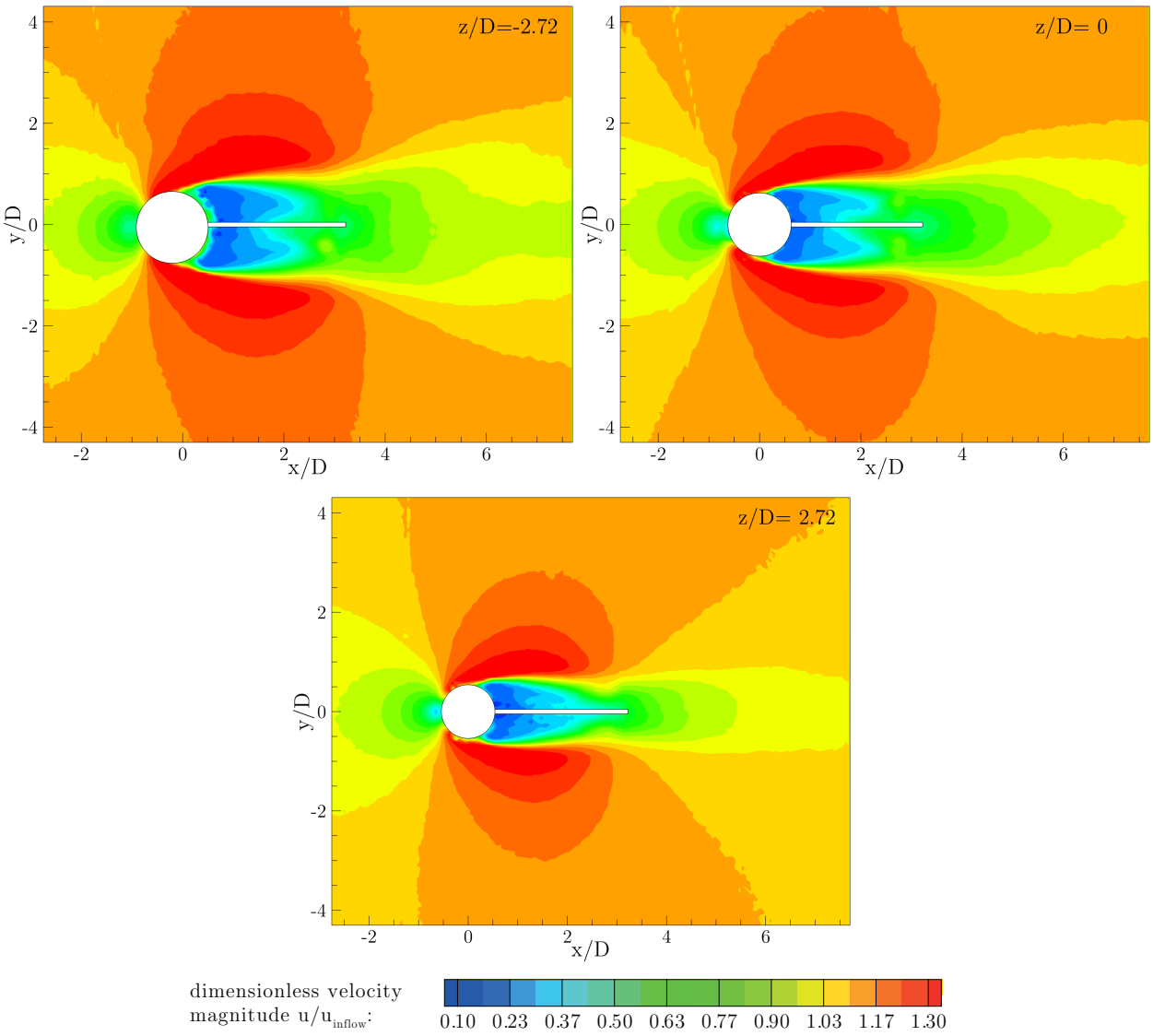

Figure 178: FSI-PfS-3b: Experimental flow and structural results, averaged over all measured periods at the three measurement planes $(z/D)_{\text{large}} = -2.72$, $(z/D)_{\text{middle}} = 0$ and $(z/D)_{\text{small}} = 2.72$.

deviation between the large cone diameter and the small cone diameter is visible in the flow fields, here a corresponding effect is not observed. This is obvious in the following picture showing the phase angle of 141 deg, where the structure moves back in the opposite (negative y-) direction and a vortex is shed from the cone almost simultaneously in all measurement planes. The passage of the neutral line of the flexible structure downstream of the large cone diameter marks the end of the first half of the phase-averaged period. In the second half period the pressure forces and the resulting structural deformations are reversed with respect to its first half.

Since the flow fields of both configurations of FSI-PfS-3x are found to be quite similar, the POD analysis are alike, too. Again, the distributions of the kinetic energy referring to the streamwise velocity u (Figs. 171a and b), the cross-flow velocity component v (Figs. 171c and d) and the vorticity (Figs. 171e and f) are presented for the midplane at $z/D = 0$. Varia-

tions in each field mainly correspond to the reduced vortex shedding frequency of FSI-PfS-3*b* in comparison to 3*a*. Additionally, the lower inflow velocity in FSI-PfS-3*b* leads to decreased fluctuations in the entire flow field. Therefore, the fluctuations caused by the movement of the flexible structure due to the fluid become more distinct. Therefore, a rough estimation of the structural deflections and its bending mode is visible in the POD analysis of the streamwise velocity u and the vorticity.

Quantitatively, the POD analysis shows again the decline of the kinetic energy from the thicker side to the smaller side of the cone. The entire kinetic energy is calculated to $k_{\mathrm{abs,all,large}} = 469.25\,\mathrm{m^2/s^2}$ ($k_{\mathrm{rel,all,large}}= 100\%$) at $(z/D)_{\mathrm{large}} = -2.72$, $k_{\mathrm{abs,all,middle}}= 280.56\,\mathrm{m^2/s^2}$ ($k_{\mathrm{rel,all,middle}}= 100\%$) at $(z/D)_{\mathrm{middle}} = 0$ and $k_{\mathrm{abs,all,small}}= 103.62\,\mathrm{m^2/s^2}$ ($k_{\mathrm{rel,all,small}}= 100\%$) at $(z/D)_{\mathrm{small}} = 2.72$, respectively. Again, the relative energy distribution over the POD modes are similar to its equivalent in FSI-PfS-3*a*. The summarized energy values of the first two modes are found to be 53.13% ($(z/D)_{\mathrm{large}} = -2.72$), 55.77% ($(z/D)_{\mathrm{middle}} = 0$) and 38.53% ($(z/D)_{\mathrm{small}} = 2.72$) of its corresponding total energy content.

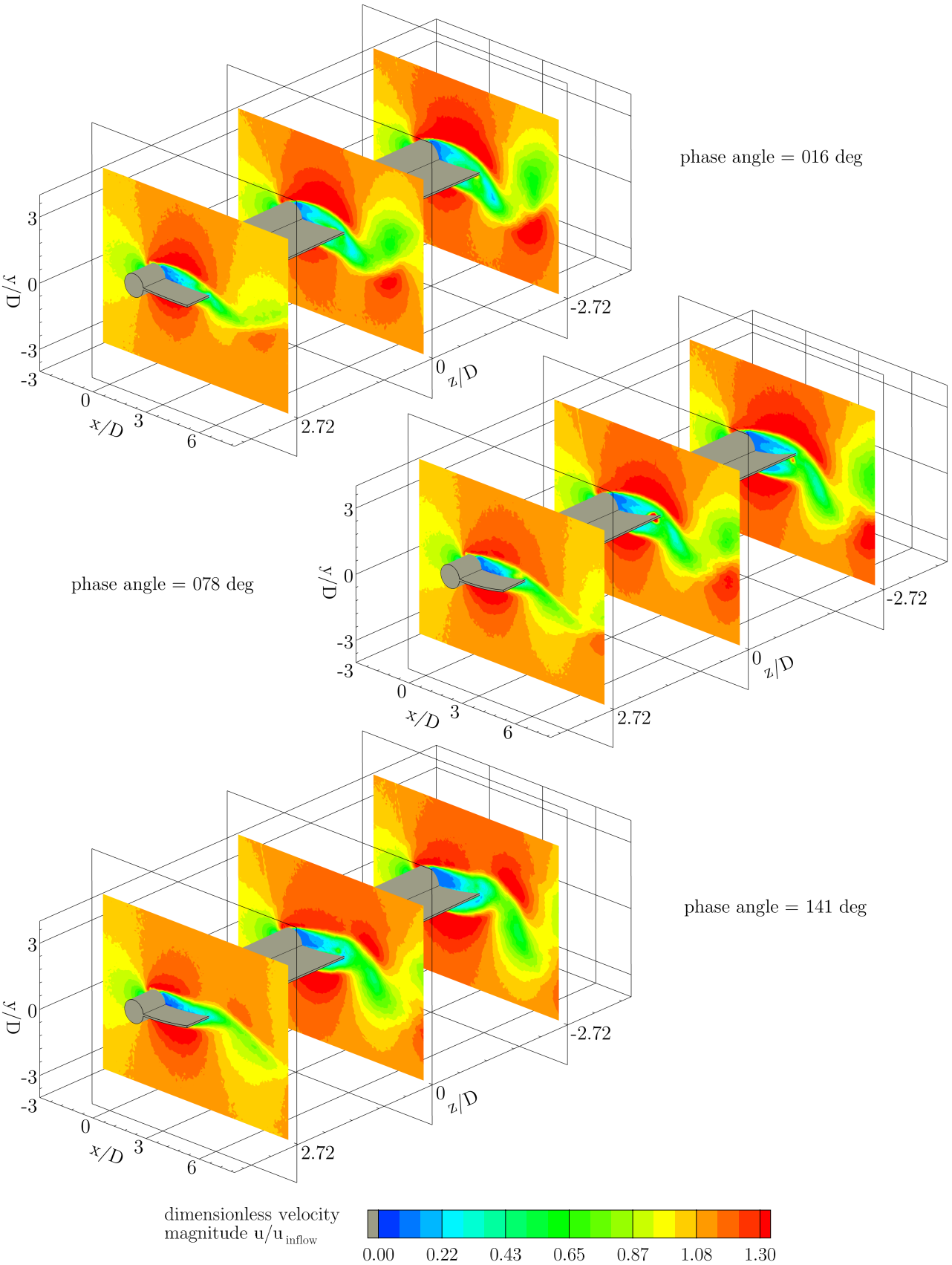

Figure 179: FSI-PfS-3*b*: Experimental phase-averaged flow and structural results for the first half of the reference period at three measurement planes at $(z/D)_{\text{large}} = -2.72$, $(z/D)_{\text{middle}} = 0$ and $(z/D)_{\text{small}} = 2.72$.

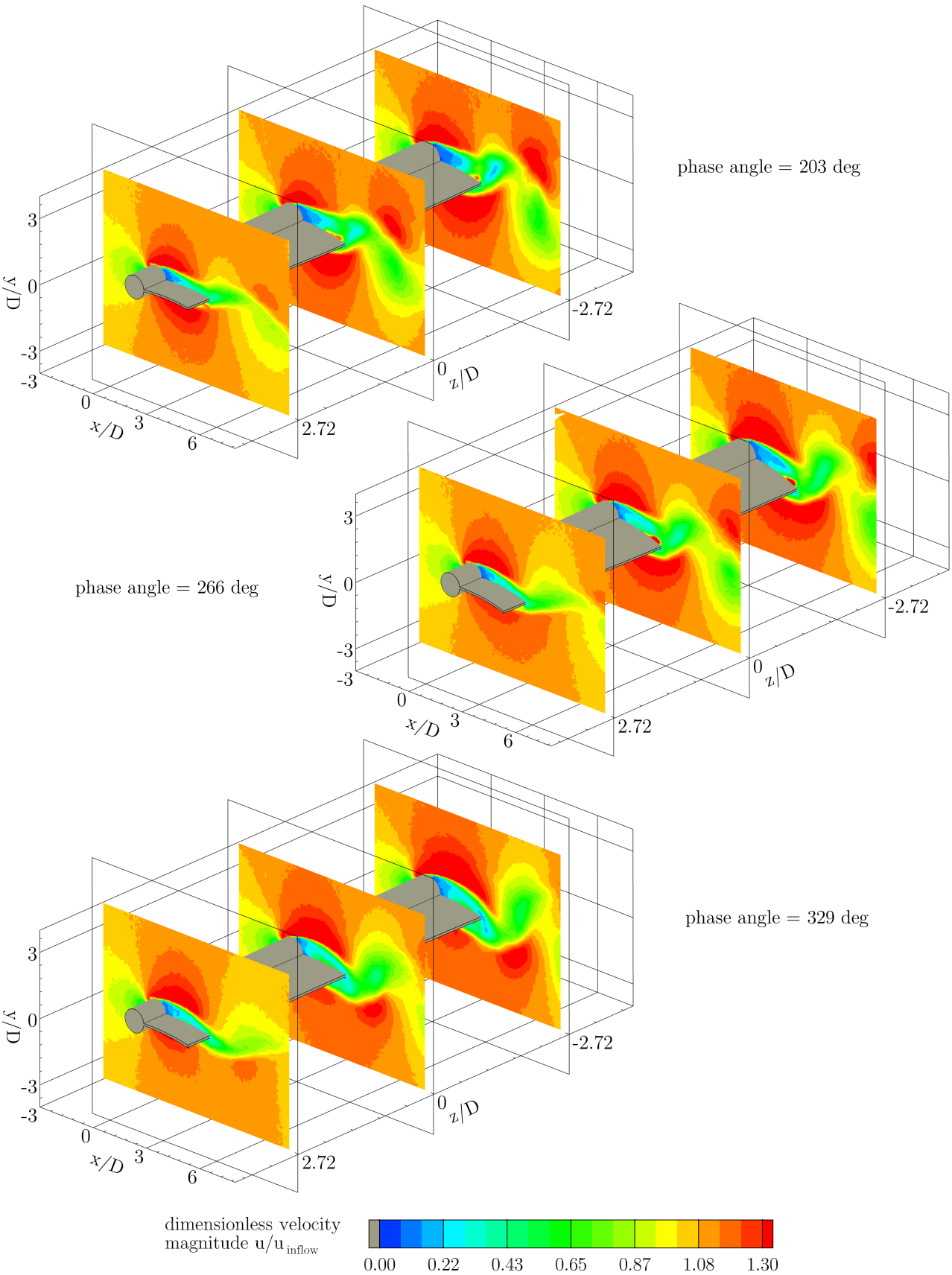

Figure 180: FSI-PfS-3*b*: Experimental phase-averaged flow and structural results for the second half of the reference period at three measurement planes at $(z/D)_{\text{large}} = -2.72$, $(z/D)_{\text{middle}} = 0$ and $(z/D)_{\text{small}} = 2.72$.

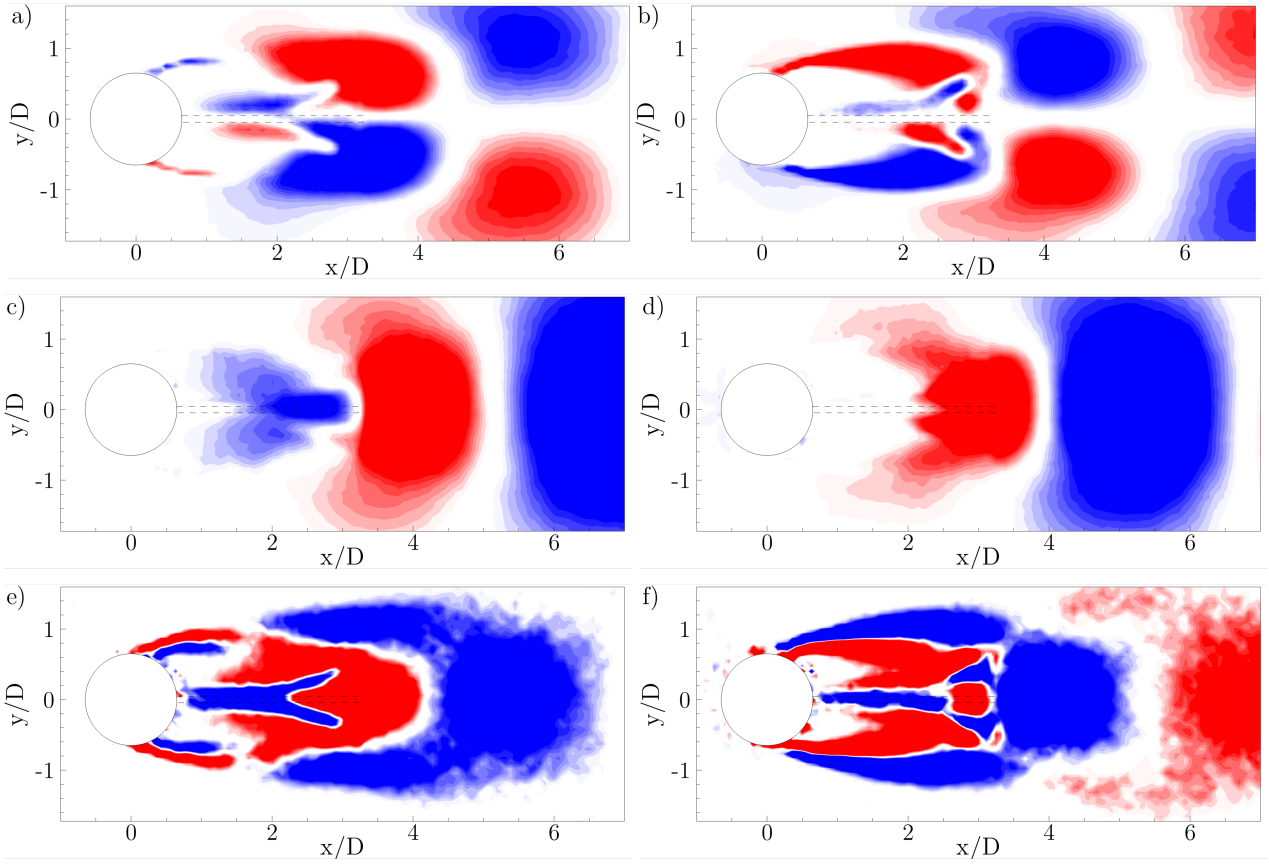

Figure 181: FSI-PfS-3*b*: POD analysis of the two-dimensional flow fields in the midplane ($z/D = 0$) a) velocity component u, first mode; b) velocity component u, second mode; c) velocity component v, first mode; d) velocity component v, second mode; e) vorticity component ω_z, first mode; f) vorticity component ω_z, second mode.

FSI-PfS-3x - Conclusion

In the third series of test cases FSI-PfS-3x a more complex front body geometry is applied to set-up three-dimensional FSI test cases in terms of structural deflection and fluid flow. In order to maintain most of the measures of the two-dimensional test cases FSI-PfS-1x and 2x, the front cylinder is replaced by a cone (the small cone diameter is equal to the former cylinder diameter D while the large cone diameter measures $1.5 \cdot D$). According to the spanwise enlargement of the cone, the flexible plate attached to it is adapted to the new geometry and preserves the plate length of 60 mm. The two present configurations FSI-PfS-3a and 3b differ in the plate material (EPDM rubber and para-rubber) and the applied inflow velocities ($u_{\text{inflow}} = 0.969$ m/s and $u_{\text{inflow}} = 0.549$ m/s).
Both test cases are limited to moderate structural deflections in one dominant swiveling mode. A quasi-periodic state in the structural deformation and the fluid motion is reached in both cases but by applying different inflow velocities. Due to the increased complexity of the flow according to the three-dimensional geometry of the front body only one quasi-periodic oscillation state is noticed in contrast to the presence of two swiveling modes, e.g., in FSI-PfS-2x. In the present state a fully three-dimensional deformation of the flexible structure appears within the oscillation period. For FSI-PfS-3a a wave-like deformation in the plate propagates from the large cone diameter to the small cone diameter with decreasing structural deflections. This behavior is consistent with the assumption of higher fluid loads caused by the larger shedding vorticies on the large side of the cone in contrast to its opposite side proven by the PIV measurements at different planes. The stiff EPDM rubber supports or eventually enables this wave-like deflection behavior. In FSI-PfS-3b a different deflection behavior is observed. Here, the middle section of the plate reaches the extrema first followed by the parts downstream the large and later the small cone diameter. It can be assumed that the soft para-rubber decreases the deformation resistance in comparison with the EPDM rubber and therefore the local characteristics of the entire structure deformation. However, in both cases the structural deflections are limited to the dimension of the front body (similar to the two-dimensional test cases without a steel weight FSI-PfS-1x) with mild variations towards the large end of the cone and stronger fluctuations downstream of the small cone diameter (see Table 22).

As already mentioned the oscillation behavior is strongly affected by the applied material of the rubber plate. Beside the three-dimensional deflection behavior, the low YOUNG's modulus of the para-rubber plate (FSI-PfS-3b) also reduces the critical inflow velocity of the FSI onset. As a consequence the destabilization of the quasi-periodic swiveling state commences earlier compared to the EPDM rubber in FSI-PfS-3a. This is also represented by the bending stiffness K_B for FSI-PfS-3a with $K_B = 0.07023$ which is almost doubled in comparison to the value of $K_B = 0.03720$ calculated for FSI-PfS-3b. In both cases the fluctuations of the deflections increase towards the small cone diameter. This indicates that the flow works against the "lock-in" swiveling state of the system. More precise the vortex shedding frequency naturally rises along the decreasing cone diameter while the attached flexible plate forces an uniform vortex shedding frequency. It can be assumed that at the smaller end of the cone the physical coupling between the flow and the structure is eventually more sensitive and leads to the increased variations in the deflections there.

Test case	**FSI-PfS-3*a***	**FSI-PfS-3*b***
behavior	3D	3D
bending modes	1st mode	1st mode
bending stiffness K_B	0.07023	0.03720
u_{inflow} [m/s]	0.969 m/s	0.549 m/s
symmetry	✓	✓
f [Hz]	5.77	3.20
$\sigma(f)$	±2.08%	±2.90%
St	0.131	0.128
$(y/D)_{\text{large}}$	±0.54	±0.66
$\sigma(y/D)_{\text{large}}$	±7.08%	±5.38%
$(y/D)_{\text{middle}}$	±0.460	±0.56
$\sigma(y/D)_{\text{middle}}$	±6.34%	±7.26%
$(y/D)_{\text{small}}$	±0.224	±0.30
$\sigma(y/D)_{\text{small}}$	±13.52%	±10.38%
POD energy content $k_{\text{abs,all,large}}$	934.30 m^2/s^2	469.25 m^2/s^2
POD energy content $k_{\text{abs,all,middle}}$	595.11 m^2/s^2	280.56 m^2/s^2
POD energy content $k_{\text{abs,all,small}}$	147.23 m^2/s^2	103.62 m^2/s^2

Table 22: Summary of FSI-PfS-3x.

The observation that this sensitive region does not affect the entire system coupling can be explained by the POD analysis. The analysis at the different measurement planes reveals a strong decrease of the kinetic flow energy from the large cone diameter to the small cone diameter (see Fig. 182 for the case FSI-PfS-3*a* and Fig. 183 for the case 3*b*). That means that only a small fraction of the kinetic energy is present towards the small end of the cone while the large end with its great amount of flow energy dominates the coupled system. It can be assumed that all unstable flow effects at the small side of the cone are suppressed by the flow excitation coming from its large side.

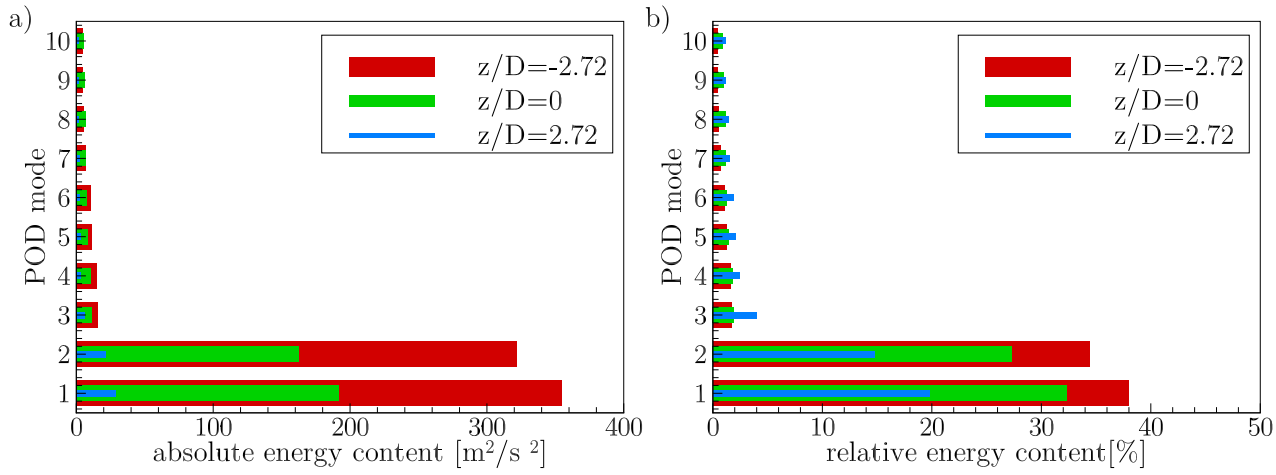

Figure 182: FSI-PfS-3*a*: POD results

Since the mentioned flow effects are mainly the effect of the three-dimensional geometry of the

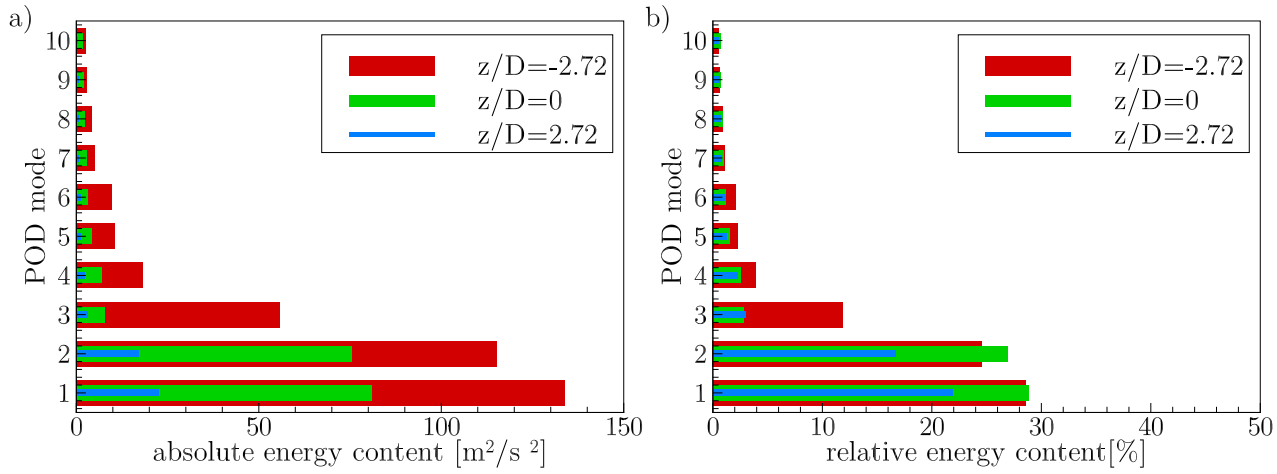

Figure 183: FSI-PfS-3*b*: POD results

bluff body, the instability-induced excitation (IIE) is assumed to be responsible for the FSI coupling. In both test configurations the structural motion is driven by the vortex shedding instability. The limitation to the swiveling mode in main flow direction and the moderate deflections in the range of the local cone diameter are not able to alter the system coupling. Thus, the movement-induced excitation (MIE) state does not appear.

10.1.4. FSI-PfS-4x (Application-based test cases)

The fourth set of test cases (FSI-PfS-4x) consists of an elastic circular polyethylene cylinder clamped at one channel wall and free at the opposite side (see test case definitions in Section 6.3.4). The configurations FSI-PfS-4a and 4b differ concerning eight additional rigid cylinders that build together with the flexible cylinder a 3 $\times$ 3 alignment in the case 4b. The configurations FSI-PfS-4x are again geometrically simple and tend to an application-based FSI test case scenario. Applications regarding these generic configurations are widespread. Maritime structures such as tension risers (Yang and Xiao, 2014) applied in the offshore oil extraction are a common example referring to the present configuration of FSI-PfS-4a. Tube bundles in heat exchangers correspond to the more complex set-up of FSI-PfS-4b. Here, structural vibrations caused by a fluid-structure excitation may lead to significant damage scenarios in several industrial applications (Weaver and Fitzpatrick, 1988; Païdoussis and Li, 1992; Goyder, 2002; Païdoussis, 2006; Shinde et al., 2014). Especially, the vortex-induced vibrations on fuel rods in nuclear plants are seriously studied (Païdoussis, 2006) in the last decades due to its important safety aspects.

In the following paragraphs the experimental results of the two configurations FSI-PfS-4x are discussed in terms of their structural deflections and their corresponding fluid flow. In contrast to the previous test cases now all results are normalized by the small diameter of the flexible cylinder $d = 0.008$ m and obtained at the measurement plane $(z/d) = 20.63$ in the vicinity of the cylinder tip (see Fig. 184). Furthermore, the structural results are based on measurements yielding the circular xy-cross-section of the flexible cylinder at this measurement plane. Out of the circularly arranged points and the known cylinder diameter its center point is calculated and referenced in the following results.

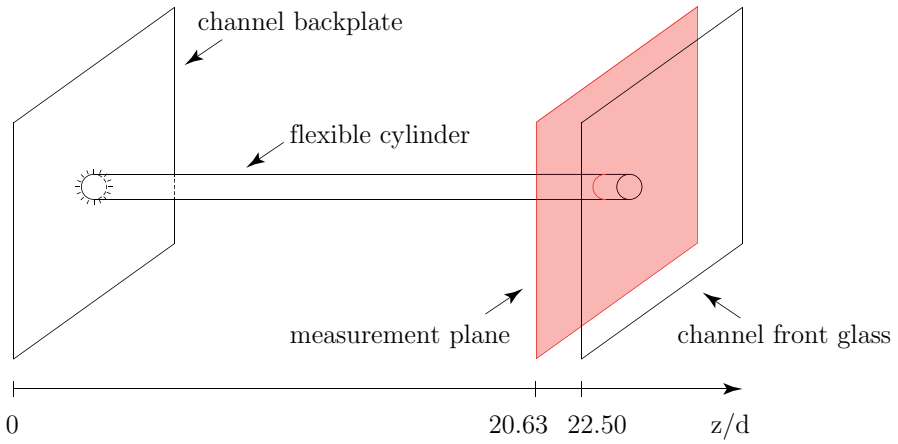

Figure 184: Measurement plane of FSI-PfS-4x.

FSI-PfS-4a - Structural results

The stiff polyethylene cylinder fixed at the channel wall deflects with moderate deformations in the range of the cylinder diameter but high oscillation frequencies. Figures 185 and 186 refer to the structural response as a function of the inflow velocity up to $u_{\text{inflow}} = 1.9$ m/s. In Fig. 185 the maximal and minimal amplitudes of the structural deformations are given. The corresponding swiveling frequencies of the flexible cylinder are shown in Fig. 186. These averaged results are based on a series of 10 single measurements in which the inflow velocity of the water tunnel is continuously increased step by step.

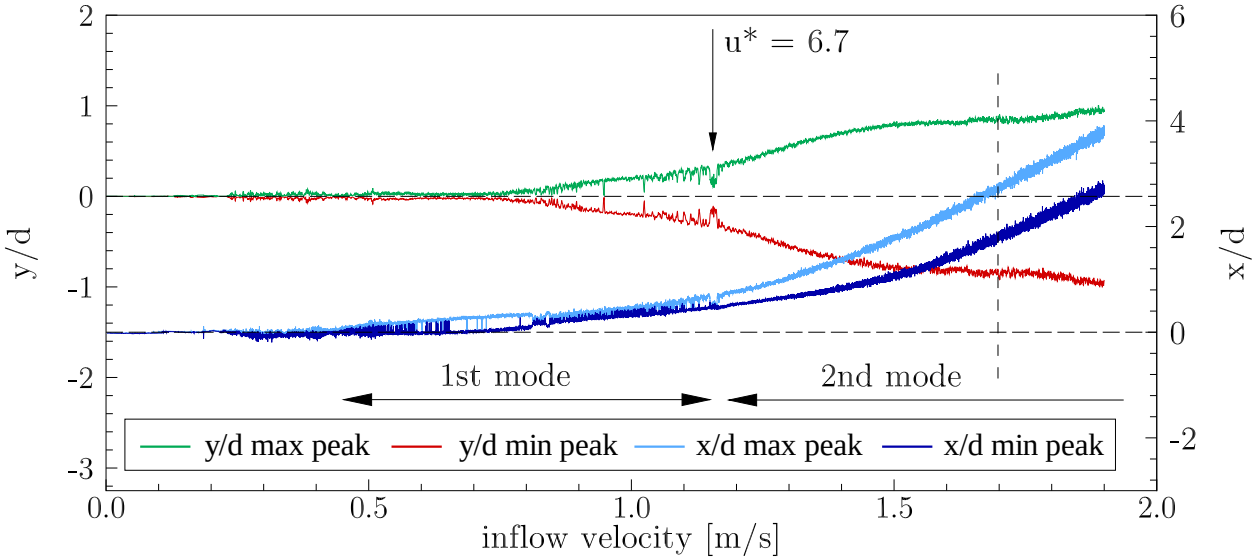

Figure 185: FSI-PfS-4*a*: Averaged maximal/minimal structural deflections as a function of the inflow velocity.

The FSI coupling starts at an inflow velocity of about $u_{\text{inflow}} = 0.20$ m/s with tiny and aperiodic deformations until the velocity reaches a magnitude of 0.75 m/s. By reaching this critical inflow velocity the amplitudes of the structural deformations start to rise slowly. Within the range of inflow velocities of about $u_{\text{inflow}} = 0.75$ to 1.15 m/s an increase of the deflections is observable but it remains small. At about $u_{\text{inflow}} = 1.15$ m/s an abrupt decrease of the deflections is noticeable. This momentary structural response marks the further increase to larger structural deflections up to maximal and minimal displacements of about $y/d \approx \pm 1$ at $u_{\text{inflow}} = 1.9$ m/s. Similar to the y/d-deflections the x/d-coordinate of the center point shows large deflections up to $x/d \approx 4$. Due to the increasing inflow velocities the drag forces raise quadratically. This is evident by the nearly quadratic increase of the x/d displacements. The high drag forces result in a maximum of the tip deflection of the polymer cylinder of about $x/d = 3.91$ at the inflow velocity of $u_{\text{inflow}} = 1.9$ m/s. Remarkable is the range of the peak-to-peak x/d-displacements. The cylinder tip swivels with about $x/d = \pm 0.17$ around $x/d = 0.6$ at $u_{\text{inflow}} = 1.17$ m/s in contrast to the increased oscillations at $u_{\text{inflow}} = 1.9$ m/s with $x/d = \pm 0.67$ around $x/d = 3.22$. The swiveling frequencies f and the Strouhal number St (Fig. 186) related to the y/d-deflections reveal strong fluctuations until the inflow velocities of $u_{\text{inflow}} = 0.9$ m/s is reached. Here, the structure oscillates at a frequency of $f = 19.96$ Hz (St = 0.178). A significant change of the

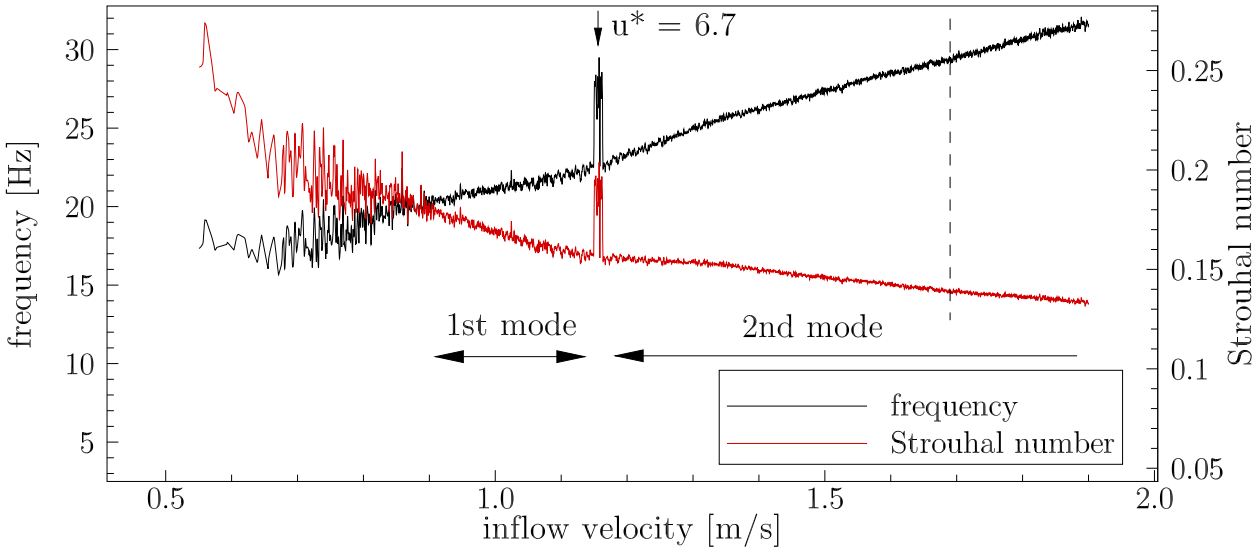

Figure 186: FSI-PfS-4*a*: Averaged frequency and Strouhal number as a function of the inflow velocity.

swiveling frequency is noticed at $u_{\text{inflow}} = 1.15$ m/s ($f = 22.40$ Hz) corresponding to the structural displacements y/d and x/d mentioned in the previous paragraph. This structural response is characterized by a short and abrupt increase in the frequency to $f = 29.5$ Hz (St $= 0.196$) and represents the mode transition from the first swiveling mode (small deflections) to the second swiveling mode (large deflections). In contrast to the other test cases this mode transition is characterized by a short increase in the swiveling frequency and a corresponding decrease in the structural deflections at the particular inflow velocity of about $u_{\text{inflow}} \approx 1.15$ m/s. After the mode transition an oscillation frequency of about $f = 23.0$ Hz is present. In the following the oscillation frequency rises almost linearly to a frequency of about 31.8 Hz (St $= 0.133$) at $u_{\text{inflow}} = 1.9$ m/s.

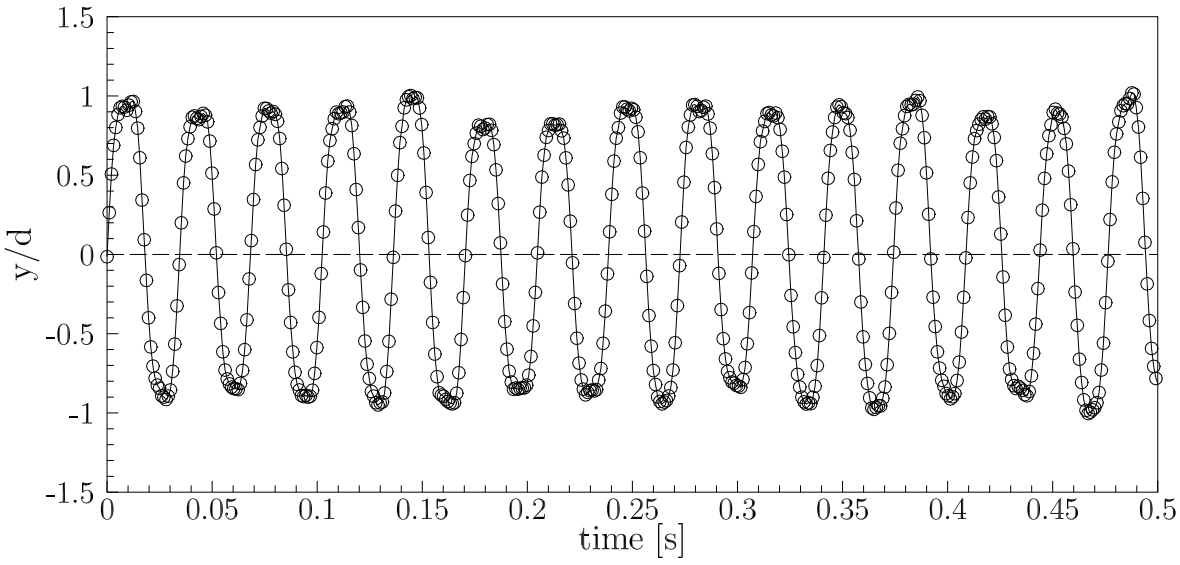

Figure 187: FSI-PfS-4*a*: Experimental structural results: Time history of the structural deflections (extract) for the center of the flexible cylinder at the measurement plane $(z/d) = 20.63$.

The final velocity of this test case is set to the inflow velocity of $u_{\text{inflow}} = 1.69$ m/s (Re = 13,520). In this state the deflections are large (the time histories are shown in Fig. 187) with time-averaged peak y-displacements of about $(y/d)_{\max} = 0.903$ and $(y/d)_{\min} = -0.895$. Furthermore, the fluctuations are characterized by the moderate standard deviations of $\sigma((y/d)_{\max}) = 0.0421$ (4.66%) and $\sigma((y/d)_{\min}) = 0.0495$ (5.53%). In the x-direction the cylinder center swivels with minimal values of $(x/d)_{\min} = 2.84$ and maximal values of $(x/d)_{\max} = 3.85$. Compared to the values of the structural response in Fig. 185 a mismatch of the x-deflections is measured. The reason for this mismatch is found in the excitation before attaining the specific swiveling state. In the case of the measurement series related to the structural response the inflow velocity and hence the load on the cylinder is continuously increased. For the measurements at the fixed inflow velocity the load is kept constant at a high level. Related to this case preliminary studies reveal that a settlement phase of approximately three minutes is necessary till a quasi-periodic swiveling state of the flexible cylinder is achieved and the measurements can be started. Especially the x-deflections are influenced by this settlement phase by bending more and more in positive x-direction. It can be assumed that the integral load (mainly the drag force) within the settlement phase is lower in the first measurement series (Fig. 185) than in the second fixed velocity case. Therefore, the deflections in x-direction are larger in this case. The mean swiveling frequency at the fixed inflow velocity of $u_{\text{inflow}} = 1.69$ m/s is found to be $f_{\text{avg}} = 29.39$ Hz (St = 0.139) with a low standard deviation of $\sigma(f) = 0.62$ Hz (2.11%).

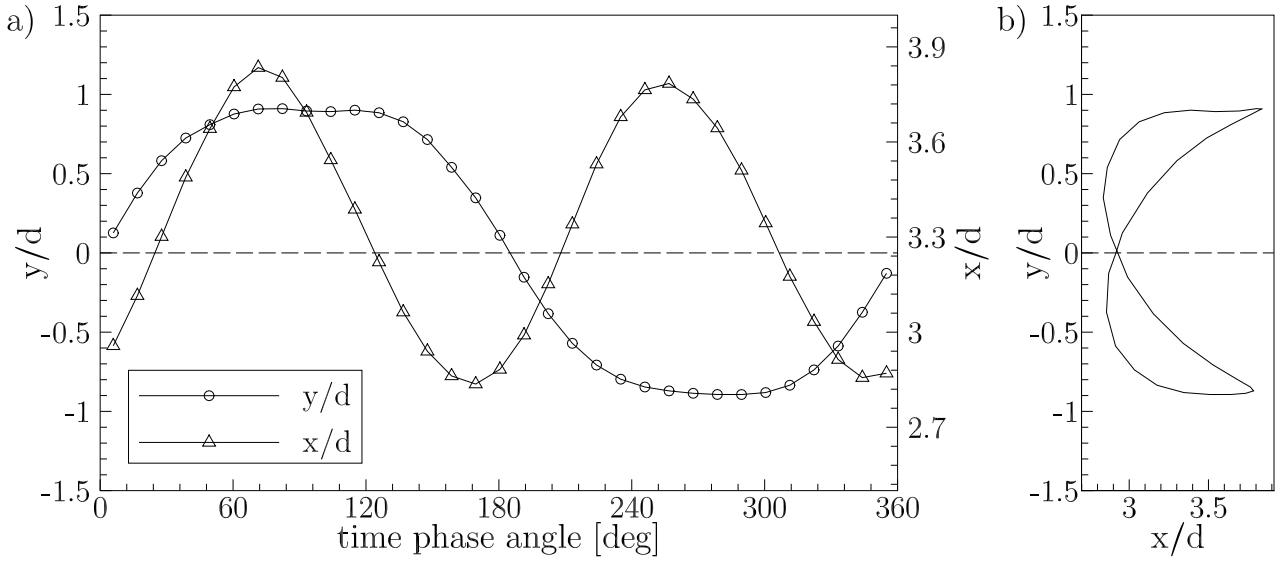

Figure 188: FSI-PfS-4*a*: Experimental structural results: a) phase-averaged reference period of the structure for the x/d- and y/d-deflections, b) xy-motion of the structural deflections, both for the center of the cylinder at $z/d = 20.63$.

The phase-averaged structural results are presented in Fig. 188a. The oscillation period consists of 31 phase-averaged data points calculated out of the recorded 4938 periods. While the x/d-deflection is characterized by a sinusoidal behavior with a doubled frequency (compared to the y/d-deflections), the y/d-displacements near the tip of the polyethylene beam are flattened towards the maximal and minimal deflections. By reaching these peak deflections the cylinder tip stays at its y/d-position for almost 50 degrees of the time-phase angles. Afterwards, the

cylinder tip accelerates rapidly to attain the opposite extrema. The xy-motion path of the cylinder tip describes a distorted eight "8" and is plotted in Fig. 188b.

FSI-PfS-4a - Flow results

The result of the flow field time-averaged over all PIV measurements without applying a phase-reconstruction method is depicted in Fig. 189a. Remarkable is the apparent influence of the cylinder motion on the flow field. The stagnation point in front of the cylinder is not visible due to the blurring effect by averaging a flow field containing a moving structure. The same effect is responsible for the strongly reduced velocities in the wake of the structure compared to the fixed cylinder case. That is clearly visible in the range ($y/d \approx 1.5$), where the cylinder moves. On the upper and lower sides of the cylinder the typical acceleration areas with decreasing velocities towards the channel walls are noticed. Rearwards a congealing recirculation area is present. Looking at the entire wake of the moving structure, its significant expansion of about six cylinder diameters is observed. In comparison to the fixed configuration (refer to Section 8.1.3) this is an increase of the wake from four to six cylinder diameters and only related to the FSI coupling. Other changes related to the flexible cylinder are the acceleration areas shifted in y-direction and the above mentioned blurred stagnation point in front of the moving cylinder. The distribution of the Reynolds shear stress $\overline{u'v'}$ depicted in Fig. 189b is also changed from the fixed to the flexible FSI configuration of this test case. While in the fixed configuration the maximal and minimal shear stresses are found in the wake of the fixed cylinder and correspond to the vortex shedding, now the maximal positive and negative stresses are observed in the vicinity of the moving cylinder. In the wake area only low shear stresses are present in the FSI case.

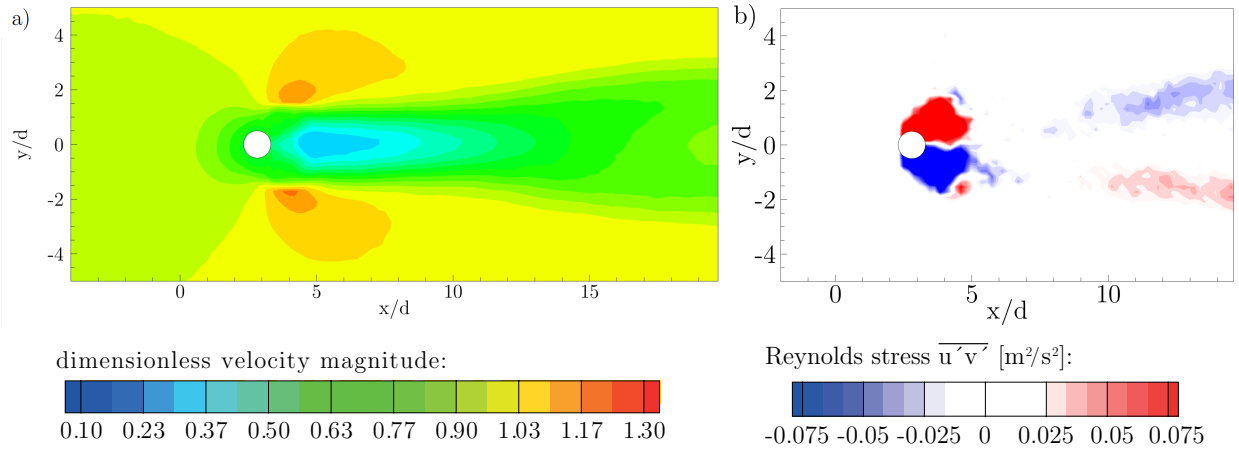

Figure 189: FSI-PfS-4*a*: Time-averaged flow results at the measurement plane $z/d = 20.63$ for a) the dimensionless velocity magnitude and b) the Reynolds shear stress $\overline{u'v'}$.

The combined phase-averaged flow and structural results are shown in Figs. 190 and 191 for the six time phase angles 16, 78, 141, 204, 266 and 326 deg. In these six states the large contrast to the time-averaged flow field in Fig 189 is visible. Several symmetric vortex centers shedding from the moving cylinder surface are located in its wake. The positions of the vorticies

indicate a 2P[19] arrangement similar to observations related to elastically supported cylinders by other authors (e.g., Blevins, 1990). That means that in each period a pair of two symmetric vorticies are shed from the moving cylinder and convected downstream. Due to the motion of the structure the stagnation point in front of the cylinder is not explicitly visible. The coarse resolution of the PIV measurements, the temporal limitation of the LLT sensor and the handicaps of the phase-averaging method (especially the resulting blurring effect) inhibit a more detailed analysis of the flow field in terms of, for example, the movement of the separation point on the moving cylinder and the collapse of the vorticies in the wake area. Changes in the experimental set-up, e.g., the reduction of the measurement area brought only minimal improvements to the present test configuration. Furthermore, the high oscillation frequency of the flexible cylinder impedes the PIV measurements by the large velocity gradients in the vicinity of the fast moving structure in comparison to the low fluid velocities in its wake.

[19] 2P - two vortex pairs are formed per period.

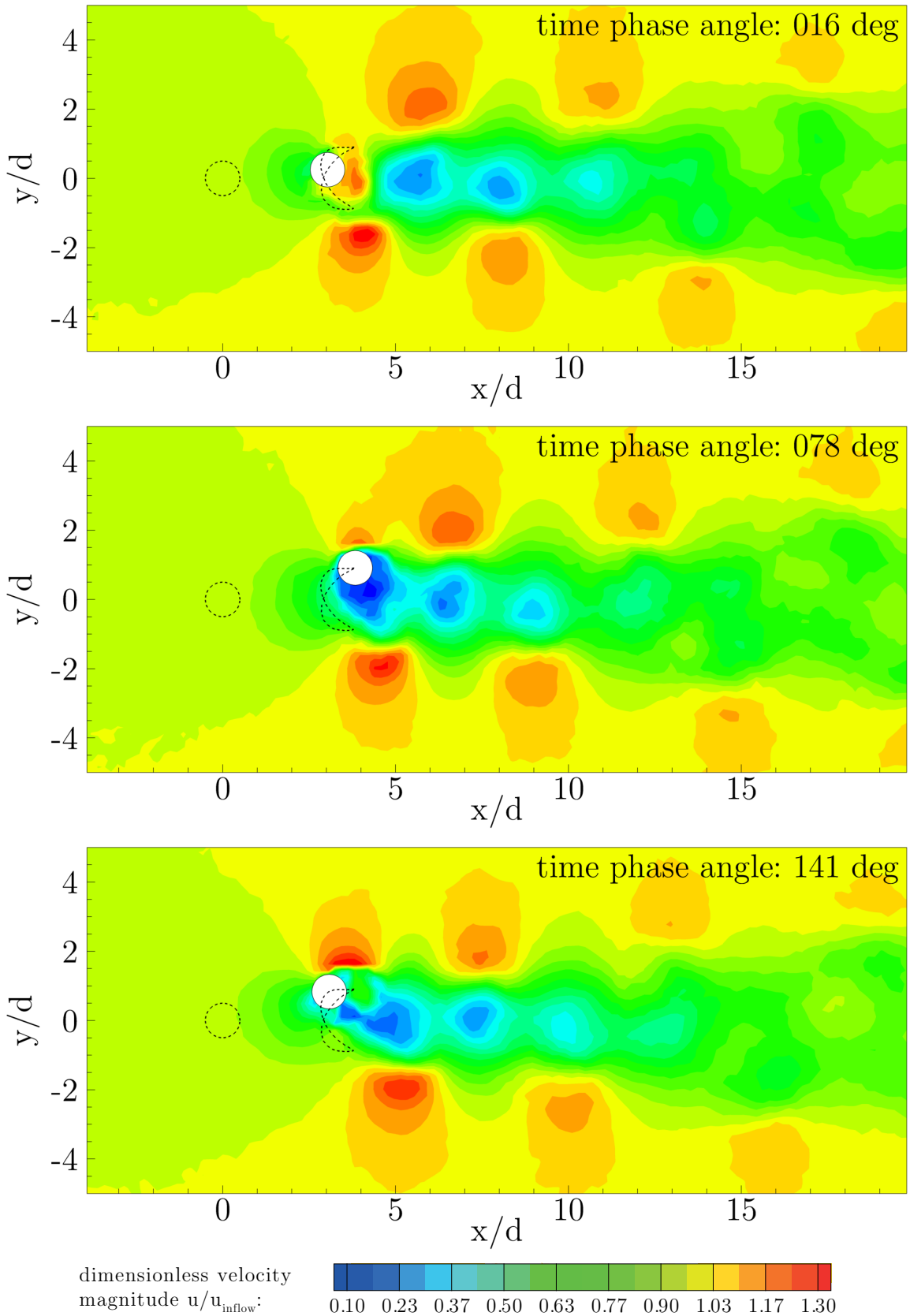

Figure 190: FSI-PfS-4*a*: Experimental phase-averaged flow and structural results for the first half of the reference period at the measurement plane $z/d = 20.63$.

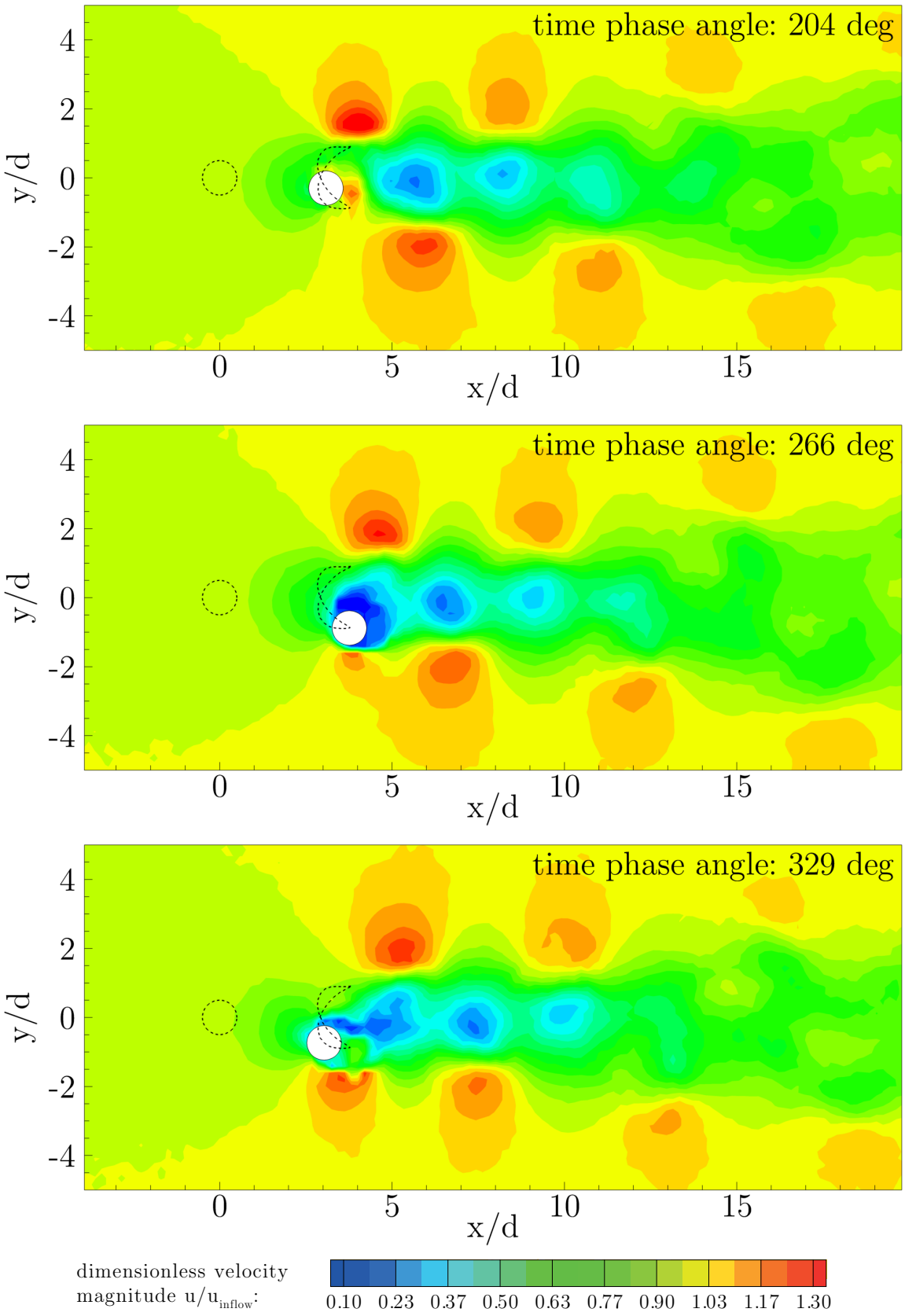

Figure 191: FSI-PfS-4*a*: Experimental phase-averaged flow and structural results for the second half of the reference period at the measurement plane $z/d = 20.63$.

In the time series of the six time phase angles in Figs 190 and 191 the mean quasi-periodic FSI

data of this test case are illustrated. In the first picture at a phase angle of 16 deg the cylinder tip is slightly deflected in positive y/d-direction. The fast motion of the structure induces a small acceleration area nearby. At the next phase angle of 78 deg the structure reaches its maximum deflection in y/d- and x/d-direction. On the upper and lower side of the cylinder two acceleration areas developed. At this phase angle the cylinder is almost motionless. At 141 deg both vorticies are already shed and the cylinder moves in negative y/d-direction to the opposite deflection extrema, repeating the whole process and forming the typical 2P vortex street. Since the four shedding vorticies are not visible in the velocity magnitude distributions (Figs 190 and 191) Fig. 192 depicts the vorticity component ω_z at the phase angle of 203 deg. In the direct vicinity of the moving cylinder the four generated vorticies are observed. Due to the coarse spatial and temporal resolution of the PIV system and the blurring of the phase-averaging, the vorticies are not visible further downstream.

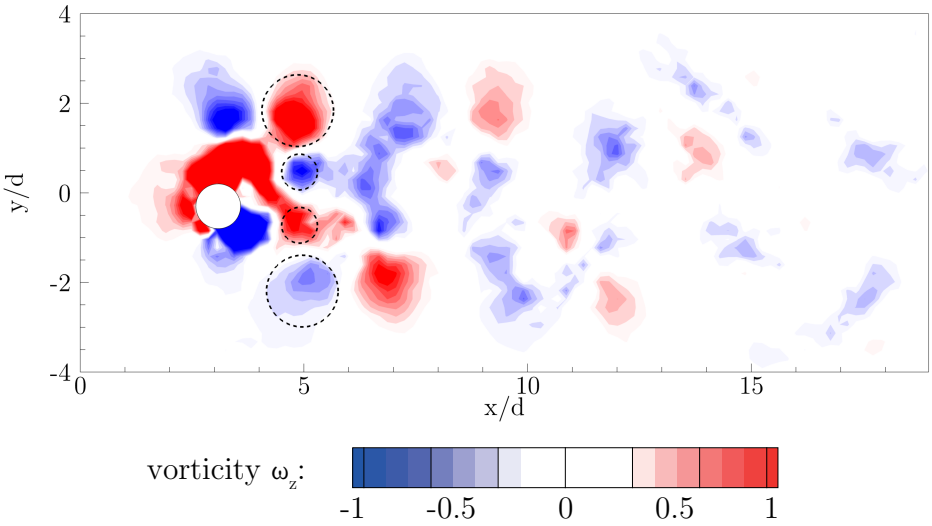

Figure 192: FSI-PfS-4*a*: Experimental phase-averaged flow vorticity at the phase angle of 203 deg at the measurement plane $z/d = 20.63$.

The three-dimensional flow results (analyzable flow volume of $x/d = 1.1$ to 17.7, $y/d = -9.1$ to 9.1 and $z/d = 3.4$ to 19.5) based on the V3V-measurements for this test case are depicted in Fig. 193 for several perspectives. In contrast to the other three-dimensional flow results depicted in this thesis, the present visualizations show the time-averaged flow field and its corresponding mean cylinder deformation. The time-averaged results are chosen due to the high velocity fluctuations present in the three-dimensional flow field. Therefore, not enough data for the phase-averaging procedure are available to provide a sufficiently accurate quasi-periodic 3D flow field.

The time-averaging over all 550 V3V measurements provide no smooth velocity iso-surfaces in the wake of the deformed cylinder. Nevertheless, similar to the mean results based on the PIV measurements the expansion of the wake is visible in Fig. 193.

The POD analysis for the first two POD modes of FSI-PfS-4*a* is presented in Fig. 194. The influence of the characteristic 2P vortex street is obvious in the distributions of the kinetic energy referring to the streamwise velocity u in Figs. 194a and b. Here, the four shedding vorticies generated within an oscillation period are visible in the first and second POD mode. As

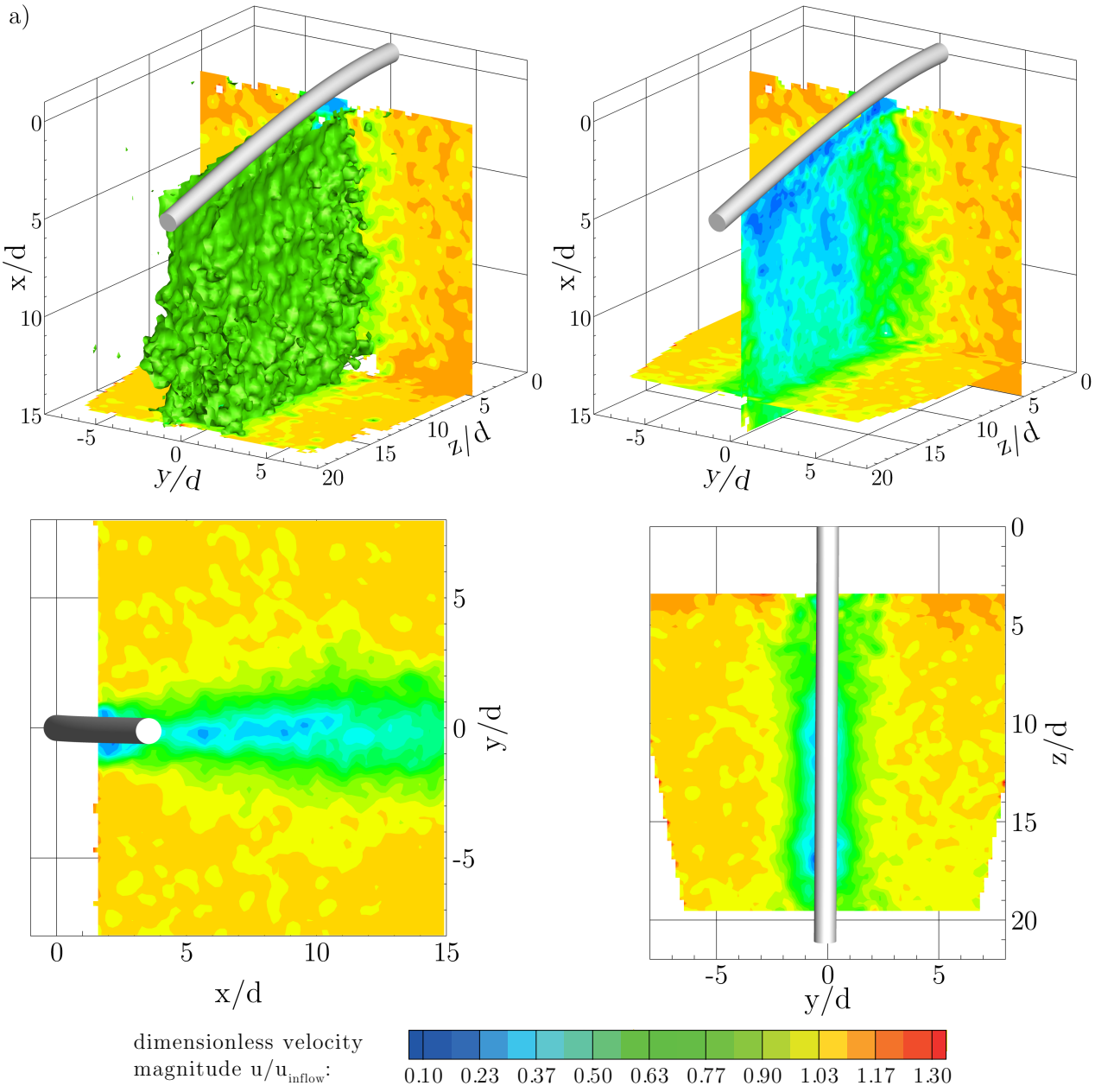

Figure 193: FSI-PfS-4*a*: Experimental time-averaged flow results based on the V3V and the structural results, iso-surfaces depict the velocity magnitude at $|\mathbf{u}|/u_{\text{inflow}} = 0.79$.

expected, the highest kinetic flow energy for this velocity component is found in the vicinity of the moving cylinder. In comparison to the fixed configuration of FSI-PfS-4*a* (see Section 8.1.3) the strong impact of the FSI coupling on the flow field is clearly recognizable. While in the rigid configuration only two vorticies are present side by side, in the FSI case four vorticies are found. In contrast, the cross-flow velocity component v (depicted in Figs. 194c and d) seems to be less affected by FSI. Similar to the fixed configuration broad areas of high kinetic energy are distributed in the wake of the cylinder. Due to the moving cylinder these areas are much more expanded in y-direction, since the y-momentum exchange in the wake region is increased in the FSI case. Furthermore, the shape of the areas of high kinetic energy far downstream of the flexible cylinder reveals a significant extension (buckle) in negative x-direction. This

leads to the assumption that the inner vorticies are slightly slower convected downstream in comparison to the lateral vorticies next to the fast bulk flow. The POD analysis of the vorticity component ω_z is shown in Figs. 194e and f. Again the mostly affected region of the kinetic energy is found in the wake of the cylinder and in the regions where the vorticies are generated and shed. Further downstream the expansion of the wake and the corresponding drift of the vorticies apart are visible. This phenomenon is not visible in the vorticity-based POD analysis of the fixed configuration, where the areas of high kinetic energy are smaller than in the FSI case.

Despite the significant changes of the system characteristics (especially the vortex shedding mode) the comparison of the total energy content of the fixed ($k_{\mathrm{abs,all}} = 652.74$ m^2/s^2, $k_{\mathrm{rel,all}} = 100\%$) and the flexible cylinder ($k_{\mathrm{abs,all}} = 732.14$ m^2/s^2, $k_{\mathrm{rel,all}} = 100\%$) configurations yield only a small increase of the energy due to the FSI coupling. Since the vortex shedding frequency is not measured in the fixed configuration case it only can be assumed that the vortex shedding frequency is not significantly altered due to the FSI coupling while in the other studied test cases FSI-PfS-1x, 2x and 3x a significant change in the frequency is observed. There, the flexible plate behind the front cylinder acts like a splitter plate and a stronger influence on the flow and the kinetic energy content is expected. Another indication that the FSI effect in FSI-PfS-4a is not that eminent to the flow is given with the energy content of the first and second POD modes which only contain 38% of the total kinetic energy of FSI-PfS-4a with $k_{\mathrm{abs,1st}} = 161.51$ m^2/s^2 ($k_{\mathrm{rel,1st}} = 22.1\%$) and $k_{\mathrm{abs,2nd}} = 116.17$ m^2/s^2, ($k_{\mathrm{rel,2nd}} = 15.9\%$). Nevertheless, in comparison the kinetic energy of the higher POD mode is significantly lower (e.g., under 4% of the total kinetic energy for the third POD mode, see Fig. 204). That suggests that the vortex shedding together with the impressed fluid motion due to the motion of the cylinder is still energetically dominant compared to other (e.g., turbulent) flow phenomena.

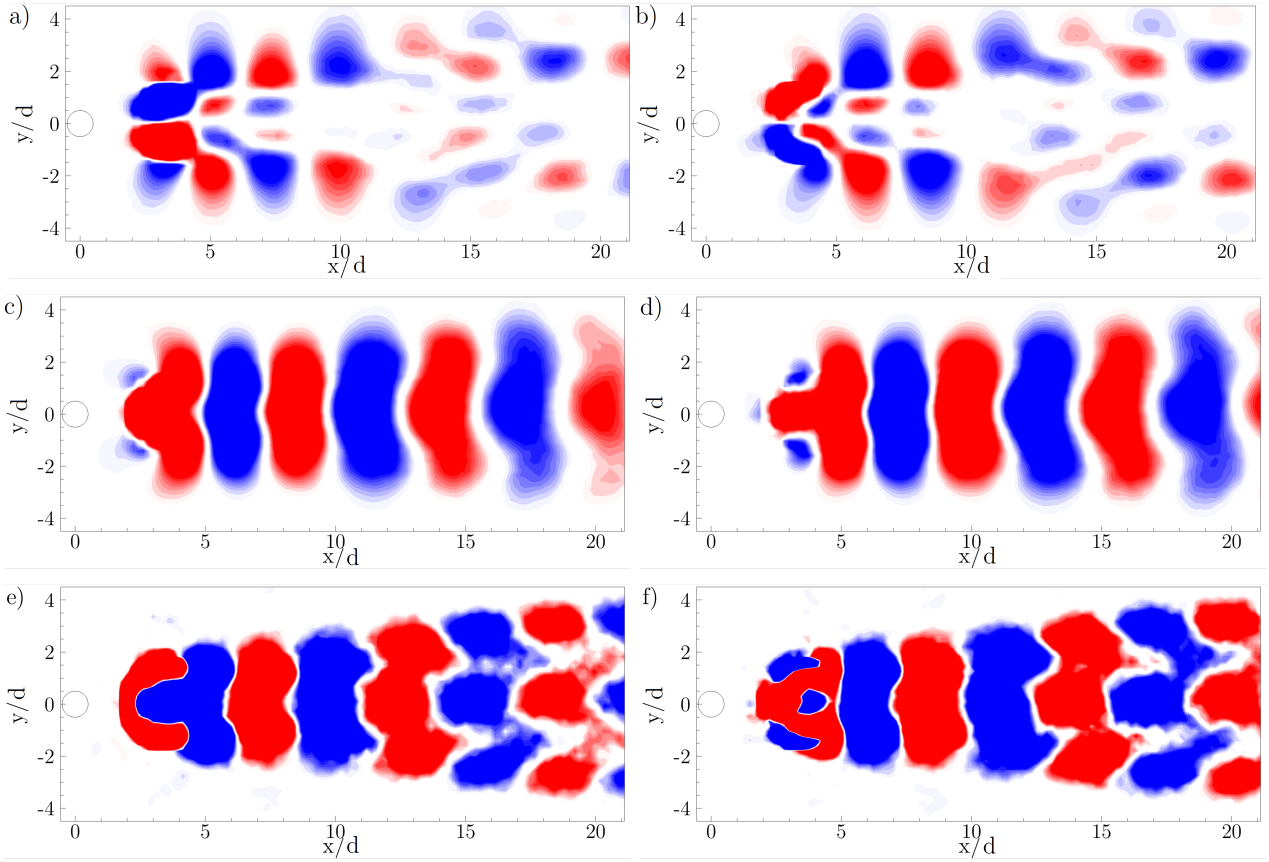

Figure 194: FSI-PfS-4*a*: POD analysis of the two-dimensional flow fields in the measurement plane at $z/d = 20.63$, a) velocity component u, first mode; b) velocity component u, second mode; c) velocity component v, first mode; d) velocity component v, second mode; e) vorticity component ω_z, first mode; f) vorticity component ω_z, second mode.

FSI-PfS-4b - Structural results

In the second test case FSI-PfS-4*b* the flexible cylinder (again fixed at the backplate, free cylinder tip) is surrounded by eight rigid cylinders in a 3×3 arrangement. Again the structural response as a function of the inflow velocity up to $u_{\text{inflow}} = 1.9$ m/s is averaged over 10 single measurements and presented in Fig. 195 for the displacements and in Fig. 196 for the swiveling frequencies and Strouhal numbers.

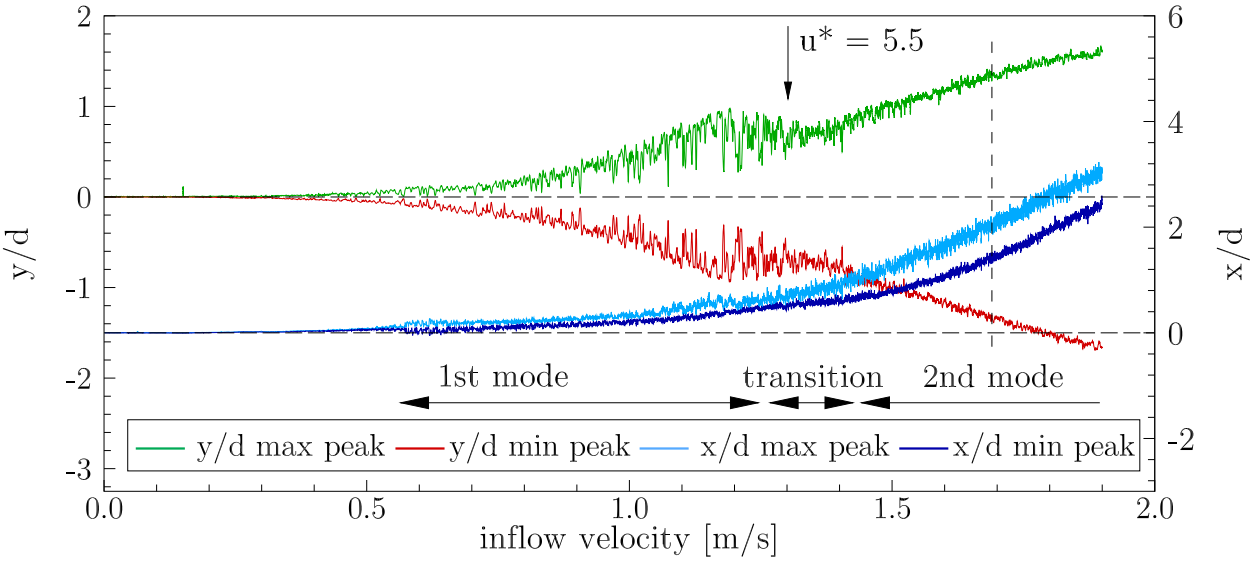

Figure 195: FSI-PfS-4*b*: Averaged maximal/minimal structural deflections as a function of the inflow velocity.

In contrast to FSI-PfS-4*a* the FSI coupling starts earlier for this case at an inflow velocity of $u_{\text{inflow}} \approx 0.4$ m/s with tiny but almost periodic oscillations of the cylinder tip. The following slow increase of the y/d-deflections is characterized by strong disturbances. Here, the cylinder tip is deflected in an asymmetric and aperiodic way, exhibiting the influence of the surrounding rigid cylinders. Especially the first row of these cylinders is assumed to generate strong flow fluctuations in their wake. These flow structures hit the flexible cylinder and amplify or hinder its deformation. At an inflow velocity of about $u_{\text{inflow}} = 1.2$ m/s this progress leads to a local extrema of the deflections ($y/d \approx \pm 0.95$) and a slight decrease in the y/d-deflections is observed for inflow velocities above this value. Here, the x/d-deflections range between $x/d \approx 0.3$ and $x/d \approx 0.8$. By reaching an inflow velocity of $u_{\text{inflow}} = 1.35$ m/s the y/d-deflections again start to increase. Furthermore, the fluctuations in the structural response decrease. The increase of the displacements (y/d and x/d) of the cylinder tip is characterized by large, symmetric and periodic deformations in the measurement plane. The almost linear increase of the y/d-deflections from $y/d \approx \pm 0.73$ at $u_{\text{inflow}} = 1.35$ m/s to $y/d \approx \pm 1.66$ at $u_{\text{inflow}} = 1.9$ m/s exhibit a gradient of about $(\delta(y/d)/\delta u) = 1.69$ 1/(m s^{-1}). In the same interval the x/d-deflections are found to be $(x/d)_{\text{min}} = 0.36$ to $(x/d)_{\text{max}} = 1.15$ at $u_{\text{inflow}} = 1.35$ m/s and $(x/d)_{\text{min}} = 2.20$ to $(x/d)_{\text{max}} = 3.43$ at $u_{\text{inflow}} = 1.9$ m/s. In comparison to FSI-PfS-4*a* the y/d-deflections are increased while the x/d-displacements are decreased in the case FSI-PfS-4*b*. This is reasonable since the y/d-momentum is not impeded by the outer bulk flow (in contrast to FSI-PfS-4*a*)

but moves through the wake of the first cylinder row, while the x/d-deflections are limited due to the third cylinder row.

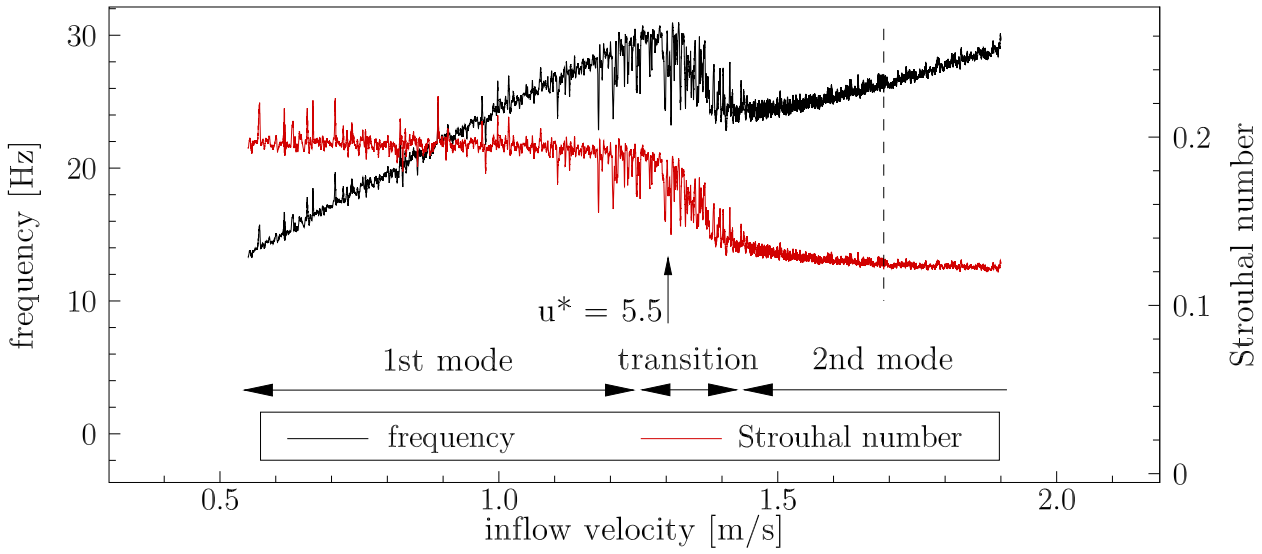

Figure 196: FSI-PfS-4*b*: Averaged frequency and Strouhal number as a function of the inflow velocity.

The oscillation frequency of the structural response shows a similar pattern as the y/d-deflection. The first phase is characterized by a linear rise of the frequencies from $f = 13.3$ Hz at $u_{\text{inflow}} = 0.55$ m/s to a maximal frequency of $f = 29.49$ Hz at $u_{\text{inflow}} = 1.27$ m/s. With the further increase of the velocity a slight decrease in the frequency to $f = 24.33$ Hz at $u_{\text{inflow}} = 1.47$ m/s is found. In the following interval the frequencies again increase linearly to 28.85 Hz at $u_{\text{inflow}} = 1.9$ m/s with minor fluctuations. In contrast to FSI-PfS-4*a* no significant particular structural response (like the abrupt increase of the swiveling frequency in FSI-PfS-4*a*) is noticed. Furthermore, the eigenfrequency of the structure (flexible cylinder, without surrounding fluid) at $f_{4x,1} = 35.66$ Hz is not reached within the present inflow velocity interval.

With $u_{\text{inflow}} = 1.69$ m/s the same inflow velocity as in FSI-PfS-4*a* is chosen for the detailed analysis of this test case. The time histories of the structural deflections are shown in Fig. 197 for the center of the cylinder near its tip at $(z/d) = 20.63$. This time-dependent signal is quasi-periodic but exhibits large amplitude variations over several cycles. With a time-averaged maximal peak $(y/d)_{\max} = 1.25$ and a time-averaged minimal peak $(y/d)_{\min} = -1.27$, the standard deviations of all positive and negative peaks are calculated to be $\sigma((y/d)_{\max}) = 0.103$ (8.24%) and $\sigma((y/d)_{\min}) = 0.099$ (7.80%) over all 4990 recorded periods. In the x-direction the cylinder center swivels with minimal values of $(x/d)_{\min} = 2.32$ and maximal values of $(x/d)_{\max} = 3.00$. Again the mismatch to the measurement series of the structural response as a function of the inflow velocity (Fig. 195) to the fixed velocity case is present similar to FSI-PfS-4*a*. As already mentioned for FSI-PfS-4*a* the measurements for the fixed inflow velocity are performed after a long settlement phase which is also necessary for FSI-PfS-4*b*. This phase is characterized by the slow bending of the flexible cylinder until it reaches a quasi-periodic swiveling state. Since the integral drag forces are assumed to be lower in the first measurement

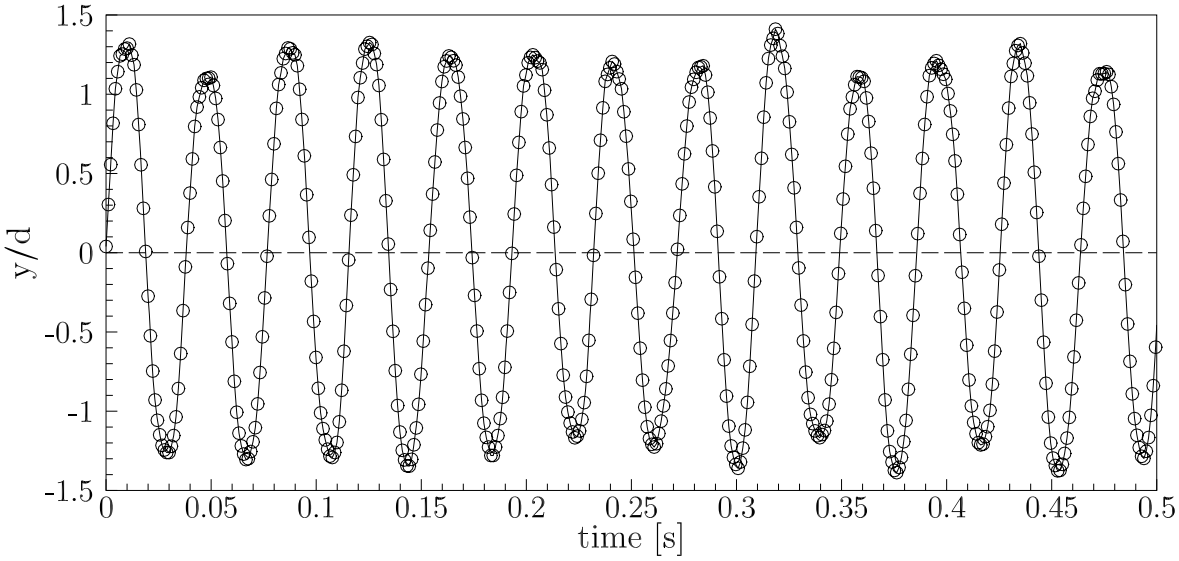

Figure 197: FSI-PfS-4*b*: Experimental structural results: Time history of the structural deflections (extract) for the center of the flexible cylinder at the measurement plane $(z/d) = 20.63$.

series (Fig. 195) the x/d-deflections are smaller at the inflow velocity $u_{\text{inflow}} = 1.69$ m/s. The mean swiveling frequency at this inflow velocity is found to be $f = 26.28$ Hz (St = 0.124) and its standard deviation $\sigma(f) = 1.18$ Hz (4.49%).

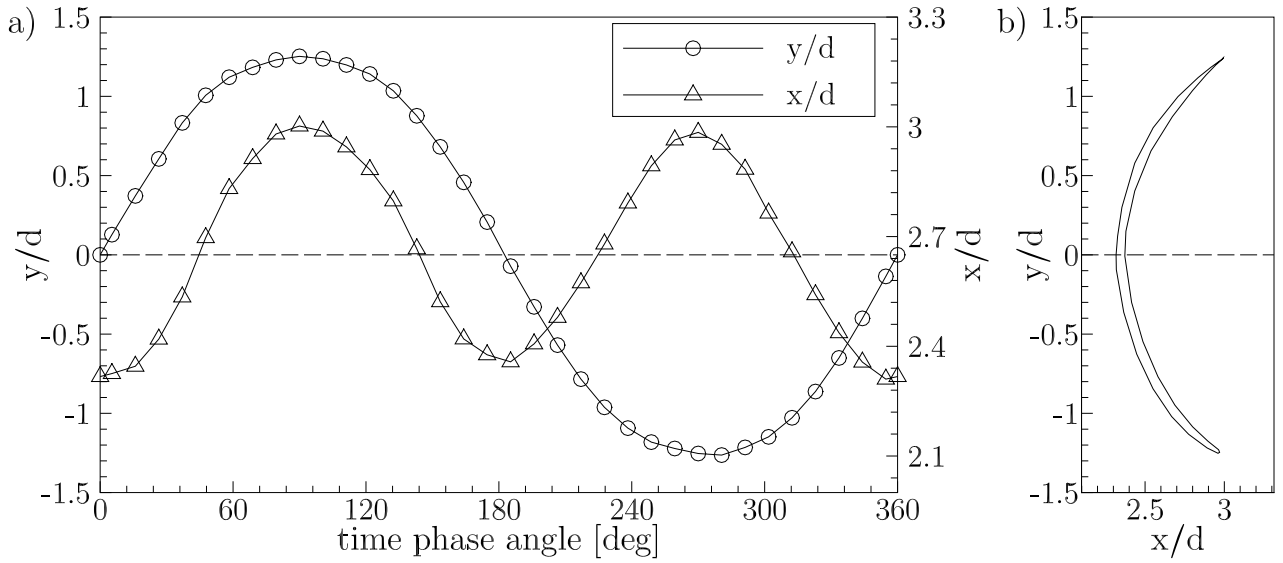

Figure 198: FSI-PfS-4b: Experimental structural results: a) phase-averaged reference period of the structure for the x/d- and y/d-deflections, b) xy-motion of the structural deflections, both for the center of the cylinder at $z/d = 20.63$.

The phase-averaged structural results are presented in Fig. 198a. The mean swiveling period consists of 34 phase-averaged parts calculated out of the 4990 recorded periods. The y/d-deflections show a nearly sinusoidal behavior around zero, while for the x/d-displacements the frequency of the sinusoidal signal is doubled and the deflections are shifted to an offset of $x/d = 2.65$. The motion path of the cylinder tip is characterized by an open "C"-shape as shown in Fig. 198b.

FSI-PfS-4b - Flow results

The time-averaged flow around and within the cylinder array is presented in Fig. 199a for the measurement plane $z/d = 20.63$ close to the channel wall. In front of the first cylinder row (rigid) the stagnation points of each cylinder are visible. Due to the blockage of the channel by the cylinders the flow on their upper and lower sides is accelerated. According to the averaging over all measurements an almost symmetric velocity distribution to the line $y/d = 0$ is observed. In the second cylinder row lower velocities are found due to the wake of the first row. Moreover, weaker acceleration regions are formed at the lateral cylinders. The flexible cylinder is illustrated in its average x/d- and y/d-position. The large deflection in x-direction is a consequence of the high fluid loads on the entire cylinder. Remarkable is an almost constant mean velocity around the moving structure. Similar to the mean velocity distribution of the first test case FSI-PfS-4*a* (Fig. 189) the range of the moving structure is assessable. The rigid cylinder in the middle of the third row in the wake of the flexible cylinder is surrounded by a region of small fluid velocities with respect to the mean values. Furthermore, the accelerating flow areas in the third row are present only between the cylinders in contrast to the first row where each cylinder possesses its own upper and lower acceleration region. Behind the cylinder array a pronounced wake region is recognizable. At the backside of the cylinders lower mean velocities are found, while higher velocities are obtained behind the cylinder gaps. At the far end of the measurement area a large and almost uniform wake flow is present.
The time-averaged distribution of the Reynolds shear stress $\overline{u'v'}$ is given in Fig. 199b. On the upper and lower sides of each rigid cylinder the influence of the shear layers and the wake behind these structures on the Reynolds stresses is clearly visible. In the vicinity of the flexible cylinder the Reynolds shear stresses increase and are limited to the region of the cylinder trajectory. This result indicates that the fluctuations increase due to the moving cylinder tip and are highly correlated to it.
The comparison of the flow distributions of the FSI case to the rigid configuration (refer to Section 8.1.3) reveals the influence of the flexible cylinder in the center of the 3×3 configuration to the mean flow field of the coupled system. In the rigid configuration the flow around the central cylinder behaves as expected, while in the FSI case especially the center region is affected by the moving structure. In contrast, the outer flow in the vicinity of the lateral cylinders is less affected by the FSI coupling as well as the wake region of the central cylinder.

The combined phase-averaged flow and structure results are shown in Figs. 200 and 201 for six time phase angles (16, 78, 141, 204, 266 and 326 deg). The velocity distributions are very similar to the time-averaged results in Fig. 199. A phase-dependent change of the velocity field is visible owing to the alternating rise and fall of the acceleration regions between the cylinders in the third row of the array. Furthermore, by the movement of the free cylinder the surrounding fluid is accelerated or decelerated according to the phase angle of the period. Due to the high fluctuations of the fluid velocities and the large structural velocities and accelerations within one period, the spatial and temporal resolution of the phase-averaged results are decreased (blurring). Therefore, no other significant changes in the flow fields are noticeable. Similar to the phase-averaged result of FSI-PfS-4*a* more accurate measurement techniques (in time and

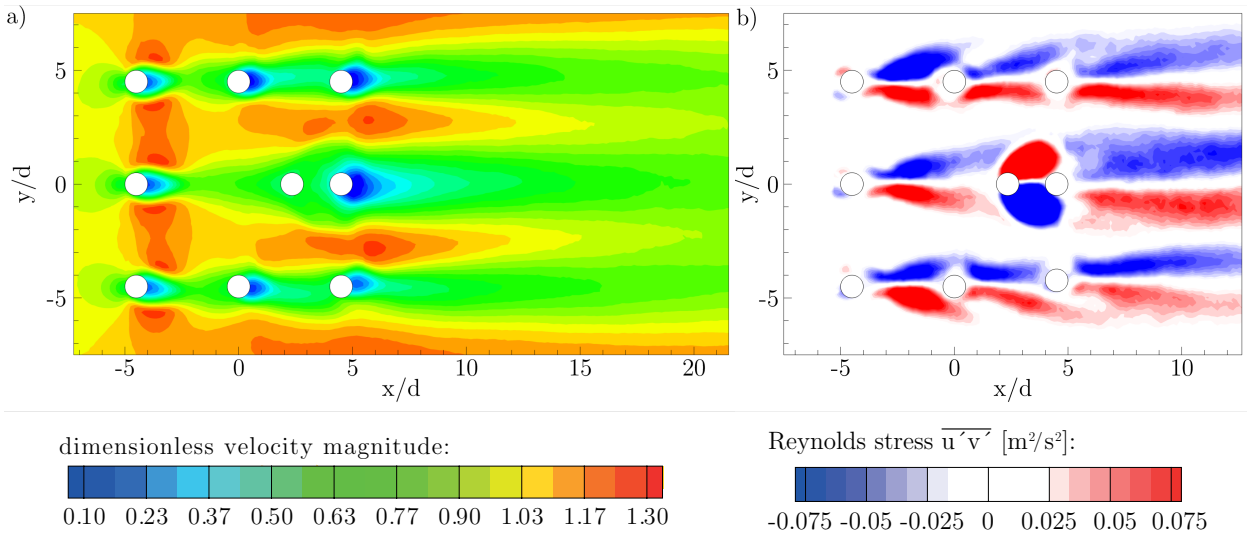

Figure 199: FSI-PfS-4*b*: Time-averaged PIV results of at $z/d = 20.63$ for a) dimensionless velocity magnitude and b) Reynolds shear stress $\overline{u'v'}$.

space) and a larger amount of data points applied in the phase reconstruction would enhance the flow results but require additional efforts in the acquisition and processing of the PIV measurements.
In Fig. 202 the three-dimensional flow results in the flow volume of $x/d = 4.2$ to 23.3, $y/d = -9.9$ to 9.9 and $z/d = 1.4$ to 16.5 are depicted. These time-averaged results are based on the 550 single V3V-measurements for this test case. Similar to the three-dimensional flow results of FSI-PfS-4*a* the time-averaging over all 550 V3V measurements yields no smooth velocity distributions and iso-surfaces in the wake of the cylinder array. Again the increased velocity fluctuations and the limited amount of flow data for the averaging are responsible for the rough flow distribution. Clearly visible are the regions of higher velocities downstream the cylinder gaps.

More remarkable are the results of the POD analysis for the first two POD modes of FSI-PfS-4*b* depicted in Fig. 203. Although the phase-averaged flow results do not offer a clear insight into the present flow situation, the POD analysis reveals that a correlated vortex shedding is also present in this case. In Figs. 203a and b the distributions of the kinetic energy referring to the streamwise velocity u are given.

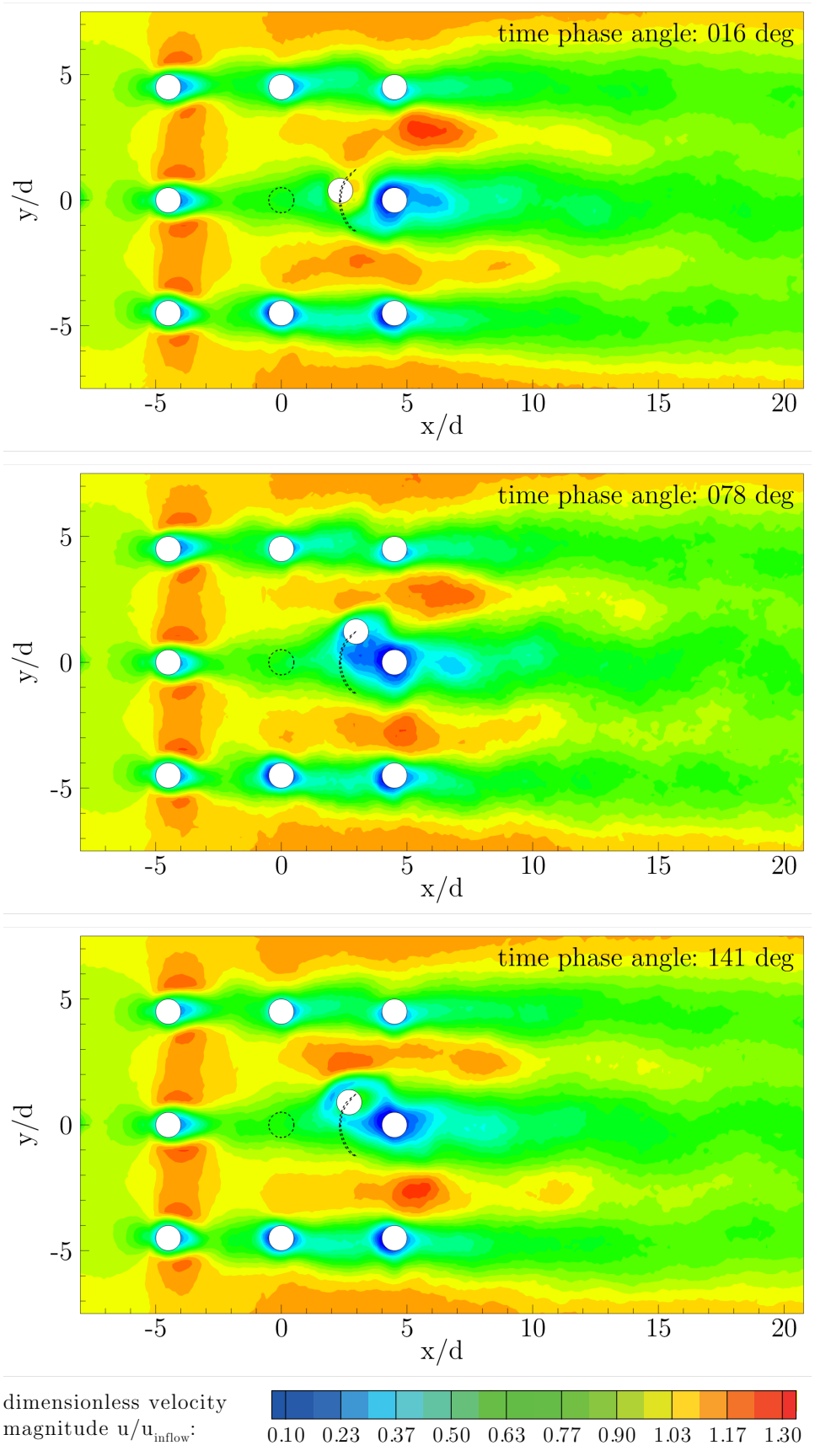

Figure 200: FSI-PfS-4*b*: Experimental phase-averaged flow and structural results for the first half of the reference period.

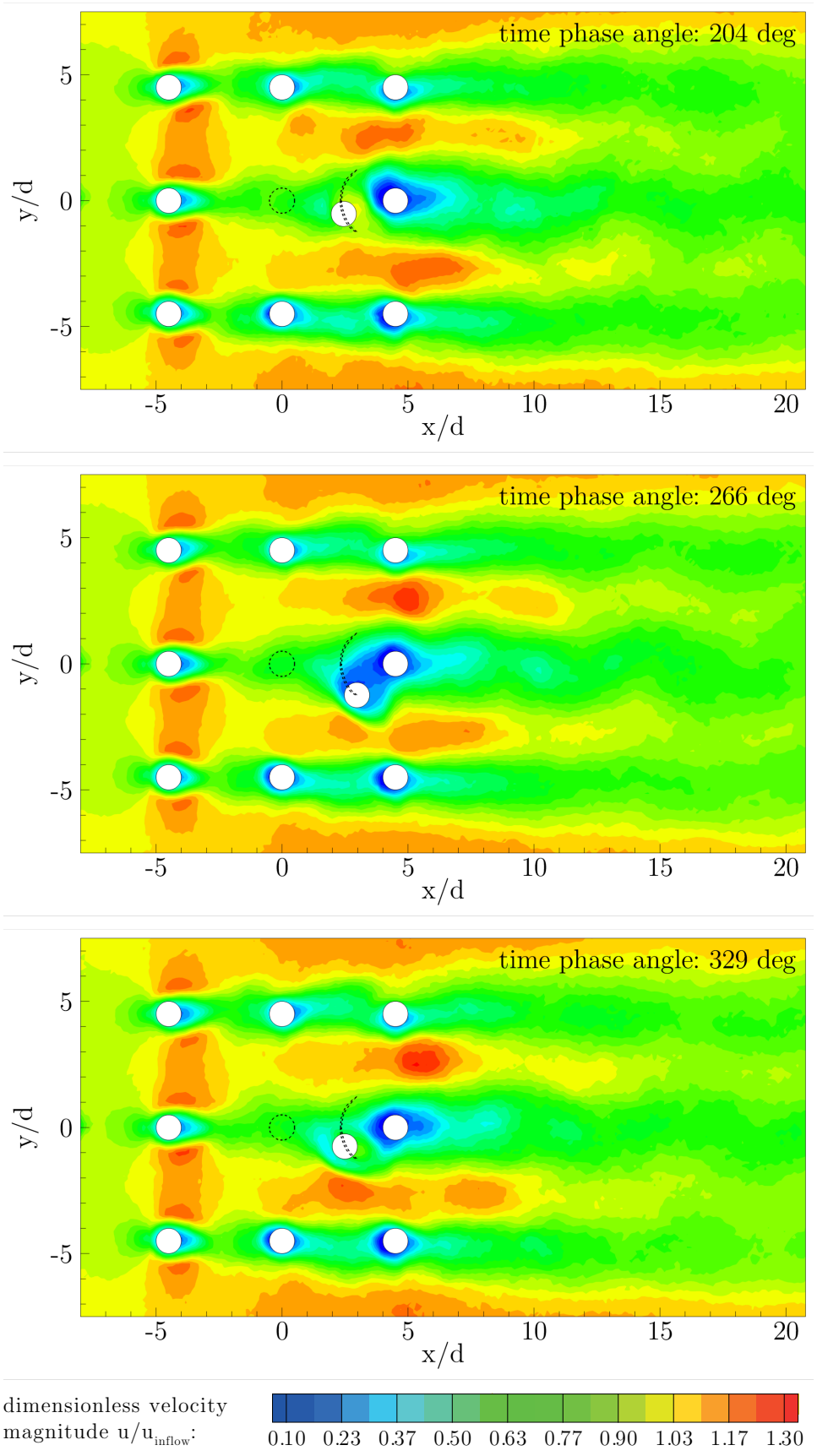

Figure 201: FSI-PfS-4*b*: Experimental phase-averaged flow and structural results for the second half of the reference period.

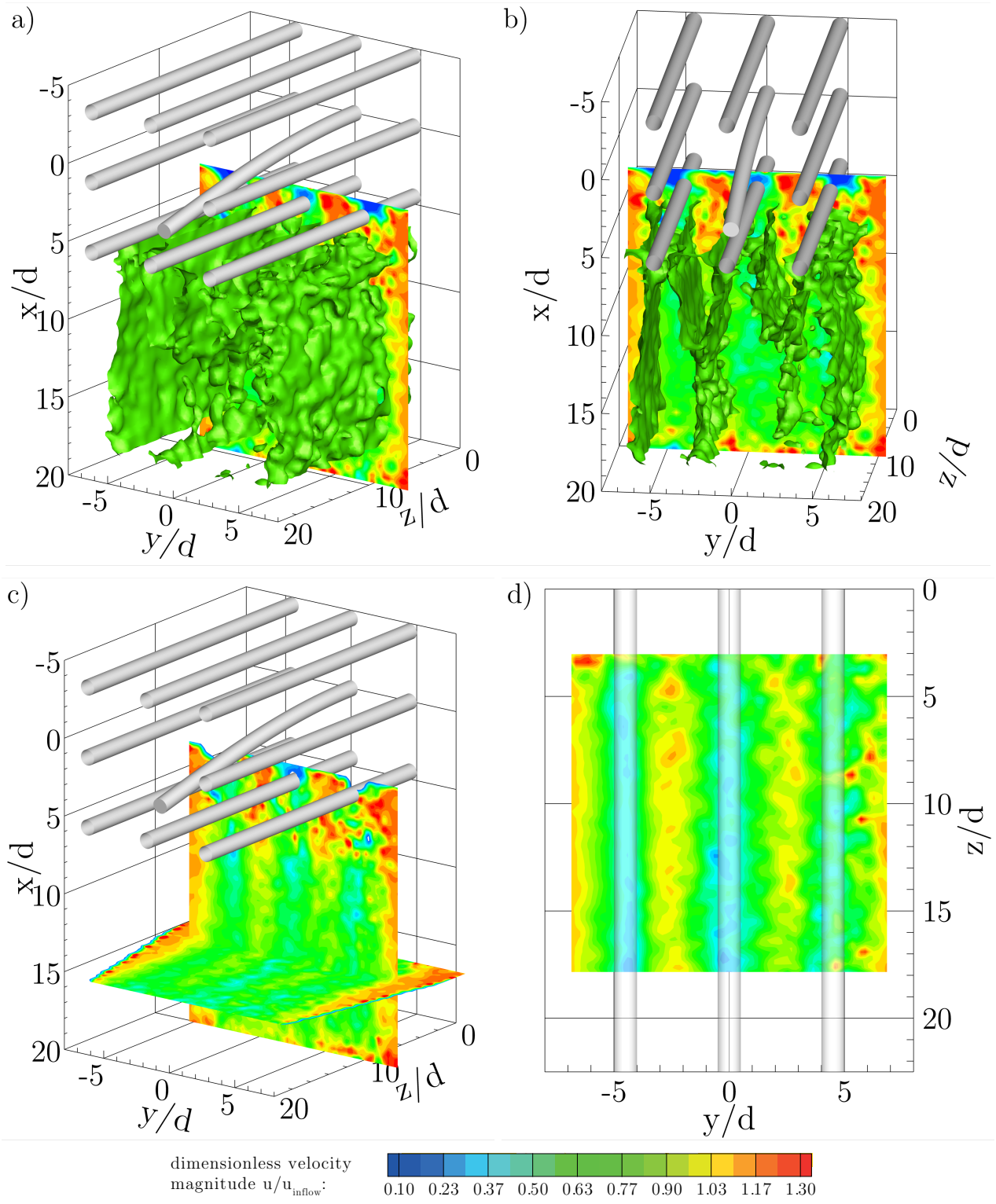

Figure 202: FSI-PfS-4*b*: Experimental time-averaged flow results based on the V3V measurements and the structural results, iso-surfaces depict the velocity magnitude at $|\mathbf{u}|/u_{\text{inflow}} = 0.79$.

In both modes an alternating pattern which is characteristic for a vortex street is present. Especially downstream of the center of the cylinder array regions of high kinetic energy are found. Further downstream past the array the expansion of the wake area is visible. In this region signs of a 2P vortex shedding mode (in the wake the small inner areas of kinetic energy correspond to the inner vorticies while the lateral areas are related to the larger lateral vorticies) are present similar to the flow behavior found in FSI-PfS-4*a*. It remains unclear whether this effect is caused by the middle cylinder in the third row or by the motion of the flexible cylinder. The POD based on the cross-flow velocity component v is shown in Figs. 203c and d. Here, large areas of kinetic energy are alternately expanding downstream of the array. Again the unusual buckling shape of the region far downstream indicates the presence of the 2P vortex shedding mode and a slightly lower convection velocity of the inner vorticies compared to the lateral vorticies. Figures 203e and f refer to the POD analysis of the vorticity component ω_z. Since this flow quantity is directly related to the velocity gradients present in the flow field, most of the flow disturbances are found close to the trajectory of the flexible cylinder. Behind the cylinder array broad areas of high kinetic energy are observed referring to the correlated vortex shedding from the moving cylinder. Outer regions (e.g., close to the lateral cylinders or the vorticies generated by the first cylinder row) seem to be energetically less important for this system state. In comparison to the rigid configuration this is a significant change. There, the energy is concentrated in the first two cylinder rows owing to the vortex shedding, while in the FSI case the largest energy refers to the motion and the vortex shedding from the moving cylinder. The observation that the FSI coupling has a strong impact on the flow situation is supported by comparing the total energy content of the fixed configuration ($k_{\mathrm{abs,all}} = 2385.08\ \mathrm{m^2/s^2}$, $k_{\mathrm{rel,all}} = 100\%$) to the FSI case ($k_{\mathrm{abs,all}} = 3417.36\ \mathrm{m^2/s^2}$, $k_{\mathrm{rel,all}} = 100\%$). Here, an increase of the kinetic energy of about 43% for the FSI configuration in relation to the fixed case confirms its impact on the flow. It can be assumed that this increase is the consequence of the strong impact of the moving cylinder to the flow structures generated at the rigid cylinders. Here, the vortex shedding is extensively disturbed coming along with the increase of the velocity fluctuations. Furthermore, the first and second POD modes only contain together 13% of the total kinetic energy with $k_{\mathrm{abs,1st}} = 279.05\ \mathrm{m^2/s^2}$ ($k_{\mathrm{rel,1st}} = 8.2\%$) and $k_{\mathrm{abs,2nd}} = 173.25\ \mathrm{m^2/s^2}$, ($k_{\mathrm{rel,2nd}} = 5.1\%$). It can be assumed that large amounts of the kinetic energy are stored in the dependent but uncorrelated flow fluctuations generated by the cylinder array and the moving central cylinder.

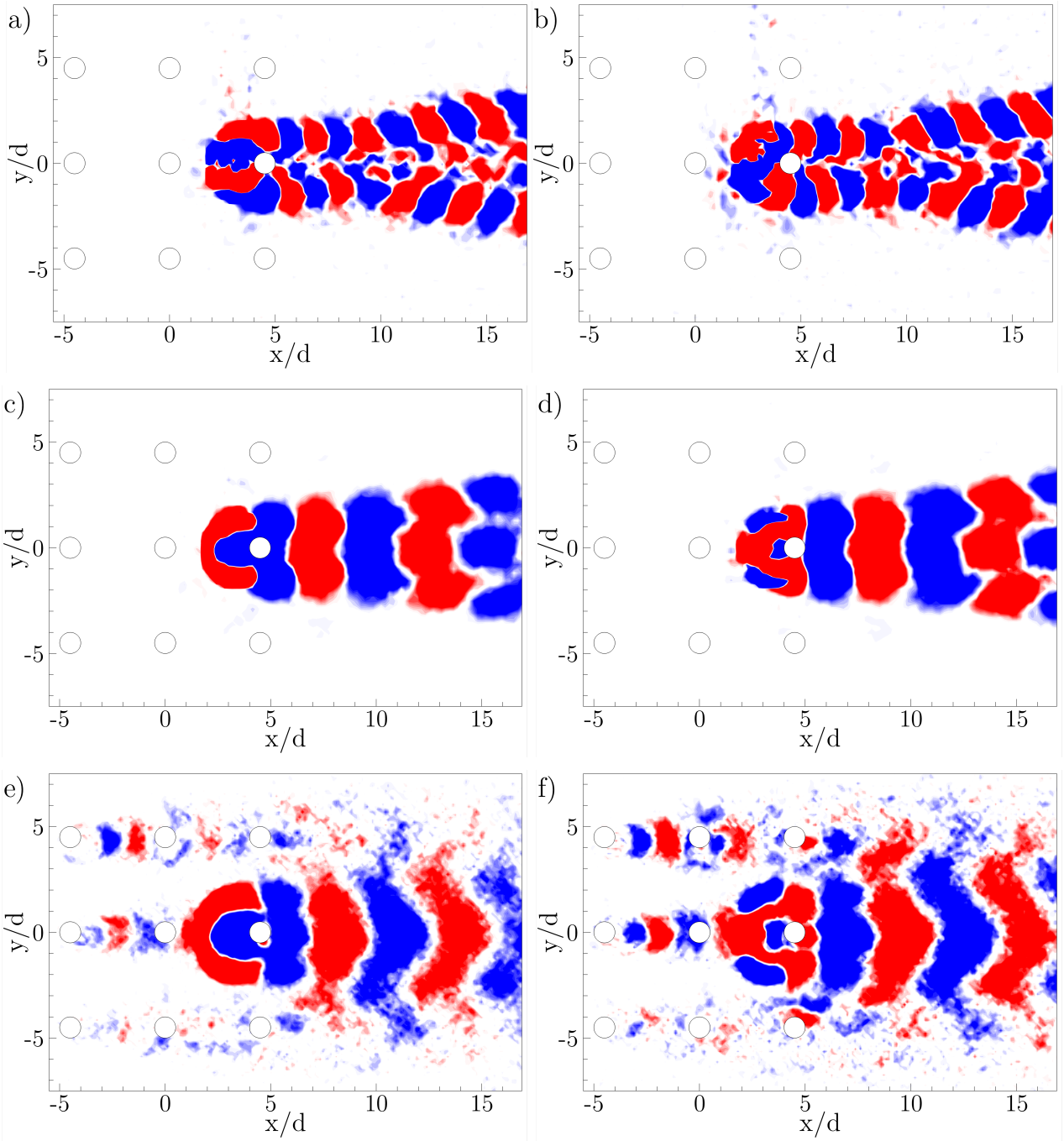

Figure 203: FSI-PfS-4*b*: POD analysis of the two-dimensional flow fields in the measurement plane at $z/d = 20.63$ a) velocity component u, first mode; b) velocity component u, second mode; c) velocity component v, first mode; d) velocity component v, second mode; e) vorticity component ω_z, first mode; f) vorticity component ω_z, second mode.

Conclusions - FSI-PfS-4x

These last test cases FSI-PfS-4x are developed with respect to an application-oriented FSI benchmark. In the two cases the flexible structure is a long, thin polyethylene cylinder (bending stiffness $K_B = 2.43$) which is exposed to a free-stream flow (FSI-PfS-4a) and a disturbed flow within a 3 $\times$ 3 arrangement (FSI-PfS-4b). Both configurations show a strong dependence on the inflow velocity. Due to the different configurations both test cases show individual structural responses to the increasing inflow velocities. FSI-PfS-4a is characterized by large fluctuations in the structural deflections for low inflow velocities. By passing a critical inflow velocity the structural motion gets more stable and its response (two pair (2P) vortex shedding mode) is comparable to experimental investigations carried out on elastically mounted cylinders (Blevins, 1990). In this mode the motion of the structure causes the shedding of four alternately rotating vorticies within a period. In FSI-PfS-4a this 2P flow state is characterized by large quasi-periodic deflections of the cylinder tip slightly smaller than one cylinder diameter in y-direction and very large deflections in x-direction ($2.8 < x/d < 3.9$) and mild standard deviations ($\approx 5\%$). The swiveling frequency is high and in the order of 30 Hz.

Test case	**FSI-PfS-4a**	**FSI-PfS-4b**
behavior	3D	3D
bending modes	1st mode, 2nd mode	1st mode, 2nd mode
bending shapes	'8'	'('
bending stiffness K_B	2.43	2.43
u_{inflow} [m/s]	1.69 m/s	1.69 m/s
symmetry	✓	✓
f [Hz]	29.39	26.28
$\sigma(f)$	$\pm 2.11\%$	$\pm 4.49\%$
St	0.139	0.124
$(x/d)_{\max}$	3.85	3.00
$(x/d)_{\min}$	2.84	2.32
$\sigma(x/d)$	$\pm 5.10\%$	$\pm 4.38\%$
$(y/d)_{\max}$	0.903	1.25
$(y/d)_{\min}$	-0.895	-1.27
POD energy content $k_{\text{abs,all}}$	732.14 m^2/s^2	3417.36 m^2/s^2

Table 23: Summary of FSI-PfS-4x.

The same flexible cylinder applied in FSI-PfS-4a is surrounded by eight rigid cylinders in a 3×3 arrangement in the second test case FSI-PfS-4b. In comparison to the free-stream case of FSI-PfS-4a the additional structures nearby reveal a strong influence on the structural behavior of the elastic cylinder. Especially for higher inflow velocities the structural response is quasi-periodic with large deflections in x- ($2.3 < x/d < 3.0$) and y-direction ($-1.3 < x/d < 1.3$). For the detailed investigations at the inflow velocity $u_{\text{inflow}} = 1.69$ m/s the motion path of the cylinder tip is described by a distorted eight in FSI-PfS-4a, while the response in FSI-PfS-4b forms an open "C". A summary of the mean values of the experimental results is given in Table 23. According to the high oscillation frequencies of the cylinder in the order of 30 Hz and the associated large accelerations and velocities in both physical domains and both test

configurations, the phase-averaged flow field measurements provide only a limited insight into the underlying physics of the system.

The classification into the excitation mechanisms according to Section 3 is rather difficult. In Moretti (1993) the lock-in of the structural deflection to a vortex-shedding excitation is observed near the reduced velocity of $u^* = u_{\text{inflow}}/(f_s\ d) = 5$ for an elastically mounted rigid cylinder. That means that first the EIE mechanism is present due to the velocity fluctuations of the inflow. Near the reduced velocity $u^* \approx 5$ (Blevins, 1990; Moretti, 1993; Williamson and Govardhan, 2004) the structural deflections lock-in to the vortex shedding frequency ($f_{\text{s}} = f_{\text{vs}}$) and generate the 2P vortex shedding mode. In this state the vortex shedding at the cylinder acts as a flow instability and refers to the IIE mode.
According to the present set-up of FSI-PfS-4*a* and the corresponding differences (present case: self-excited oscillation of an one-sided fixed flexible cylinder; common literature case: forced oscillation of an elastically mounted rigid cylinder) to the literature cases mentioned above, this mode transition from EIE to IIE occurs at the reduced velocity of $u^* = 6.7$ for FSI-PfS-4*a* (inflow velocity of about $u_{\text{inflow}} = 1.15$ m/s). With the increasing structural deflections the flow is strongly influenced by the motion of the flexible cylinder (refer to the comparison of the fixed to the FSI configuration) indicating the MIE mode. Therefore, it can be assumed that a simultaneous excitation of IIE and MIE is present for higher inflow velocities ($u_{\text{inflow}} >$ 1.15 m/s). Since the eigenfrequency of the flexible cylinder $f_{4\text{x,1st}} = 35.66$ Hz is not reached in the measurements, no further insights to the excitation mode of FSI-PfS-4*a* can be given.
In FSI-PfS-4*b* the onset of FSI also refers to the EIE mode. In contrast to FSI-PfS-4*a* the velocity fluctuations at the inflow are assumed to be less responsible for the weak structural oscillations present for low inflow velocities (0.4 m/s$> u_{\text{inflow}} <$ 1.3 m/s). The extraneous excitation due to the surrounding cylinders are assumed as the main excitation source in this system state present over a broad inflow velocity range. The mode transition from EIE to IIE takes place at a reduced velocity of $u^* \approx 5.5$ ($u_{\text{inflow}} \approx 1.3$ m/s) but not so distinguishable as observed in FSI-PfS-4*a*. The presence of this transition is evident by the decrease of the fluctuations of the structural deflections and the swiveling frequencies in the following system state. That means that the influence of the irregular excitations caused by the surrounding cylinders gets weaker, while the lock-in vortex shedding becomes the dominant excitation source for inflow velocities over $u_{\text{inflow}} > 1.3$ m/s. Similar to the conclusions for FSI-PfS-4*a* the excitation modes IIE and MIE are assumed to be present simultaneously for these higher inflow velocities. Again the comparisons between the fixed configuration and the FSI case reveal strong changes in the flow field and support this assumption. Additionally, the POD analysis reveals that only a small amount of the total kinetic energy corresponds to the motion and the vortex shedding of the flexible cylinder (see Fig. 204). It can be assumed that the large part of the kinetic energy refers to uncorrelated (to the cylinder deflection) flow phenomena (e.g., turbulence, vortex shedding at the lateral cylinders). In contrast, most of the total kinetic flow energy present in FSI-PfS-4*a* is rather concentrated to the cylinder motion and the vortex shedding from this cylinder.

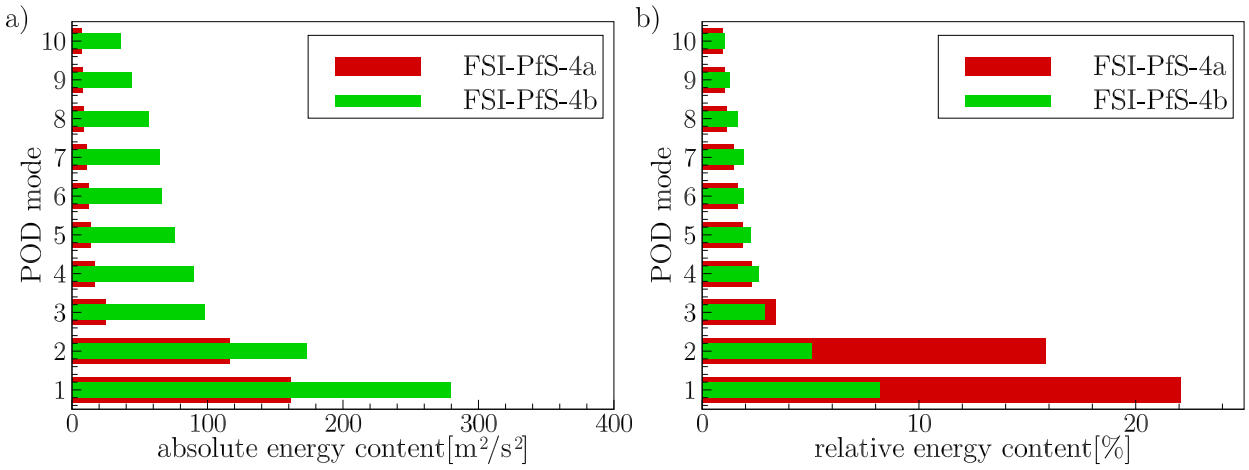

Figure 204: FSI-PfS-4x: POD results.

10.2. Numerical results

In the previous subsections the experimental results of the test cases developed in the present thesis are presented and discussed. The following subsections show the corresponding numerical results of each test case. All simulation results are obtained by the coupling of ANSYS® CFX 14.0 for the flow solution and ANSYS® Mechanical 14.0 for the structural predictions. The coupling (in detail: the transfer of the structural deflections, the fluid loads and the related mesh deformations) between both solvers is performed by ANSYS® MFX 14.0. The simulations are based on the boundary conditions and the numerical grids described in the numerical set-up in Section 9 and the material properties (see Table 24) obtained by the structural tests presented in Section 8.2[20].

material	ρ [kg m^{-3}]	E [MPa]	ν [-]	test cases
EPDM rubber	1360	16	0.48	FSI-PfS-1a, 3a
Para-rubber	1090	3.25	0.48	FSI-PfS-1c, 2x and 3b
Polyamide	1425	580	0.40	FSI-PfS-1b
Polyethylene	930	800	0.42	FSI-PfS-4x
Steel	7850	$2 \cdot 10^5$	0.30	FSI-PfS-2x

Table 24: Material properties applied in the numerical predictions.

Referring to each numerical prediction several preliminary studies in terms of mesh quality, mesh deformation, coupling conditions, convergence behavior and result quality are performed to achieve the most reasonable results under the requirement of low simulation costs (simulation time and CPU usage). Since the simulation costs of the coupled predictions are high, only the chosen inflow velocity of each test case is applied. Furthermore, in each case the unsteady coupled prediction is started out of an unsteady uncoupled flow solution which again uses a steady flow computation as its initial condition. This approach is common for FSI simulations, since the procedure guarantees that the flow is already fully developed which reduces the settlement phase of the coupled predictions.
For each test case the numerical results of the URANS predictions are compared with the phase-averaged results of the experimental flow and structure data to evaluate the quality of the predictions by the numerical model. Note that due to the URANS approach no phase-averaging is required for the simulation data.

10.2.1. FSI-PfS-1x (Two-dimensional geometry without rear mass)

Based on the nearly two-dimensional behavior of the experimental structural and flow results in all three test cases of FSI-PfS-1x, a two-dimensional numerical grid is chosen to predict the interaction of both physical domains. According to each test case definition the three configurations FSI-PfS-1a, b and c differ mainly in the applied materials (EPDM, polyamide and para-rubber) of the flexible plate attached to the fixed circular cylinder.

[20] As already discussed in the numerical set-up in Section 9, in the applied numerical model no damping is introduced. Therefore, the material damping coefficients are not considered here.

FSI-PfS-1a

The coupled numerical prediction of FSI-PfS-1a (thick EPDM rubber plate attached to the fixed rigid cylinder) reproduces a periodic and symmetric deflection of the structure in the first swiveling mode. Figure 205a shows the time history of the deflections in y-direction from the beginning of the FSI coupling till the simulation reaches a settled periodic motion. The periodic oscillation of the flexible structure is reached after an initial settlement phase of about 2.5 s. In the periodic state the deformations of the structure are characterized by the first swiveling mode and the moderate peak deflections at the monitoring point at $x/D = 3.13$ of about $(y/D)_{\max} = 0.404$ and $(y/D)_{\min} = -0.408$. The slight asymmetry of the maximal and minimal peak deflections are supposed to be an effect of the settlement phase. It is assumed that a longer simulation time would produce a fully symmetrical structural deflection. The oscillation frequency is predicted to $f_{\text{num}} = 6.77$ Hz (St = 0.107). The xy-plot in Fig. 205b shows the motion path of the monitoring point at $x/D = 3.13$[21] close to the far end of the structure. The path describes a symmetric arc which is characteristic for the motion in the first swiveling mode.

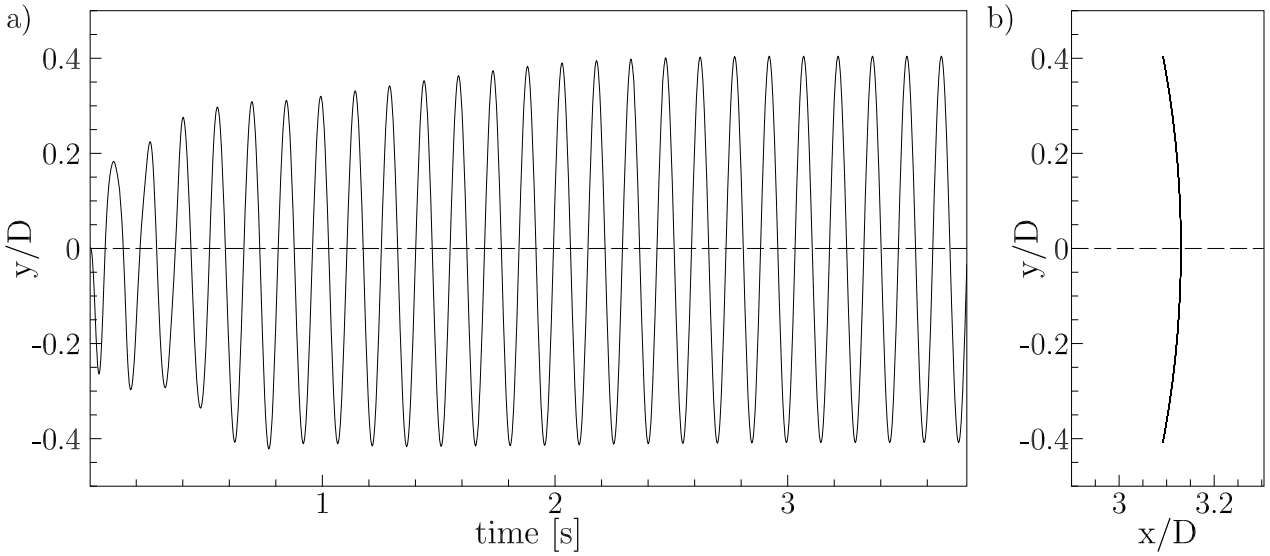

Figure 205: FSI-PfS-1a: Numerical structure results: a) Time history of the y/D displacements; b) xy-displacements, both for the monitoring point at $x/D = 3.13$.

The comparison of the experimental data with the numerical data for the y/D-deflections at the monitoring point ($x/D = 3.13$) is shown in Fig. 206a for the reference period and Fig. 206b depicts the corresponding xy-motion path. The predictions (see Table 25) are in a good agreement regarding the displacements (errors below 6%) and the swiveling frequency which differs about 5%.

Similar to the structural results the predicted flow fields are also in good accordance to the experimental results. Similar to the experimental data in Fig. 113, in Fig. 207 the six complementary flow fields of the numerical prediction within the last predicted period are depicted. All

[21] In the journal paper (De Nayer et al., 2014) and the QNET publication of FSI-PfS-1a a different measurement point at $x/D = 2.82$ is applied.

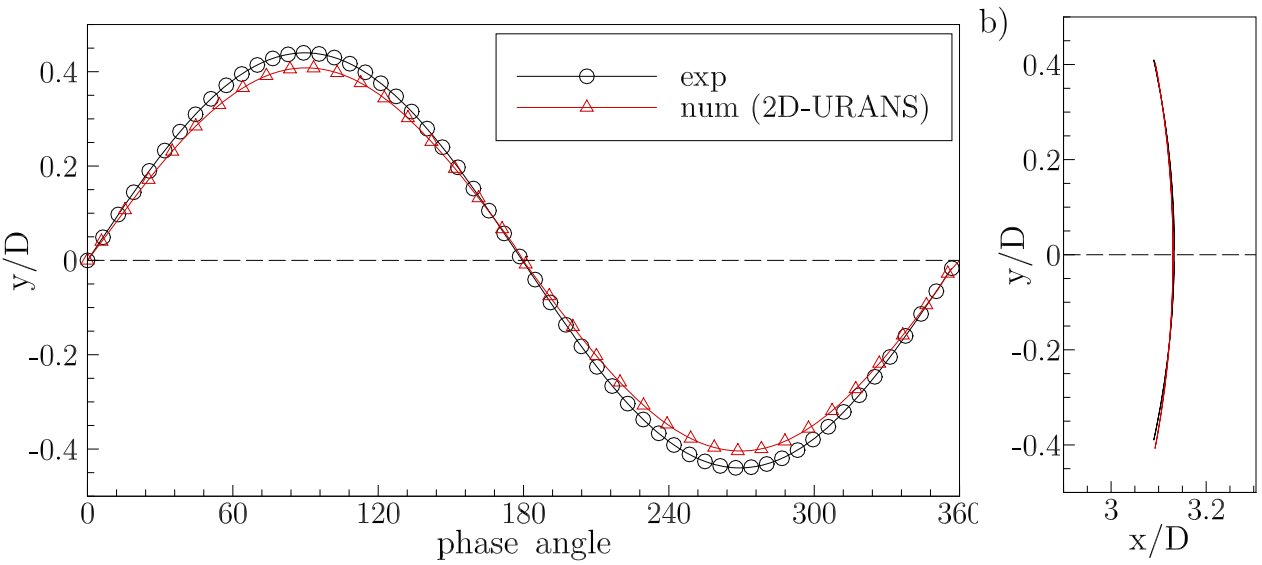

Figure 206: FSI-PfS-1a: Comparison of experimental and numerical structural results: a) Structural deflections y/D; b) Structural xy-motion path, both for the characteristic period at point at $x/D = 3.13$.

flow characteristics are well reproduced. Note that the applied RANS turbulence model only predicts the major flow structures such as the vorticies shedding from the cylinder. Small-scale turbulence effects are not covered by the applied modeling approach. Therefore, cycle-to-cycle variations caused by the turbulent fluctuations are not observed here. Furthermore, an additional phase-averaging method such as applied in the experiments is not necessary since the simulation reaches a periodic state. Due to the higher grid resolution of the computation (in comparison to the coarse PIV grid) several flow features, e.g., the stagnation point in front of the structure, the boundary layers on the cylinder surface and the wake near the flexible plate are more clearly visible than in the measured data.

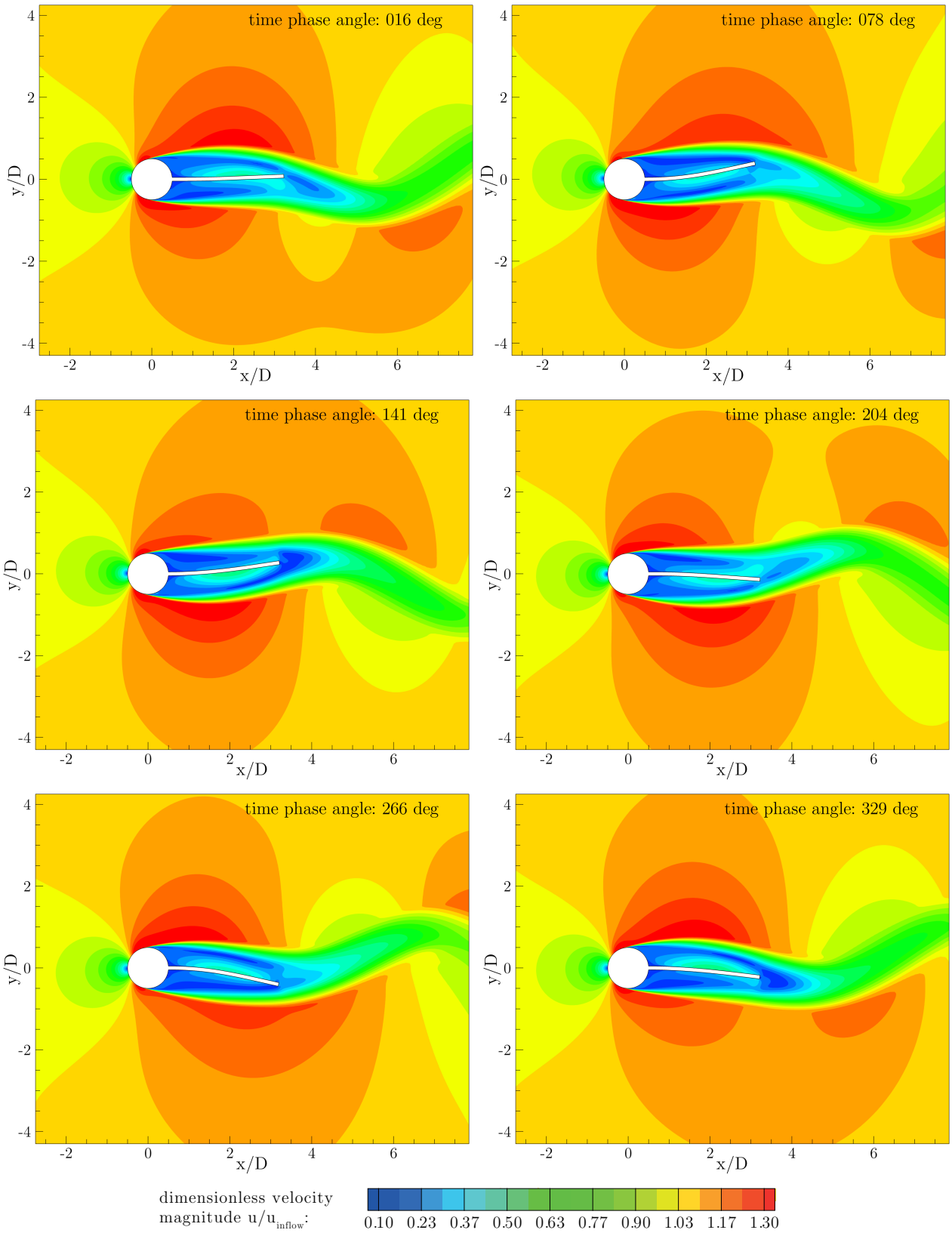

Figure 207: FSI-PfS-1*a*: Predicted flow and structural results for the characteristic period.

In Fig. 208 the predicted lift and drag coefficients (of the entire structure, e.g., the cylinder and the rubber plate) are shown as a function of the simulation time. As already mentioned in the introduction of this section, the FSI predictions are started out of an uncoupled flow prediction in order to release the flexible structure in an almost developed fluid flow. Similar to the preliminary experimental studies on the fixed configuration of each test case, now the uncoupled flow solution can be compared with the coupled FSI prediction. In the uncoupled CFD simulation the average drag coefficient on the entire structure is calculated to $\overline{c_D} = 0.70$ ($f_{c_D} = 22.73$ Hz, $\Delta c_D = \pm 0.01$). In contrast to the almost constant drag coefficient, the lift coefficients of the front cylinder and the flexible structure show large oscillations. Due to the already existing periodic vortex shedding from the cylinder, the lift oscillates around zero with a value of $c_{L,\text{cylinder}} = \pm 0.17$ and a frequency of $f_{c_L} = 11.36$ Hz which yield the half of f_{c_D}. The lift coefficient $c_{L,\text{rigid structure}}$ on the entire interface follows $c_{L,\text{cylinder}}$ with a phase shift of +319 deg, which is a result of the convection of the vortical structures. For the uncoupled case a constant periodic oscillation ($c_{L,CFD} = \pm 0.78$) and the same frequency f_{c_L} are found.
The coupled simulation with the flexible rubber plate starts at the simulation time $t = 0$ s. After an initial phase the system again attains a periodic oscillation state. While the mean drag coefficient remains almost constant, a large change in the acting lift forces appears. Both lift coefficients ($c_{L,\text{cylinder}} = \pm 0.42$, $c_{L,\text{flexible structure}} = \pm 0.24$ are now in-phase to each other and have a phase shift of 219 deg[22] to the y/D-displacements of the point $x/D = 3.13$ at the end of the rubber plate. Remarkable is the strong decrease of the lift forces on the FSI interface due to the elasticity of the structure, while the force on the cylinder only slightly increases. Furthermore, the lock-in frequency of the system is reduced to $f_{c_L} = 6.77$ Hz (decrease of about 40% in comparison to the uncoupled vortex shedding frequency).

[22]The alternate phase shift of 141 deg would also be reasonable. In the present case and the following cases the most reasonable physical interpretation is used. Since the lift forces at the cylinder are physically present at first (in comparison to the lift and deflection of the flexible plate) it will be referenced.

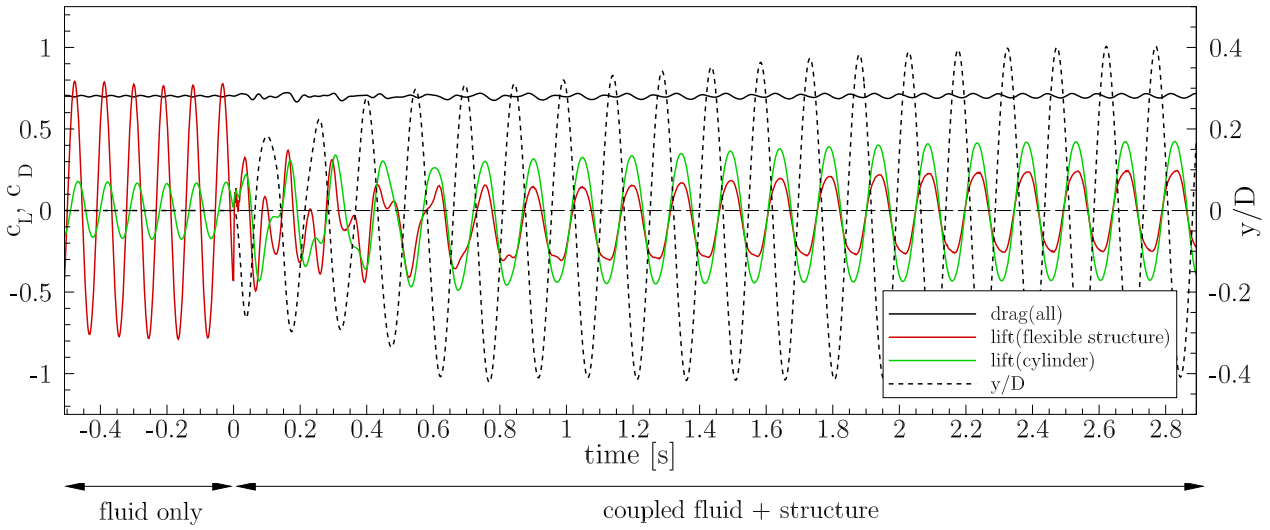

Figure 208: FSI-PfS-1a: Numerical results: Time histories of the drag coefficient c_D on the entire structure, the lift coefficients c_L of the front cylinder and the flexible structure and the y/D-deflections at $x/D = 3.13$ for the uncoupled and coupled solution.

FSI-PfS-1b

Since the configuration of FSI-PfS-1*b* only differs in the applied material (polyamide instead of EPDM rubber) and the thickness of the plate (0.8 mm instead of 2.1 mm), the predicted results are close to the findings of FSI-PfS-1*a*. Again the computation results in a periodic and symmetric deformation of the structure in the first swiveling mode due to the excitation by the surrounding flow. Remarkable is the shorter settlement phase of 1.5 s in comparison to FSI-PfS-1*a*. The deflections at the end of the polymer plate ($x/D = 3.13$) yield maximal and minimal y-deflections of about $(y/D)_{\max} = 0.412$ and $(y/D)_{\min} = -0.416$ and an oscillation frequency of $f_{\text{num}} = 7.39$ Hz (St = 0.117). Again, the slight asymmetry of the maximal and minimal peak deflections are supposed to be an effect of the settlement phase. Similar to FSI-PfS-1*a* it is assumed that a longer simulation time would produce a fully symmetrical structural deflection. Figure 209a shows the time history of the deflections in the y-direction from the beginning of the coupling till the simulation reaches a constant periodic motion. The xy-phase plane in Fig. 209b shows the characteristic arc-shaped trajectory which is typical for the first swiveling mode of the structure.

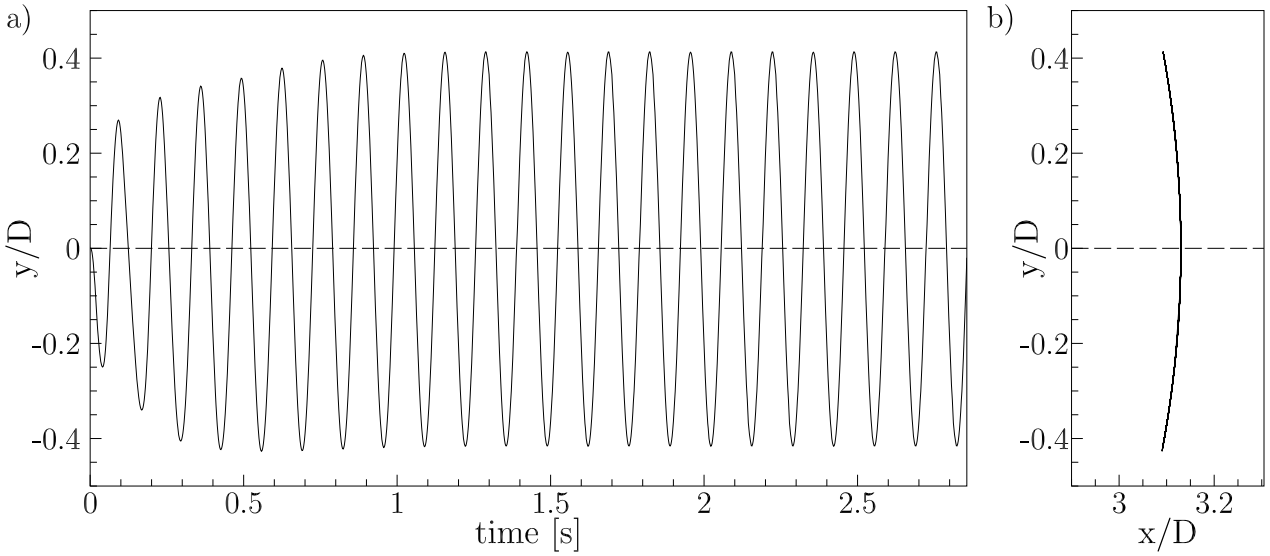

Figure 209: FSI-PfS-1*b*: Numerical structure results: a) Time history of the y/D displacements b) xy-displacements, both for the monitoring point at $x/D = 3.13$.

The comparison of the experimental data and the numerical data for the structural deflections is depicted in Fig. 210 for the characteristic period. With an error below 9% for the y-displacements and an error below 8% for the frequency, the predictions show a reasonable agreement with the experimental data (see Table 25).

In Fig. 211 the predicted flow fields for the six time phase angles 16, 78, 141, 204, 266 and 326 deg are presented. Again the predictions are in a good accordance with the experimental results (Fig. 124). The higher swiveling frequency of the flexible structure in the experiments causes a slightly different flow distribution in comparison to the flow fields found in the numerical solution. Once again the numerical prediction provides more and sharper distributed flow details due to the higher grid resolution and the absence of cycle-to-cycle variations.

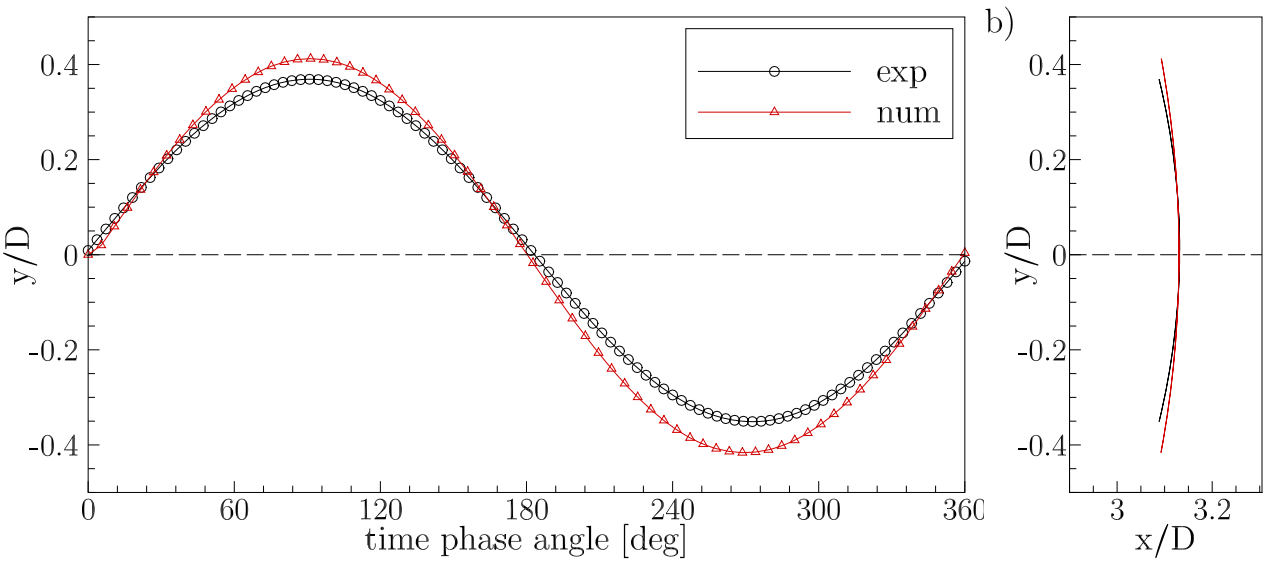

Figure 210: FSI-PfS-1*b*: Comparison of experimental and numerical structural results: a) Structural deflections y/D; b) Structural xy-motion path, both for the characteristic period at point at $x/D = 3.13$.

The predictions of the force coefficients are presented in Fig. 212. Similar to the uncoupled solution of FSI-PfS-1a the average drag coefficient on the entire rigid structure is calculated to $\overline{c_D} = 0.72$ with a frequency of $f_{c_D} = 22.73$ Hz and an amplitude of $\Delta c_D = \pm 0.01$. The lift coefficient on the front cylinder oscillates around zero with a value of $c_{L,\text{cylinder}} = \pm 0.19$ and a frequency of $f_{c_L} = 11.36$ Hz. Again the lift coefficient $c_{L,\text{rigid structure}}$ on the entire interface follows $c_{L,\text{cylinder}}$ with a phase shift of +319 deg. A constant periodic oscillation ($c_{L,CFD} = \pm 0.85$) and the same frequency f_{c_L} are found. For FSI-PfS-1b the coupled simulation starts at the time $t = 0$ s. After an initial phase the system reaches again a periodic oscillation state. The mean drag coefficient remains constant but oscillates now with a larger amplitude $\Delta c_D = \pm 0.03$ around $\overline{c_D} = 0.71$ with a reduced frequency of $f_{c_D} = 15.15$ Hz. Due to the FSI coupling both lift coefficients are altered leading to values of $c_{L,\text{cylinder}} = \pm 0.45$ and $c_{L,\text{flexible structure}} = \pm 0.24$ and a lock-in oscillation frequency of about $f_{c_L} = 7.58$ Hz for the deflections. Furthermore, between the lift forces there is a phase shift of about 300 deg. That means the lift on the FSI interface follows the lift on the cylinder. In relation to the lift on the cylinder the y/D displacements at the end of the rubber plate is following with a phase shift of 240 deg. This is a remarkable result since the swiveling mode and the deflection levels are quite similar to the results of FSI-PfS-1a, but a significantly different force history is predicted. It can be assumed that the stiff polyamide material is responsible for this behavior retarding its deformation. Thus, a different phase delay is present in FSI-PfS-1b compared to FSI-PfS-1a.

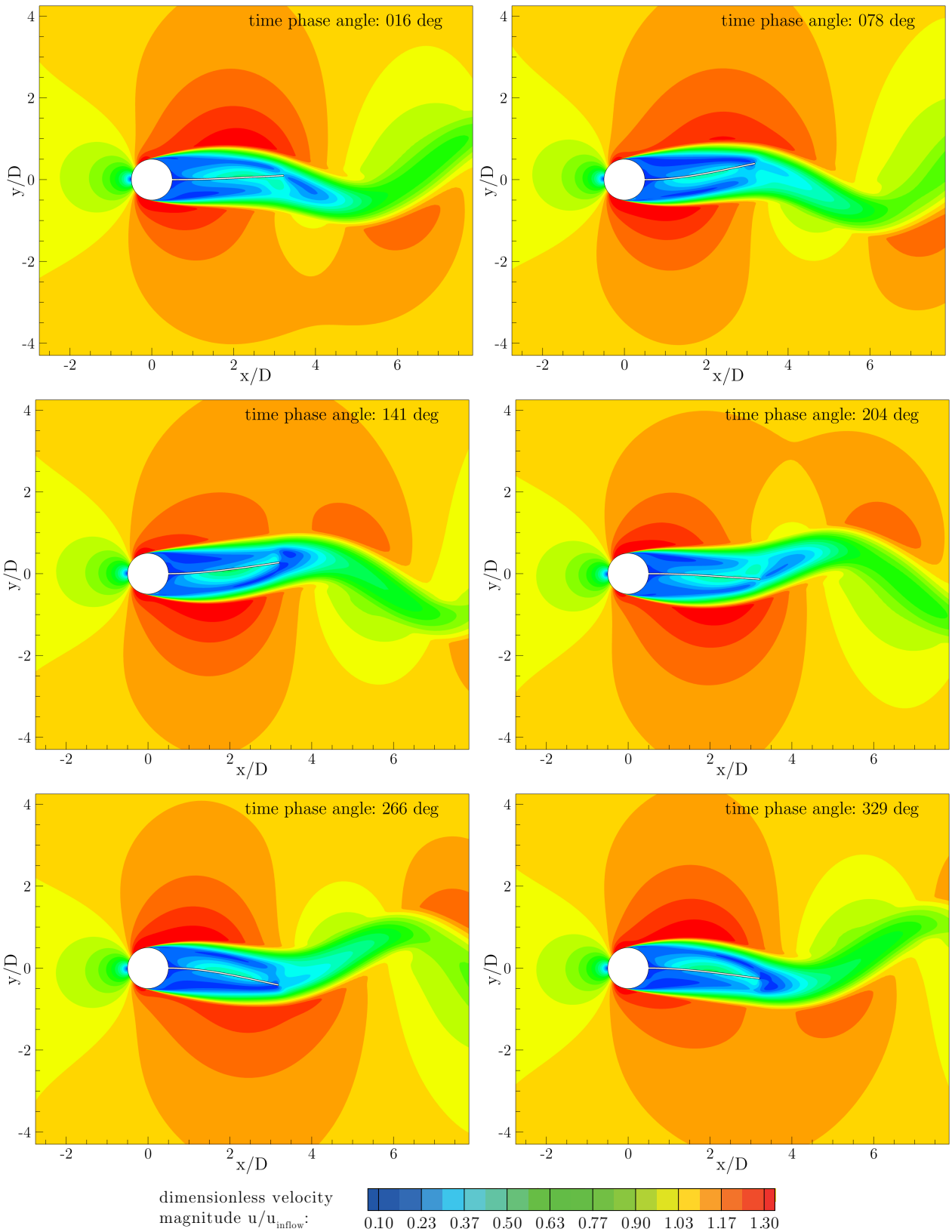

Figure 211: FSI-PfS-1*b*: Predicted flow and structural results for the characteristic period.

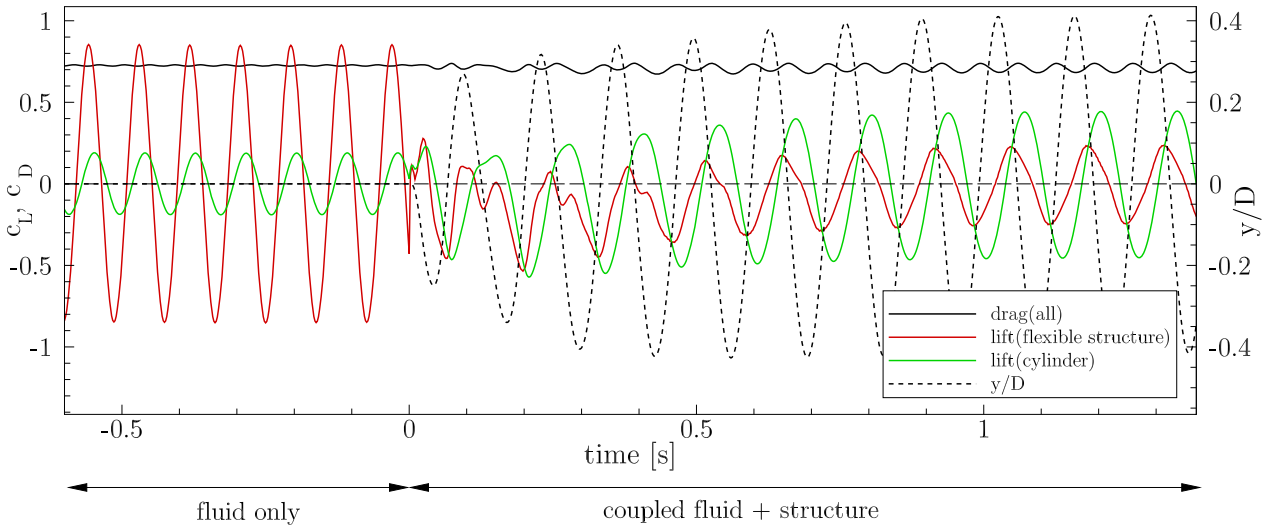

Figure 212: FSI-PfS-1*b*: Numerical results: Time histories of the drag coefficient c_D on the entire structure, the lift coefficients c_L of the front cylinder and the flexible structure and the y/D-deflections at $x/D = 3.13$ for the uncoupled and coupled solution.

FSI-PfS-1c

In contrast to FSI-PfS-1a and b the computation of FSI-PfS-1c (thick flexible para-rubber plate attached to a fixed rigid cylinder) delivers a periodic and symmetric deflection of the structure in the second swiveling mode. After a very short initial settlement phase of only 0.5 s the structure reaches a periodic oscillation in this more complex swiveling motion (Fig. 213a). The mean peak y-deflections reach values of $(y/D)_{\max} = 0.422$ and $(y/D)_{\min} = -0.423$. The oscillation frequency is predicted to $f_{\text{num}} = 11.90$ Hz (St = 0.222). The xy-trajectory of the monitoring point at $x/D = 3.13$ is given in Fig. 213b. The path describes a symmetric "8" which is characteristic for the motion in the second oscillation mode.

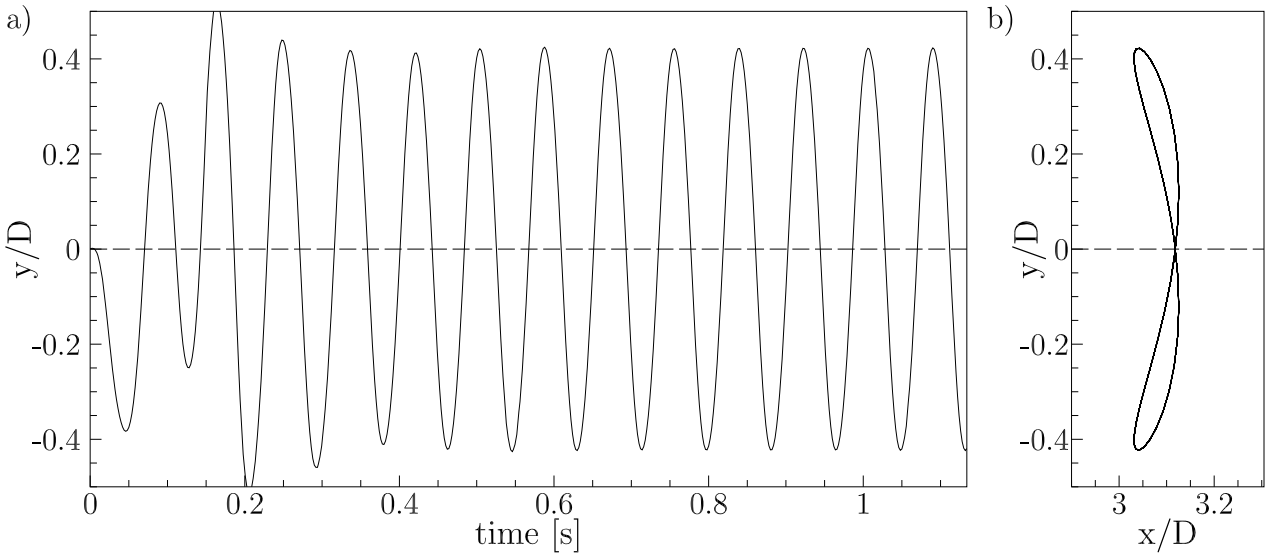

Figure 213: FSI-PfS-1c: Numerical structure results: a) Time history of the y/D displacements b) xy-displacements, both for the monitoring point at $x/D = 3.13$.

Since an almost equal trajectory is also obtained in the experiments, the experimental data and the numerical data almost coincide. The corresponding comparisons of the structural deflections are presented in Fig. 214 for the characteristic period. The errors of the prediction are below 6% for the y-deflections and the frequency differs by about 5%.
The predicted flow fields in Fig. 215 are in a good accordance with the experimental results (Fig. 133). Due to the almost doubled oscillation frequency in comparison to FSI-PfS-1a and 1b, three successive counter-rotating vortex centers are visible in the wake of the structure.

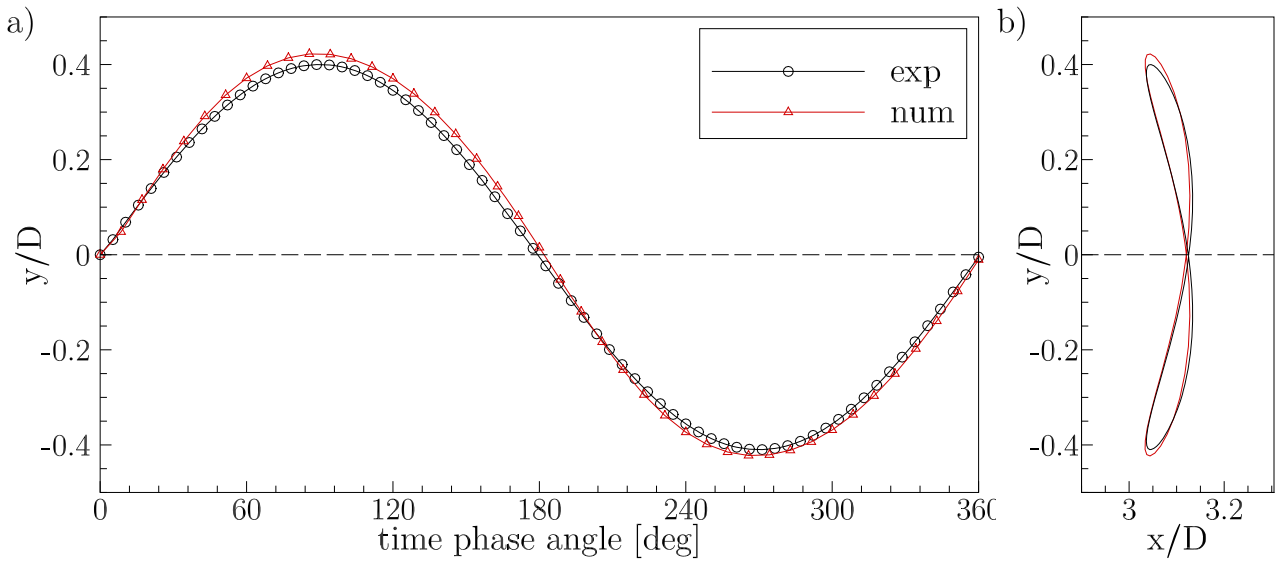

Figure 214: FSI-PfS-1*c*: Comparison of experimental and numerical structural results: a) Structural deflections y/D; b) Structural xy-motion path, both for the characteristic period at point at $x/D = 3.13$.

In Fig. 216 the predicted fluid forces on the structure are plotted as a function of the simulation time. In the uncoupled CFD simulation the average drag coefficient on the entire structure is calculated to $\overline{c_D} = 0.75$ ($f_{c_D} = 19.23$ Hz, $\Delta c_D = 0.01$). In contrast to the almost constant drag coefficient, the lift coefficients on the front cylinder and the FSI interface show large oscillations. Due to the existing periodic vortex shedding from the cylinder, the lift oscillates around zero with a value of $c_{L,\text{cylinder}} = \pm 0.21$ and a frequency of $f_{c_L} = 9.62$ Hz. With a phase shift of 319 deg the lift coefficient $c_{L,\text{rigid structure}}$ on the entire interface follows $c_{L,\text{cylinder}}$ with a constant periodic oscillation ($c_{L,CFD} = \pm 0.92$ and the same frequency f_{c_L}. The coupled simulation with the soft para-rubber plate starts at the time of $t = 0$ s. As already mentioned the settlement phase of the system to reattain a periodic oscillation state is very short. The mean drag coefficient is slightly increased to $\overline{c_D} = 0.77$ and oscillates about $\Delta c_D = \pm 0.04$ with a frequency of $f_{c_D} = 23.81$ Hz. The lift coefficients of the front cylinder $c_{L,\text{cylinder}} = \pm 0.19$ and the rubber plate $c_{L,\text{flexible structure}} = \pm 0.37$ are phase-shifted by about 120 deg to each other. The lift coefficient of the front cylinder $c_{L,\text{cylinder}}$ is followed by the y/D-displacements at the end of the rubber plate with a phase shift of 43 deg and the lift coefficient of the flexible plate $c_{L,\text{flexible structure}}$ by 197 deg, respectively. Furthermore, the lock-in frequency of the system is now increased to $f_{c_L} = 11.91$ Hz.

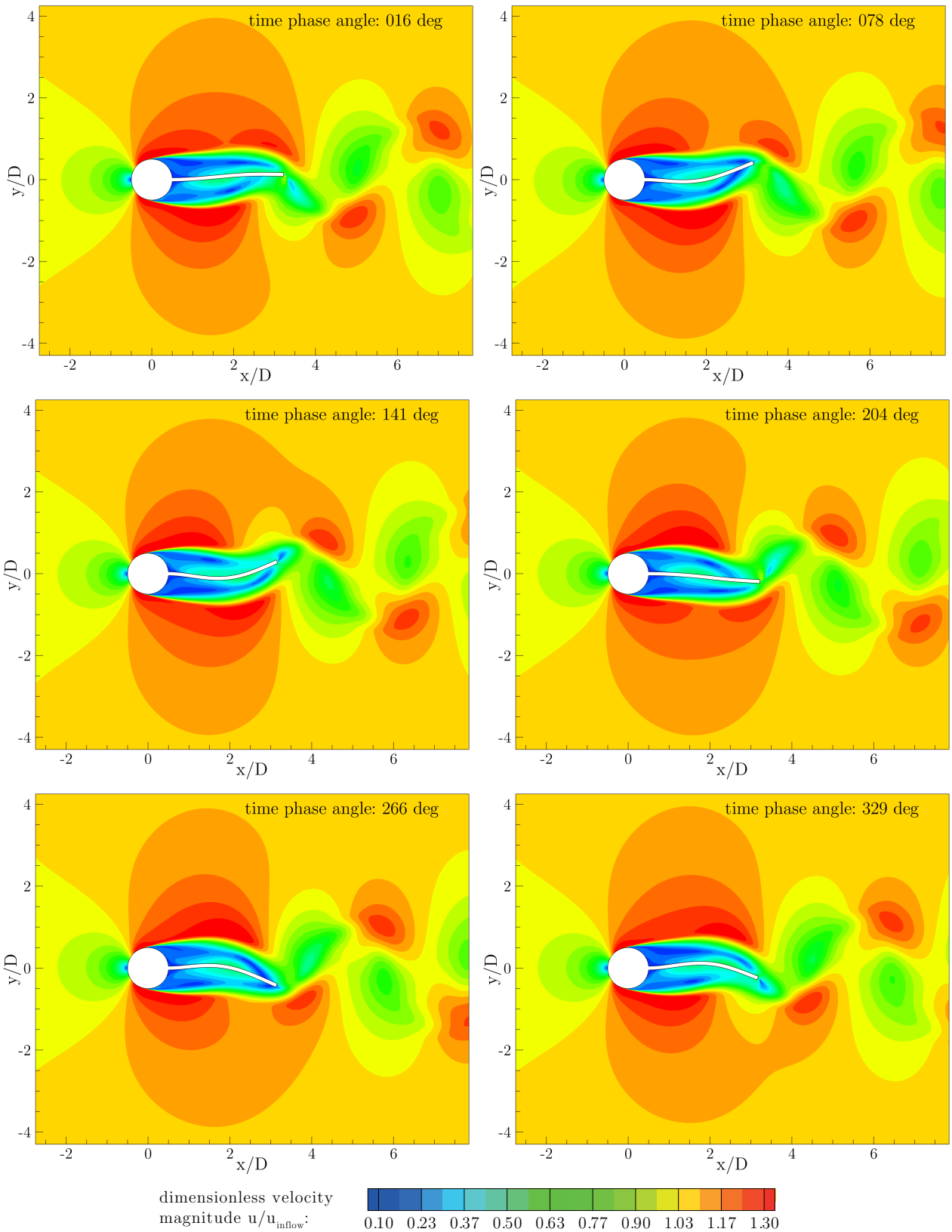

Figure 215: FSI-PfS-1*c*: Predicted flow and structural results for the characteristic period.

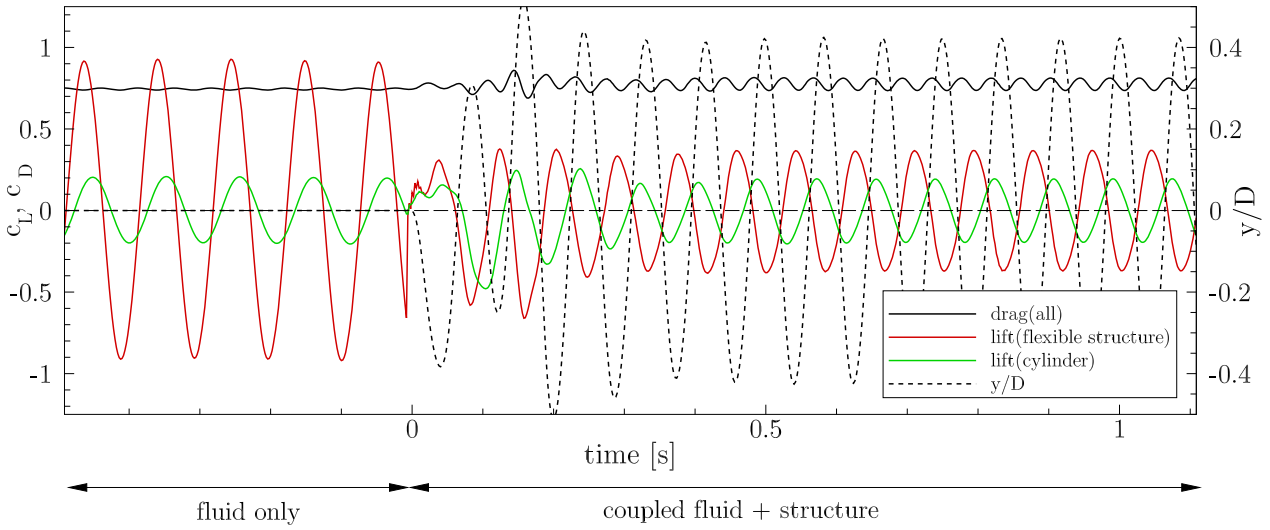

Figure 216: FSI-PfS-1*c*: Numerical results: Time histories of the drag coefficient c_D on the entire structure, the lift coefficients c_L of the front cylinder and the flexible structure and the y/D-deflections at $x/D = 3.13$ for the uncoupled and coupled solution.

FSI-PfS-1x - Conclusions

The first set of FSI test cases (FSI-PfS-1x) focuses on simple two-dimensional geometries and moderate structural deflections depending on the plate material. Based on the experimental set-up and the structural testings for the material properties, the computations of the three configurations with ANSYS®-CFX 14.0 yield satisfactory results. The general findings derived from the experiments (see Section 10.1.1) on the system coupling depending on the chosen flexible material are confirmed by the computations. In comparison to the experiments the predictions produces errors between 3% and 8% for the y-displacements and errors between 5% and 8% for the swiveling frequency. A summary of the comparisons is listed in Table 25.

test case	**FSI-PfS-1a**	**FSI-PfS-1b**	**FSI-PfS-1c**
simulation	successful	successful	successful
swiveling mode	1st mode	1st mode	2nd mode
bending shape	flat ')'	flat ')'	flat '8'
u_{inflow} [m/s]	1.385 m/s	1.385 m/s	1.179 m/s
symmetry	$\approx$	$\approx$	✓
f_{num} [Hz]	6.77	7.39	11.90
f_{exp} [Hz]	7.11	8.02	11.39
error(f)	-4.78%	-7.86%	$+4.48\%$
St_{num}	0.107	0.117	0.222
St_{exp}	0.113	0.127	0.213
$(y/D)_{\text{num,max}}$	0.404	0.412	0.422
$(y/D)_{\text{exp,max}}$	0.439	0.380	0.398
$(y/D)_{\text{num,min}}$	-0.408	-0.416	-0.423
$(y/D)_{\text{exp,min}}$	-0.440	-0.393	-0.410
error($(y/D)_{\text{max}}$)	-7.97%	$+8.42\%$	$+6.03\%$
error($(y/D)_{\text{min}}$)	-7.27%	$+5.85\%$	$+2.93\%$
validation	successful	successful	successful

Table 25: Comparison of the numerical data with the experimental results of FSI-PfS-1x.

The comparison of the predicted lift and drag forces on the structures between the three test cases reveal the dependency of the acting forces on the swiveling mode of the system. While FSI-PfS-1a and 1b oscillate in the first mode and the lift on the cylinder is larger than the lift on the FSI interface, FSI-PfS-1c swivels in the second mode and the lift on the cylinder is smaller than the lift on the FSI interface. The influence of the swiveling mode is also observable in the modulation of the system frequencies between the pure fluid and the coupled simulation. The system frequencies in FSI-PfS-1a and 1b decrease in the coupled FSI predictions while the frequency in FSI-PfS-1c increases. For the drag forces no significant change due to the elasticity of the structure is noticed. Despite the slightly asymmetric structural deflections (probably a settlement phase effect) the predictions of all three cases are successful and are confirmed by the experimental data.
In the journal paper (De Nayer et al., 2014) and the QNET publication an additional detailed comparison to coupled LES predictions of FSI-PfS-1a is carried out.

10.2.2. FSI-PfS-2x (Two-dimensional geometry with rear mass)

According to the attachment of the rigid steel weight at the end of the flexible para-rubber plate and based on the experimental results of FSI-PfS-2x, the usage of a two-dimensional mesh for the numerical predictions is justified. With respect to the experimental studies large structural deflections are expected for both test configurations FSI-PfS-2a and 2b. Especially the free rotational degree of freedom of the front cylinder in FSI-PfS-2b enlarges the structural deflections in such a manner that special concerns on the mesh deformation and their distribution are necessary. In the following paragraphs the computational results of both test cases FSI-PfS-2x and the comparisons with the experimental data are described.

FSI-PfS-2a

Similar to the experimental results the coupled numerical prediction shows a periodic deflection of the structure in the second swiveling mode. The monitoring point near the tail at $x/D = 3.13$ reaches deflections of $(y/D)_{\max} = 0.637$ and $(y/D)_{\min} = -0.639$ in the second swiveling mode which are very close to the experimentally observed values. The predicted oscillation frequency of 11.91 Hz is slightly higher than the experimental value of 11.25 Hz. Figure 217a shows the time histories of the structural deflections in x- and y-direction from the start of the coupling till the simulation reaches a constant periodic motion. The xy-plot in Fig. 217b depicts the motion path of the monitored point at $x/D = 3.13$ close to the end of the steel weight. The path is nearly symmetric due to the symmetric motion of the predicted structure deformation. The slight asymmetry of the structural deflections is probably again a settlement effect. It can be assumed that a longer simulation time will produce fully symmetrical deflections. The comparison between the experimental data and the numerical data is shown in Fig. 218. The predictions of the structural displacements are quite similar to the experimental results.

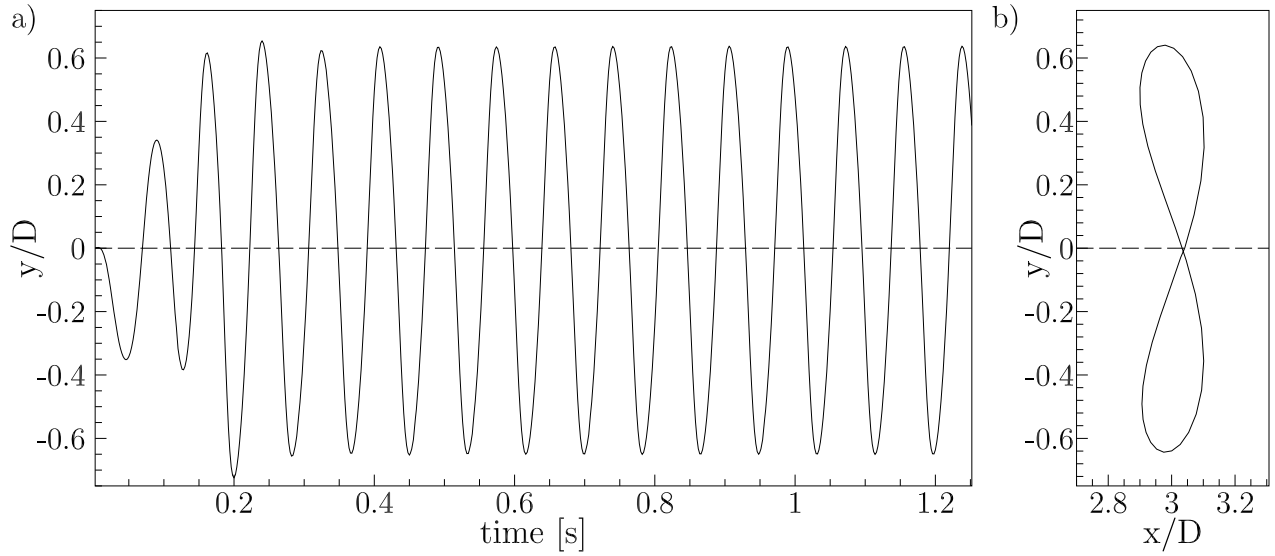

Figure 217: FSI-PfS-2a: Numerical structure results: a) Time history of the y/D displacements b) xy-displacements, both for the monitoring point at $x/D = 3.13$.

The predicted flow fields including the deformed structure for the same six states within a period as depicted for the experimental results in Fig. 143 are shown in Fig. 219. In contrast

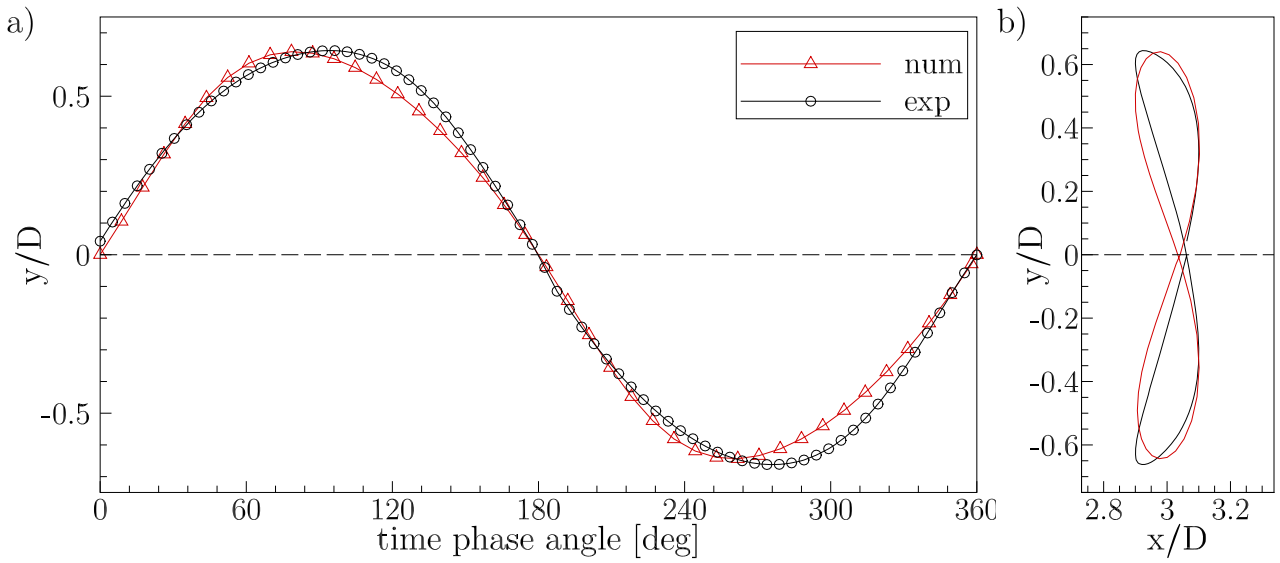

Figure 218: FSI-PfS-2*a*: Comparison of experimental and numerical structural results: a) Structural deflections y/D; b) Structural xy-motion path, both for the characteristic period at point at $x/D = 3.13$.

to the experimental data these results are not phase-averaged as explained above. Due to the statistical RANS turbulence model only the dominating vorticies shedding from the cylinder are predicted. The overall flow structure for all six phase angles depicted in Fig. 219 is in close agreement with the corresponding plots in Fig. 143 showing the measured data. The shed vorticies are convected downstream leading to an alternating vortex pattern in the wake of the structure. Finally, these vorticies leave the region of interest. In contrast to the PIV results the stagnation point in front of the cylinder is clearly visible. Due to the higher resolution of the computation compared to the PIV resolution more details are generally recognizable. At the end of the structure the formation of a second smaller vortex is identified which merges shortly after the detachment of the tail with the large eddy convecting downstream. This secondary vortex is also observed in the test cases of Gomes and Lienhart (2013) and appears especially in the second swiveling mode. As already mentioned this oscillation state is characterized by large deformations and high swiveling frequencies. Both lead to significant and fast structural motions through the fluid which allows the vortex formation at the tip of the structure.

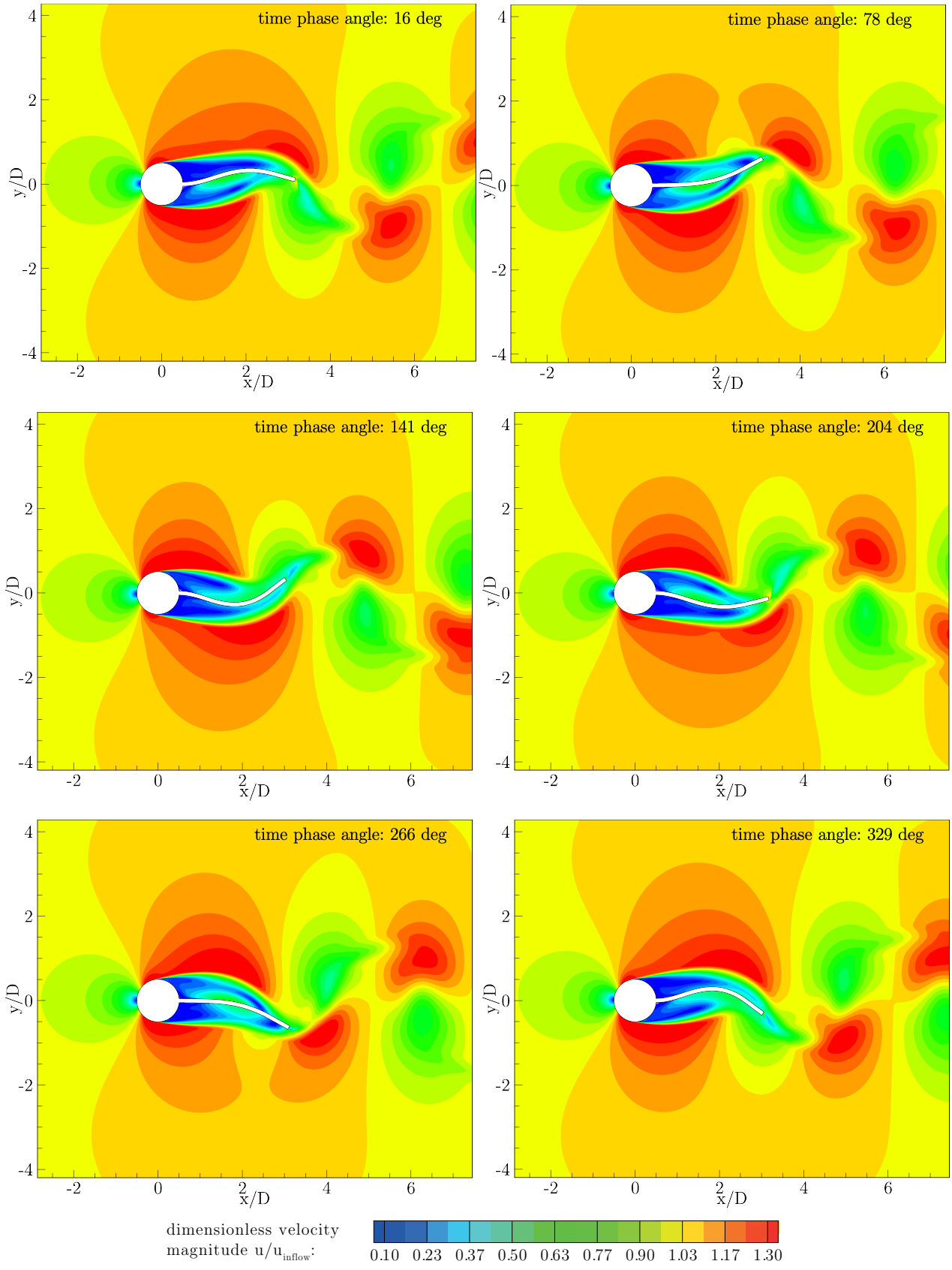

Figure 219: FSI-PfS-2*a*: Predicted flow and structural results for the characteristic period.

In Fig. 220 the predicted fluid forces on the structure are plotted as a function of the simulation time. Since the initialization of this numerical solution of FSI-PfS-2a is the same as in FSI-PfS-1a the same fluid forces and corresponding frequencies ($\overline{c_D} = 0.70$, $f_{c_D} = 22.73$ Hz, $\Delta c_D = \pm 0.01$, $c_{L,\text{Cylinder}} = \pm 0.17$, $c_{L,CFD} = \pm 0.78$, $f_{c_L} = 11.36$ Hz, phase delay between $c_{L,\text{cylinder}}$ and $c_{\text{L,rigid structure}}$ equals 319 deg) appear. The coupled simulation with the flexible para-rubber plate starts at the time $t = 0$ s. After an initial phase the system again reaches the periodic second swiveling mode. The drag coefficient starts to oscillate around its increased mean value of $\overline{c_D} = 0.88$ with $\Delta c_D = \pm 0.18$ and a frequency of $f_{c_D} = 22.81$ Hz. The lift coefficients on the cylinder and the FSI interface act acyclic to each other and possesses almost equal values with $c_{L,\text{Cylinder}} = \pm 0.59$ and $c_{L,\text{flexible structure}} = \pm 0.56$. With a phase shift of about 9 deg with respect to the lift force on the cylinder the y/D displacements at the end of the rubber plate are nearly in phase. Consequently, the lift on the FSI interface acts almost acyclic to this deflection (phase shift: 189 deg). Similar to FSI-PfS-1c the lock-in frequency of the system is slightly increased to $f_{c_L} = 11.91$ Hz.

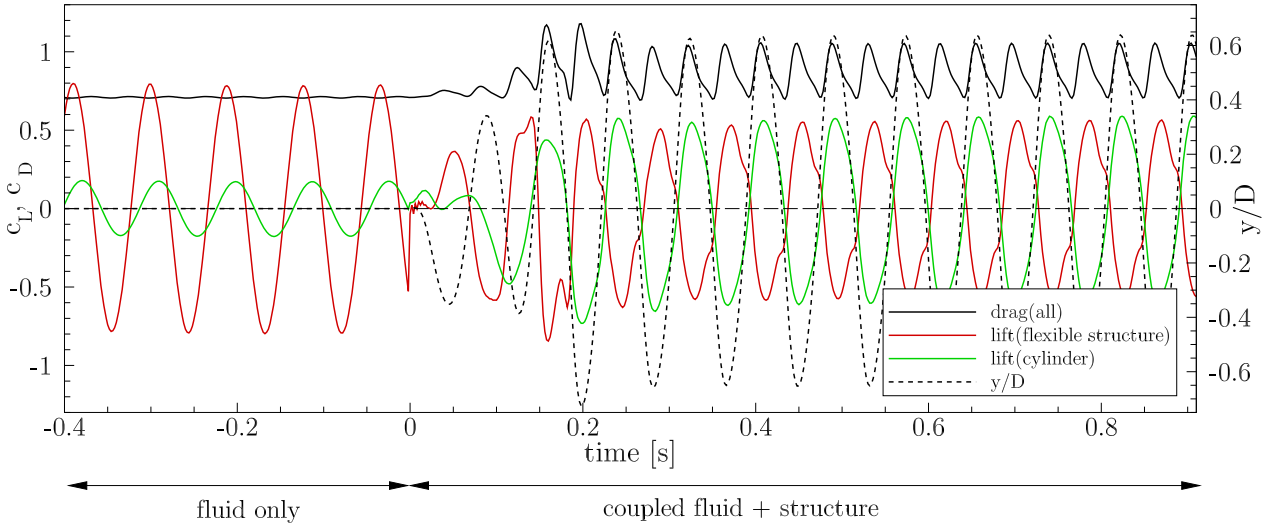

Figure 220: FSI-PfS-2a: Numerical results: Time histories of the drag coefficient c_D on the entire structure, the lift coefficients c_L of the front cylinder and the flexible structure and the y/D-deflections at $x/D = 3.13$ for the uncoupled and coupled solution.

FSI-PfS-2b

The computation of FSI-PfS-2b (released rotational degree of freedom) predicts a periodic and symmetric deflection of the structure in the second swiveling mode with exceedingly large deflections depicted in Fig. 221. After an initial settlement phase of only 1 s the structure reaches a periodic oscillation in a very complex oscillation mode. Due to the released rotational DOF of the front cylinder, the deflections at $x/D = 3.13$ reach values of $(y/D)_{\max} = 0.983$ and $(y/D)_{\min} = -0.992$ in the range of the cylinder diameter. The oscillation frequency is predicted to $f_{\text{num}} = 8.62$ Hz (St $= 0.137$). Fig. 221a shows the time history of the deflections in y-direction from the beginning of the coupling till the simulation reaches a constant periodic motion. The xy-plot in Fig. 221b displays the characteristic phase plane of the monitored point

at $x/D = 3.13$ close to the far end of the structure.

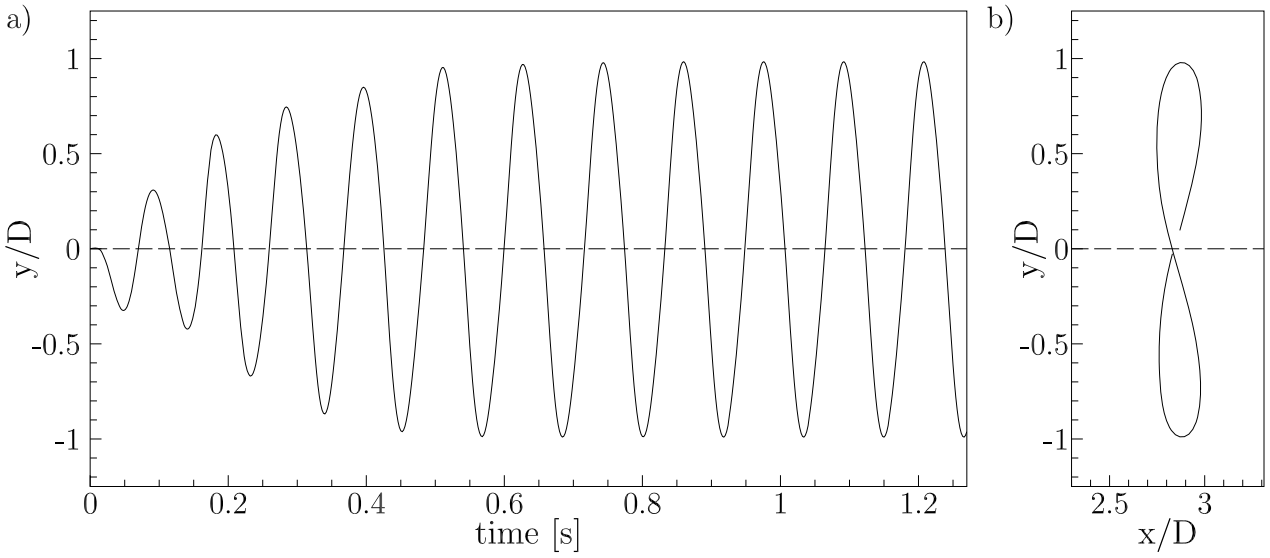

Figure 221: FSI-PfS-2*b*: Numerical structure results: a) Time histories of the y/D displacements b) xy-displacements, both for the monitoring point at $x/D = 3.13$.

The front angle motion is represented by a maximal deflection of $\phi_{\max} = 24.83$ deg and a minimal deflection of $\phi_{\min} = -24.13$ deg within the characteristic period. In Fig. 222 a constant phase difference of about 80 deg between the angular motion of the front cylinder and the deflection of the trailing edge is observed similar to the experimental results. The numerical prediction of the front-body angle almost follows the experimental data but reveals differences in the structural deflections. The comparison between the experimental and the numerical data for the structural deflections at $x/D = 3.13$ presents large aberrations of about 11%. One possible reason for this large error is the friction present in the ball bearings of the front cylinder which is neglected in the numerical model. Despite these large deviations the predicted frequency only differs by about 5%.

The predicted flow fields at the six time phase angles (16, 78, 141, 204, 266 and 326 deg) in Fig. 223 are quite similar to the phase-averaged PIV results shown in Fig. 154. In all six states the relevant flow features (e.g., the acceleration areas, the shed vorticies in the wake and the angular displacement of the stagnation point in front of the structure) and the deflected structure agree quite well with the position, the appearance and the size of the experimentally determined data. Due to the better spatial resolution of the numerical prediction compared to the PIV data, smaller details in the flow field are observable. Especially in the regions of high velocity gradients now more precise flow information are available. For instance the small secondary trailing-edge vortex (generated while the structures moves through the wake area) is hardly visible in the experimental results, but is now clearly accessible in the numerical data.

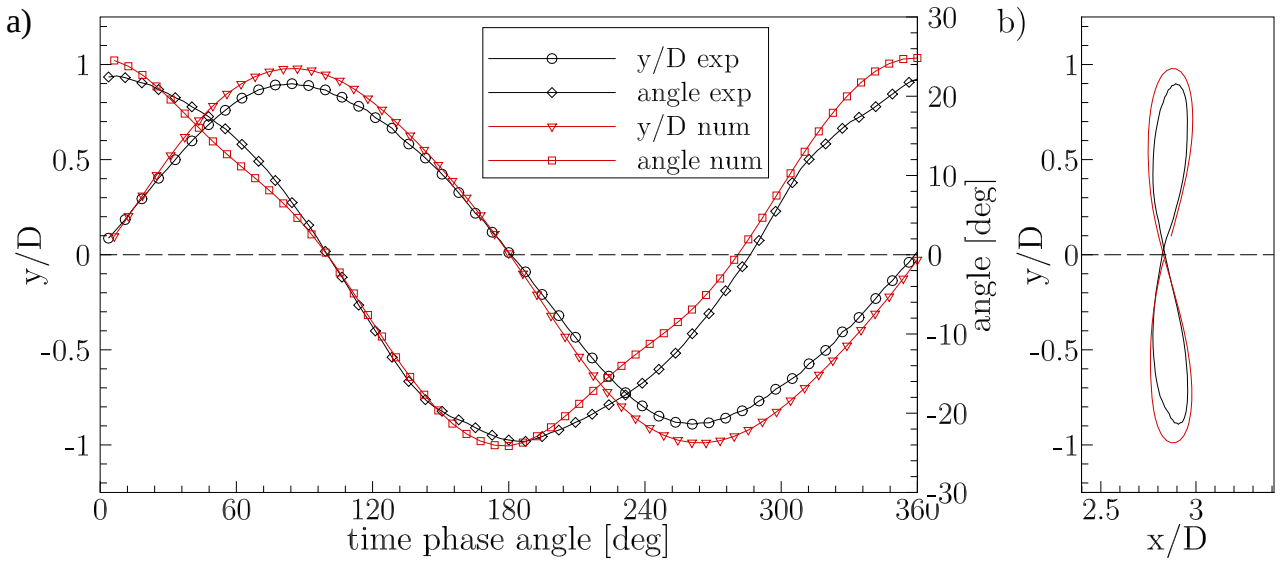

Figure 222: FSI-PfS-2*b*: Comparison of experimental and numerical structural results: a) Structural deflections y/D and front body angle; b) Structural xy-motion path, both for the characteristic period at point at $x/D = 3.13$.

The time histories of the predicted fluid forces on the structure are depicted in Fig. 224. Again the flow initialization of the numerical FSI solution of FSI-PfS-2*b* is the same as in FSI-PfS-1*a* and 2*a*. Thus equal fluid forces ($\overline{c_D} = 0.70$, $f_{c_D} = 22.73$ Hz, $\Delta c_D = \pm 0.01$, $c_{L,\text{Cylinder}} = \pm 0.17$, $c_{L,CFD} = \pm 0.78$, $f_{c_L} = 11.36$ Hz, phase delay between $c_{L,\text{cylinder}}$ and $c_{\text{L,rigid structure}}$ equals 319 deg) are present. The coupled simulation with the rotatable bearing of the front cylinder and the flexible para-rubber plate starts at the time $t = 0$ s. After an initial phase the system reaches the periodic second swiveling mode with large structural deflections. Similar to FSI-PfS-2*a* the drag coefficient starts to oscillate, but in the present case it increases strongly to a mean value of $\overline{c_D} = 1.20$ with $\Delta c_D = \pm 0.17$ and a frequency of $f_{c_D} = 17.24$ Hz. The lift coefficients on the cylinder and the FSI interface act with a phase shift of 96 deg to each other with $c_{L,\text{Cylinder}} = \pm 1.92$ and $c_{L,\text{flexible structure}} = \pm 0.76$. The y/D-displacements at the end of the rubber plate follows the lift on the cylinder with a phase shift of 292 deg. Consequently, the lift on the FSI interface follows the deflection with a phase delay of 174 deg. The lock-in frequency of the system decreases to $f_{c_L} = 8.62$ Hz in comparison to the uncoupled flow simulation. In comparison to the numerical results of FSI-PfS-2*a* an increase of the mean drag coefficient from $\overline{c_{D,2a}} = 0.88$ to $\overline{c_{D,2b}} = 1.20$ in FSI-PfS-2*b* shows the additional blockage of the channel due to the rotational DOF of the front cylinder. Connected to this effect is the strong increase of the lift coefficient at the front cylinder from $c_{L,\text{Cylinder,2a}} = \pm 0.59$ in FSI-PfS-2*a* to $c_{L,\text{Cylinder,2b}} = \pm 1.92$ in FSI-PfS-2*b*, while the lift coefficient at the FSI interface is only slightly increased ($c_{L,\text{FSI,2a}} = \pm 0.56$ to $c_{L,\text{FSI,2b}} = \pm 0.76$).

FSI-PfS-2x - Conclusions

The second set of FSI test cases (FSI-PfS-2x) focuses on simple two-dimensional geometries and large structural deflections. The case FSI-PfS-2*b* differs form the previous cases concerning the release of the rotational DOF of the front cylinder. Similar to the satisfactory comparison of the

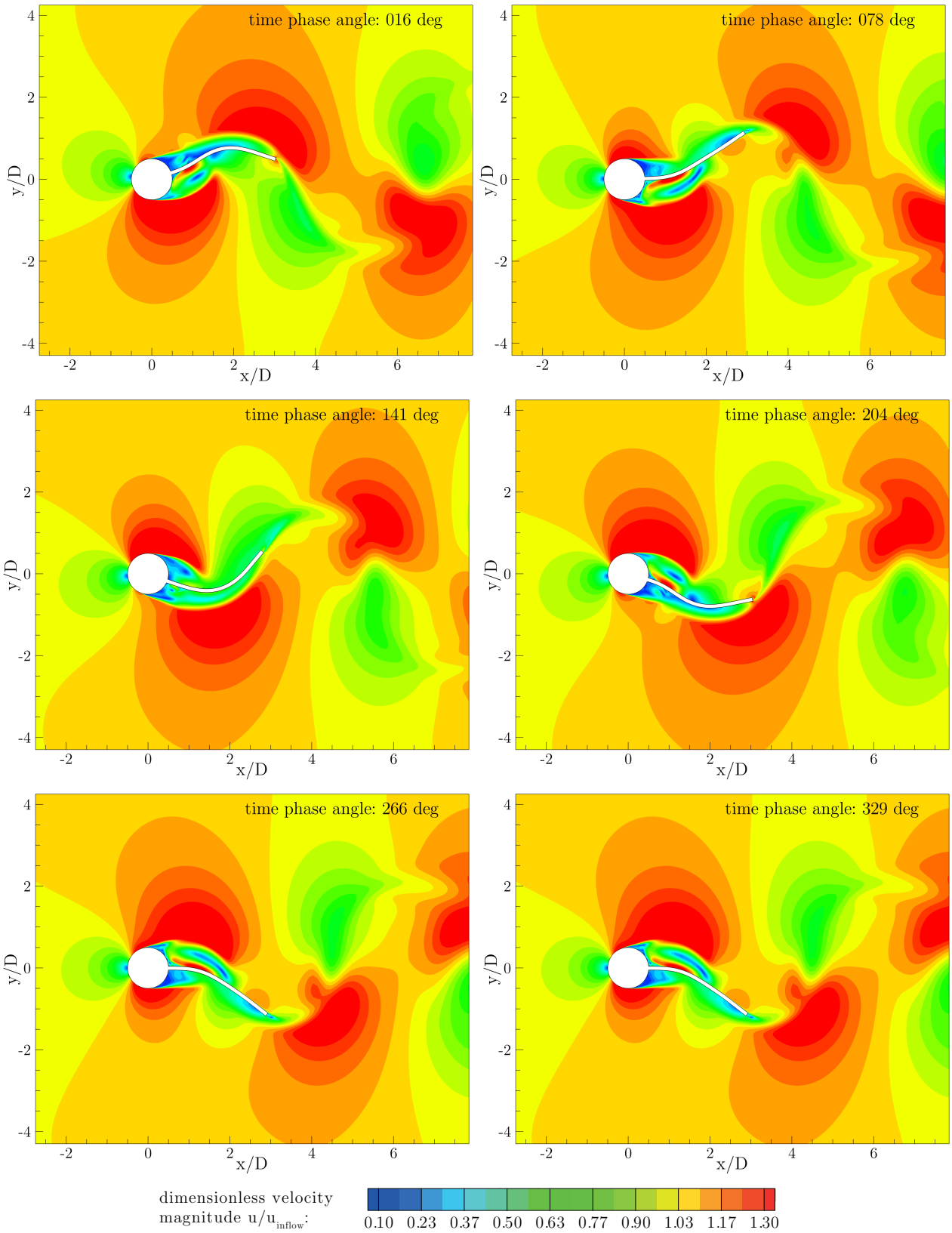

Figure 223: FSI-PfS-2*b*: Predicted flow and structural results for the characteristic period.

numerical and the experimental data of FSI-PfS-1*c* (which uses the same para-rubber material for the flexible plate) the agreement of the numerical predictions with the experimental data

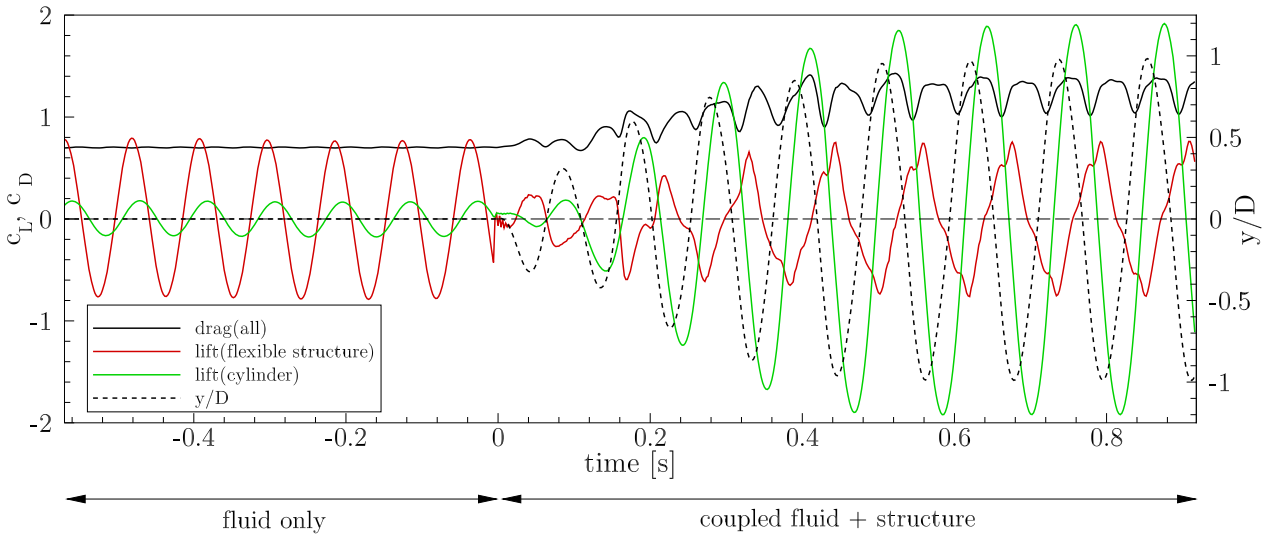

Figure 224: FSI-PfS-2*b*: Numerical results: Time histories of the drag coefficient c_D on the entire structure, the lift coefficients c_L of the front cylinder and the flexible structure and the y/D-deflections at $x/D = 3.13$ for the uncoupled and coupled solution.

is reasonable. Despite the increased complexity of both test cases (e.g., the large deflections and the additional rotational degree of freedom for FSI-PfS-2*b*) both computations agree quite well with the experiments with errors between 1% and 11% for the y-displacements and errors of about 5% for the swiveling frequencies. A summary of the comparisons is listed in Table 26.

test case	**FSI-PfS-2*a***	**FSI-PfS-2*b***
simulation	successful	successful
swiveling modes	2nd mode	2nd mode
bending shape	'8'	'8'
u_{inflow} [m/s]	1.385 m/s	1.385 m/s
symmetry	$\approx$	$\approx$
f_{num} [Hz]	11.91	8.62
f_{exp} [Hz]	11.25	8.16
error(f)	+5.60%	+5.64%
St_{num}	0.189	0.137
St_{exp}	0.179	0.130
$(y/D)_{\text{num,max}}$	0.637	0.983
$(y/D)_{\text{exp,max}}$	0.667	0.895
$(y/D)_{\text{num,min}}$	−0.639	−0.992
$(y/D)_{\text{exp,min}}$	−0.630	−0.891
error(y/D_{max})	−4.49%	+9.83%
error(y/D_{min})	+1.43%	+11.34%
validation	successful	successful

Table 26: Comparison of the numerical data with the experimental results of FSI-PfS-2*x*.

The numerical predictions of both cases FSI-PfS-2*x* confirm the experimental observations that the rotational DOF of the front cylinder has a massive impact on the system coupling between the fluid flow and the structural deflections. This is also evident by the strong increase on

the lift forces at the front cylinder in the case of FSI-PfS-2*b* and the shift of the phase delays of the y-displacements of the trailing edge to the lift forces on the front cylinder and the FSI interface. While in FSI-PfS-2*a* the lift forces act almost in-phase (lift on the front cylinder) or acyclic (lift at the FSI interface) to the y-displacements, in FSI-PfS-2*b* the phase delays are changed especially for the y/D-displacements which now follows the lift force on the front cylinder by about 292 deg. The lift force at the FSI interface remains almost acyclic with the y-deflections at the trailing edge of the cylinder. Noticeable is the strong increase of the drag force in FSI-PfS-2*b* by about 325% compared to FSI-PfS-2*a*, which refers to the increased structural deflections and the rotation of the front cylinder.

In the journal paper (De Nayer and Breuer, 2014) and the QNET publication an additional detailed comparison to coupled LES predictions of FSI-PfS-2*a* is carried out.

10.2.3. FSI-PfS-3x (Three-dimensional geometry)

In the experiments the test cases FSI-PfS-3*a* (fixed cone with attached EPDM rubber plate) and FSI-PfS-3*b* (fixed cone with attached para-rubber plate) reveal significant three-dimensional effects in the flow and the structural deformations. To take these spatial phenomena into account, in both configurations a three-dimensional mesh is used in the computations. Again, the coupled FSI simulations are carried out using ANSYS® CFX 14.0 and ANSYS® Mechanical 14.0 (details of the numerical set-up are given in Section 9.2). Due to the limitation in the element number of the fluid domain, only qualitative results are expected. In the following paragraphs the numerical results are presented and compared with the experimental results.

FSI-PfS-3a

FSI-PfS-3*a* consists of the tapered cylinder with an attached EPDM rubber plate. The inflow velocity is set to $u_{\text{inflow}} = 0.97$ m/s which corresponds to a Reynolds number of $\text{Re} = 32,000$ (related to the small cone diameter $D = 0.022$ m). As visible in Fig. 225 the numerical simulation reaches a periodic symmetric oscillation state within 2.0 s after releasing the flexible structure. The periodic state is characterized by large deflections with $(y/D)_{\text{large}} = \pm 0.494$ behind the large cone diameter at $(z/D)_{\text{large}} = -2.72$ and smaller displacements behind the middle ($(y/D)_{\text{middle}} = \pm 0.191$) and small cone diameter ($(y/D)_{\text{small}} = \pm 0.194$) at $(z/D)_{\text{middle}} = 0$ and $(z/D)_{\text{small}} = 2.72$, respectively. While the deflections behind the large and middle diameter are almost in-phase to each other, the deflection downstream the small cone diameter has an almost acyclic behavior to them. That means that the plate deformation is driven by the large vorticies generated at the larger side of the cone, while the plate at the small end of the cone is streaked. Thus, the fluid forces at the smaller end of the cone are much smaller than on the larger parts. Surprisingly the displacements at the middle and the small cone diameter are almost equal and much smaller than the deflections downstream of the large cone. The fact that the smallest deflections are reached in the mid-plane and the non-existing phase difference in the deflections between the large and the middle plane suggests an unphysical prediction of this case referring to the corresponding experimental structural results.

The comparison of the numerical data with the phase-averaged experimental results of the deflections are presented in Fig. 226. Obviously, a wave-like deformation of the plate is present for the chosen inflow velocity in the experiments (characterized by decreasing displacements with decreasing diameter and reasonable phase differences). This behavior is not observed in the numerical data. The predicted swiveling frequency is calculated to $f_{\text{3a,num}} = 6.29$ Hz and differs significantly from the experimentally measured value ($f_{\text{3a,exp}} = 5.77$ Hz) by about 9.91%.

The predicted flow fields including the deformed structure at the three different planes are shown in Fig. 227 for the phase angle of 266 deg. In comparison to the experimental flow data for this test case in Figs. 168 and 169 no significant disagreements in the flow fields in terms of the flow phenomena present are noticeable. Acceleration areas, vortex sizes and positions are in a good agreement to the measured data. Variations correspond to the different structural deformation especially to the unphysical phase delay and its impact on the flow. Since the structural deflections are small towards the small cone diameter, its influence on the flow is

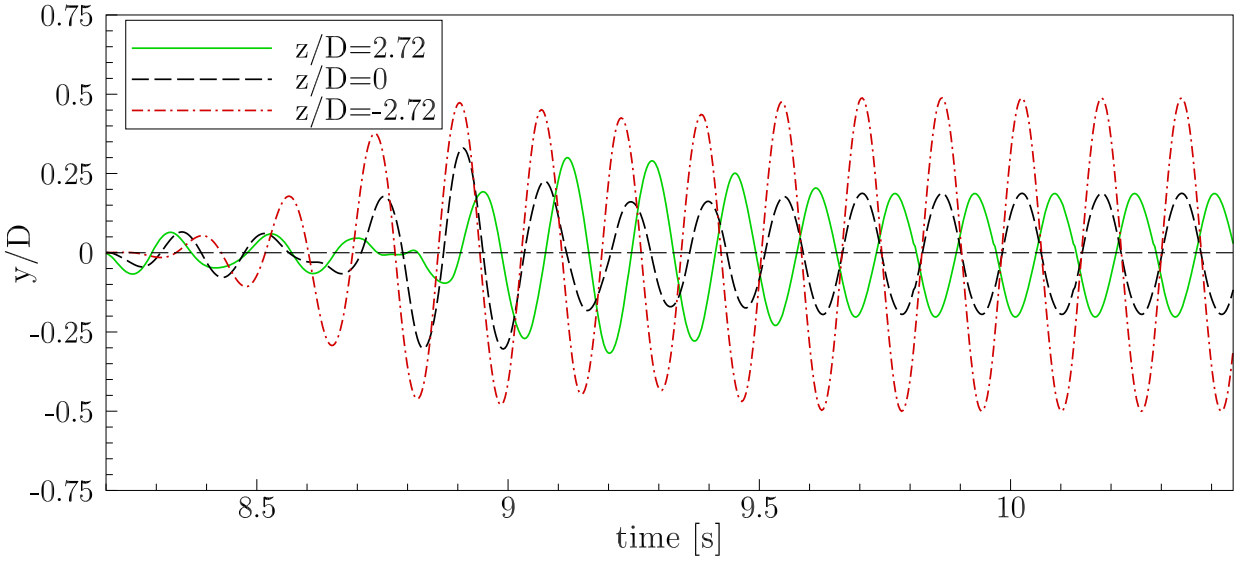

Figure 225: FSI-PfS-3*a*: Numerical structure results: a) Time histories of the y/D displacements at the three planes $(z/D)_{\text{large}} = -2.72$, $(z/D)_{\text{middle}} = 0$ and $(z/D)_{\text{small}} = 2.72$ for the monitoring point at $x/D = 3.13$.

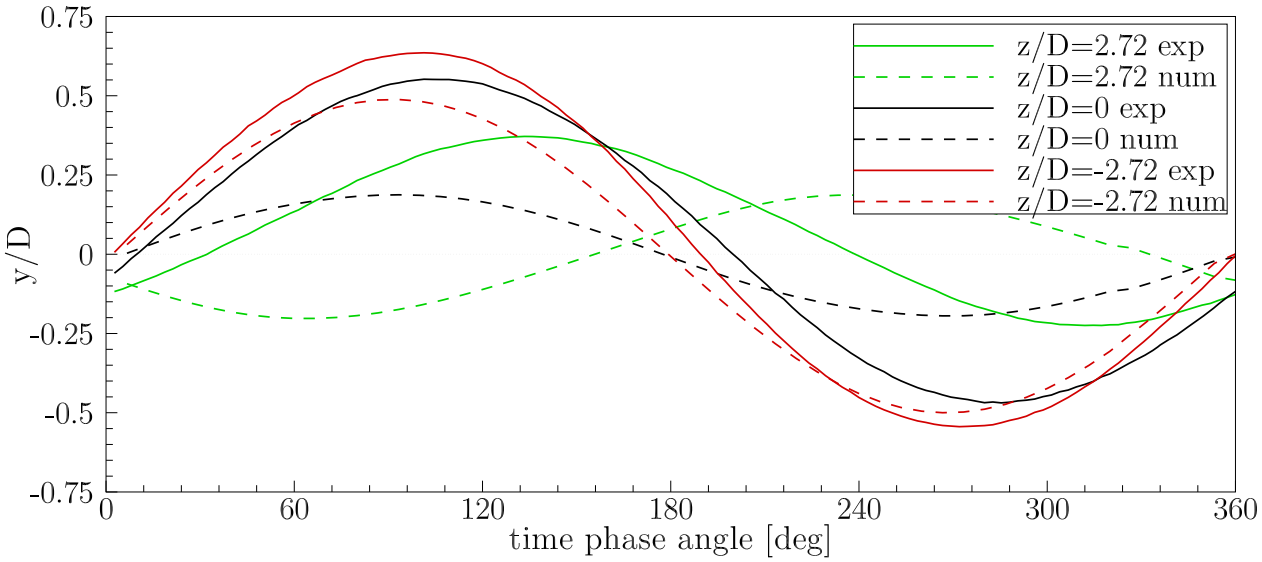

Figure 226: FSI-PfS-3*a*: Comparison of experimental and numerical structural results: Characteristic period of the y/D displacements at the three planes $(z/D)_{\text{large}} = -2.72$, $(z/D)_{\text{middle}} = 0$ and $(z/D)_{\text{small}} = 2.72$ for the monitoring point at $x/D = 3.13$.

also rather small. It can be assumed that the inertia of structural deformation lead by at the large cone diameter is more significant than on the pressure forces induced by the vortex shedding at the small cone diameter. That means that the vortex shedding is generated in a "normal" manner and not significantly altered by the structural deflections downstream the small cone diameter and roughly matches the measured data. Due to the large deviations of the predicted structural motion to the measured data, it can be assumed that the simulation produces an unphysical solution of the system (including the applied model, computational grid or boundary conditions). Furthermore, it is assumed that the coarse resolution of the

numerical grid results in an imprecise prediction of this test case.

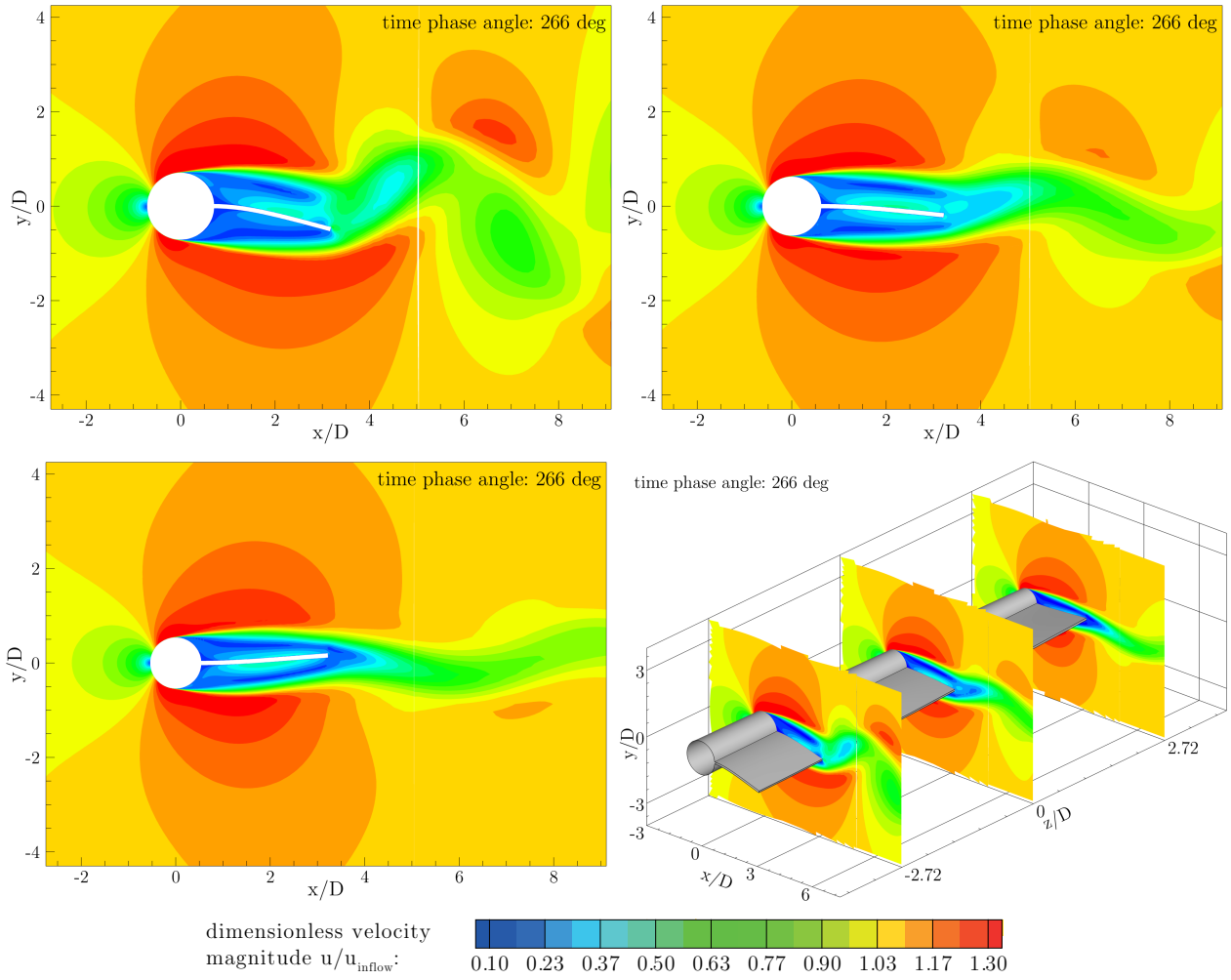

Figure 227: FSI-PfS-3a: Predicted flow and structure results at the three planes $(z/D)_{\text{large}} = -2.72$, $(z/D)_{\text{middle}} = 0$ and $(z/D)_{\text{small}} = 2.72$ for the time phase angle of 266 deg.

A possible explanation for the deviations is as follows. The numerical model of this test case neglects the small gaps between the flexible plate and the channel walls. In the experiments the edges of the plate are fully free. That means that displacements of the plate tips in positive or negative z-direction are possible and take place during the three-dimensional structure deformations. During the wave-like motion of the flexible plate observed in the experiment, the plate tips tend to its center and leave their initial z-plane near the lateral channel walls. In the experiments this motion is unproblematic, while the boundary conditions for the structure in the numerical simulation can not handle this effect. Since the gaps between the walls and the structure are not discretized in the fluid model, a dislocation of the grid nodes on the lateral sides of the flexible plate would lead to an undefined space in the coupled FSI model. On the contrary, the boundary conditions of the structural model describe the lateral sides of the plate by a frictionless support. Here, motions in x- and y-directions are allowed while z-displacements are forbidden, which means that the plate is bounded at the sides of the computational domain. Consequently, every three-dimensional deformation of the plate induces a stress which acts against the deformation. That also means that an added artificial

stiffness of the flexible plate is introduced by the improper boundary conditions. Implications of this effect are the wrongly predicted structural deformations and their impact on the flow. To reduce the influence of this out-of-plane deformation, several rows of elements on the lateral sides of the plate are replaced by artificial, more elastic elements in the structural model. These elements with a reduced YOUNG's modulus are supposed to compensate the z-displacements by stretching or compressing the artificial material. Different approaches (isotropic or anisotropic materials, different YOUNG's moduli ranging from $E \approx 10^{-4}$ to 10^{-1} MPa) are tested but failed for miscellaneous reasons. For elements with a higher YOUNG's modulus (towards $E \approx 10^{-1}$ MPa) the influence on the structural deformation remains present. Simulations with elements with a lower YOUNG's modulus (towards $E \approx 10^{-4}$MPa) are faced with problems of convergence and negative volumes. For the last case, the stiffer rubber material penetrates the softer artificial material and the simulation fails, too. Thus no reasonable solution to this problem was found.

FSI-PfS-3b

In the experiments the data of the flow and the structure of FSI-PfS-3*b* (para-rubber plate instead of EPDM rubber plate) appears in similar ranges as the measured results of FSI-PfS-3*a*. Nevertheless, a different deflection behavior is observed. While in FSI-PfS-3*a* a wave-like behavior is observed, the mid-plane of the structure in FSI-PfS-3*b* reaches the extrema first followed by the parts downstream the large and later the small cone diameter.
Since changes in the simulation set-up are made only concerning the material characteristics and the inflow velocity, no large differences to the results mentioned in the previous paragraph are expected. However, despite the almost equal set-up of FSI-PfS-3*b* compared to FSI-PfS-3*a*, the computation reveals another oscillation state.
As shown in Fig. 228 the simulation reaches a periodic and symmetric swiveling state about 2.5 *s* after the release of the flexible para-rubber plate. After the initial phase the deformations downstream the large and small cone diameter are large and almost equal (both $y/D = \pm 0.49$) but phase-shifted by about 100 deg to each other. The deflections in the mid-plane are smaller with only $y/D = \pm 0.36$. They reach their extrema nearly in the middle between the large and the small plane (the phase delay at the plane $(z/D)_{\text{middle}} = 0$ is +55 deg and at the plane $(z/D)_{\text{small}} = 2.72$ it is +100 deg with respect to the plane at $(z/D)_{\text{large}} = -2.72$).

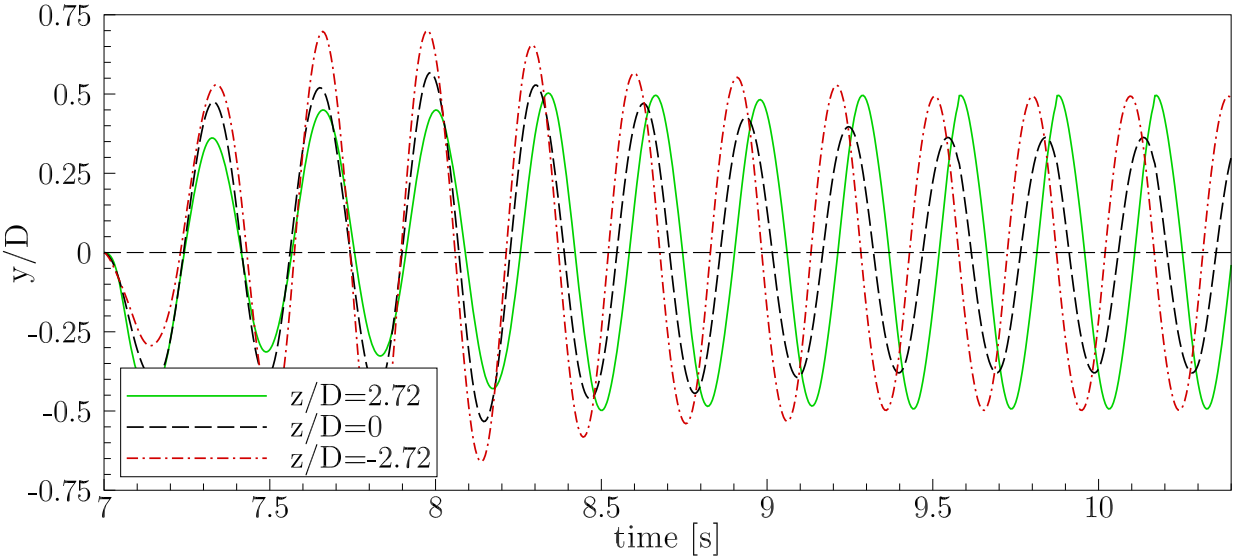

Figure 228: FSI-PfS-3*b*: Numerical structure results: a) Time histories of the y/D displacements at the three planes $(z/D)_{\text{large}} = -2.72$, $(z/D)_{\text{middle}} = 0$ and $(z/D)_{\text{small}} = 2.72$ for the monitoring point at $x/D = 3.13$.

In the prediction a wave-like deflection of the flexible plate is observed. That means that first the plane at the large cone diameter reaches its extrema after the mid-plane and finally the plane at the small cone diameter. In the experiments, however, a different order is noticed. Here, the mid-plane reaches at first its deflection extrema followed by the large plane and the small plane. Furthermore, in the experiments the phase delays between the planes are significantly shorter than in the predictions. In contrast to the numerical results of FSI-PfS-3*a* no acyclic deformations in the mid-plane are present. The predicted maximal and minimal y/D-deflections itself do not match the experimentally measured values. While the

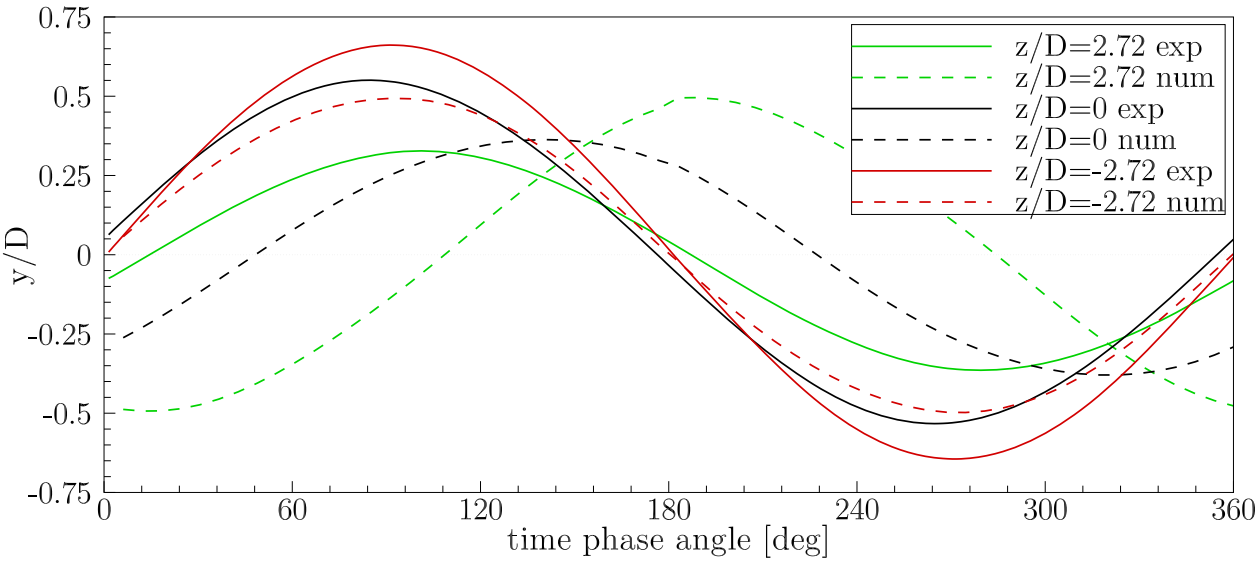

Figure 229: FSI-PfS-3*b*: Comparison of experimental and numerical structural results: Characteristic period of the y/D displacements at the three planes $(z/D)_{\text{large}} = -2.72$, $(z/D)_{\text{middle}} = 0$ and $(z/D)_{\text{small}} = 2.72$ for the monitoring point at $x/D = 3.13$.

displacements downstream of the large and the middle cone diameter are under-predicted, the deflections at the small cone diameter are over-predicted. The oscillation frequency is predicted to $f_{3\text{b,num}} = 3.39$ Hz and differs by about 5.94% from the measured frequency of $f_{3\text{b,exp}} = 3.20$ Hz.

Comparing the experimentally measured flow fields (see Figs. 179 and 180) with the predicted flow (Fig. 230) at a phase angle of 266 deg, a reasonable agreement is visible. Similar to the flow prediction of FSI-PfS-3*a* all major flow features are well predicted in size and appearance (variations are caused by the influences of the wrongly predicted structural deflections and the phase delays). It is assumed that the same problem of artificially induced stresses caused by the inappropriate boundary conditions for the three-dimensional deformations as present in the predictions of FSI-PfS-3*a* are responsible for the failure of the simulations of FSI-PfS-3*b*.

FSI-PfS-3x - Conclusions

The predictions of the three-dimensional test cases FSI-PfS-3*x* reveal major problems in the modeling of the coupled system. According to the experimental results a three-dimensional deformation behavior of the flexible plate is present in both test cases. That means that the lateral sides of the rubber plate tend to its center and leave their initial z-plane. However, in the predictions the lateral sides of the rubber plate are bound to a fixed geometry of the structural domain. Therefore, a displacement in z-direction may generate an unphysical/undefined space in the fluid domain. Since this issue could not be solved in the present work, a large mismatch to the structural results of the experiments is found. Here, mismatches regarding the displacements, the swiveling mode and the corresponding phase delays of the flexible plate are observed. A quantitative comparison of both test cases with the corresponding experimental results is given in Table 27.

The analysis of the predicted flow fields show that all relevant flow effects are nevertheless

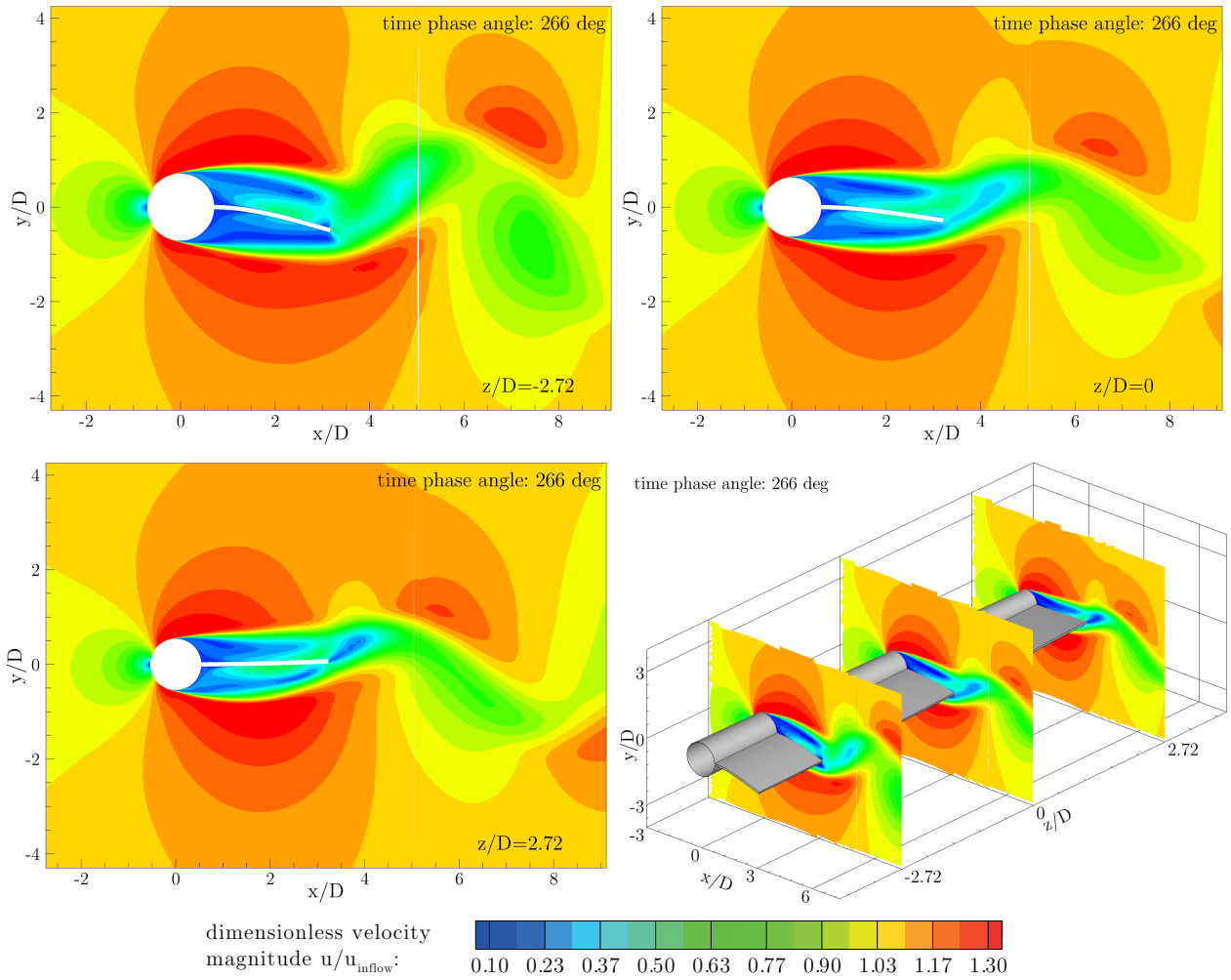

Figure 230: FSI-PfS-3*b*: Predicted flow and structure results at the three planes $(z/D)_{\text{large}} = -2.72$, $(z/D)_{\text{middle}} = 0$ and $(z/D)_{\text{small}} = 2.72$ for the time phase angle of 266 deg.

reasonably predicted even if the quality of the results is questionable due to the coarse resolution of the numerical grid applied in both cases. This fact supports the thesis that the inappropriate structural model or in detail its false lateral boundary conditions are responsible for the failure of the coupled computations.

test case	**FSI-PfS-3***a*	**FSI-PfS-3***b*
simulation	failed	failed
behavior	3D	3D
u_{inflow} [m/s]	0.969 m/s	0.549 m/s
symmetry	✓	✓
f_{num} [Hz]	6.29	3.39
f_{exp} [Hz]	5.77	3.20
error(f)	+9.91%	+5.94%
St_{num}	0.143	0.136
St_{exp}	0.131	0.128
$(y/D)_{\text{num,large}}$	±0.49	±0.49
$(y/D)_{\text{exp,large}}$	±0.54	±0.66
error$(y/D)_{\text{large}}$	±9.26%	±25.76%
$(y/D)_{\text{num,middle}}$	±0.19	±0.36
$(y/D)_{\text{exp,middle}}$	±0.46	±0.56
error$(y/D)_{\text{middle}}$	±58.70%	±35.71%
$(y/D)_{\text{num,small}}$	±0.19	±0.49
$(y/D)_{\text{exp,small}}$	±0.22	±0.30
error$(y/D)_{\text{small}}$	±13.64%	±63.33%
validation	failed	failed

Table 27: Comparison of the numerical data with the experimental results of FSI-PfS-3x.

10.2.4. FSI-PfS-4x (Application-based test cases)

The application-based test cases FSI-PfS-4x uses three-dimensional computational grids to investigate the vortex-induced vibrations of the flexible cylinder beam without any surrounding structures (FSI-PfS-4a) or in an arrangement of 3 $\times$ 3 rigid cylinders (FSI-PfS-4b), where the central cylinder is flexible. Both simulations are performed with the usage of the FSI environment of ANSYS® Mechanical 14.0 and ANSYS® CFX 14.0 (refer to the detailed description of the computational set-up in Section 9.3).

FSI-PfS-4a

The time history of the x/d- and y/d-displacements of the cylinder tip at the plane $z/d = 20.63$ are shown in Fig. 231. Within 0.6 s a quasi-periodic oscillation state of the cylinder tip is reached. During the development the y/d-deflections obtain this swiveling state faster than the x/d bending. After the initial phase, the deflections reach y/d-values of ± 1.30 and x/d bends between $(x/d)_{\text{num,min}} = 1.30$ and $(x/d)_{\text{num,max}} = 2.45$. The oscillation frequency is calculated to 27.03 Hz (St = 0.128).

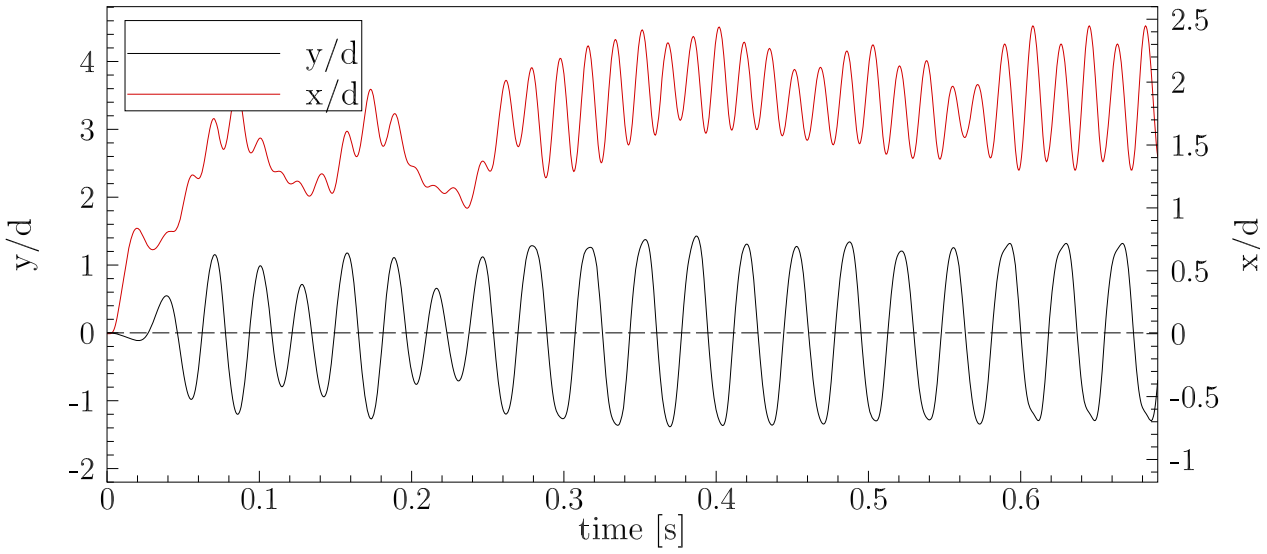

Figure 231: FSI-PfS-4a: Numerical structure results: Time histories of the x/d- and y/d displacements of the center of the cylinder at the monitoring plane $z/D = 20.63$.

The lock-in state is plotted in Fig. 232a and compared with the measured data of the phase-averaged reference period. In Fig. 232b the xy-trajectory of the cylinder tip at $z/d = 20.63$ is illustrated and reveals large disagreements between the simulation and the experimental data. The predicted motion path is slightly asymmetric due to unknown reasons. The path describes a distorted "8" which resembles the measured motion path concerning its form but differs in its range. While the cylinder tip is more bended (about one cylinder diameter) in x/d-direction in the experiments, the y/d-deflections are strongly over-predicted by the simulations. Several reasons are conceivable for the large discrepancy. The most probable reason is the insufficient spatial resolution of the three-dimensional computational grid. It is assumed, that this issue has a strong influence on the results especially on the load distribution of the flow

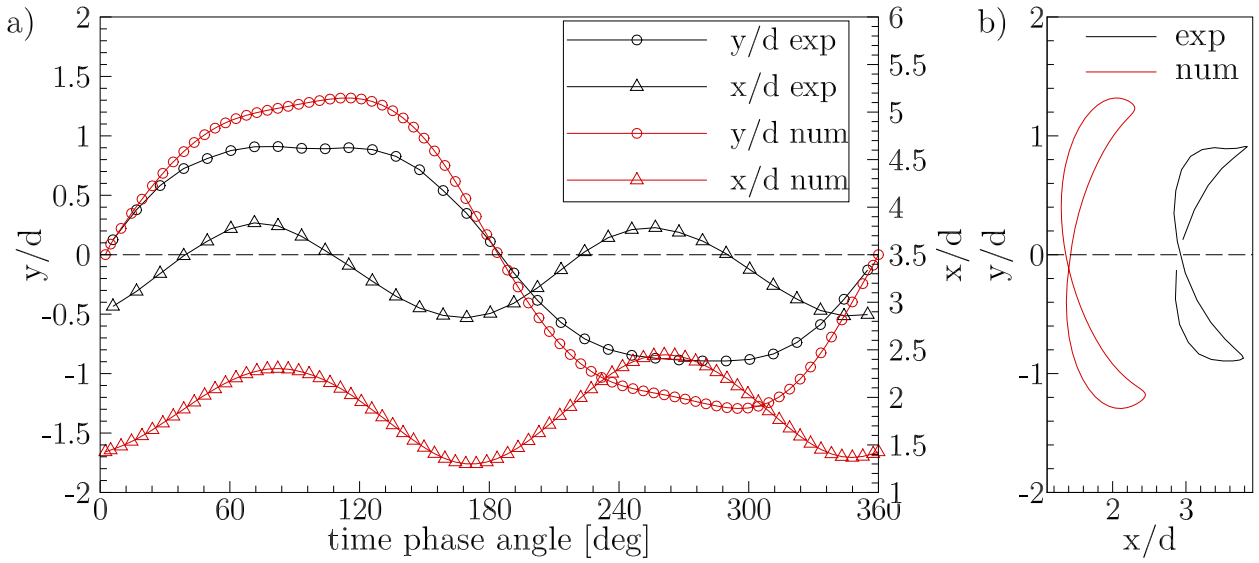

Figure 232: FSI-PfS-4*a*: Comparison of experimental and numerical structural results: a) Structural deflections x/d and y/d; b) Structural xy-motion path, both for the characteristic period at the center of the cylinder at the monitoring plane $z/d = 20.63$.

onto the structure. Since the flow in the tip region is assumed to be highly unsteady and three-dimensional, the coarse grid resolution and the URANS turbulence model are not able to reproduce the complex physical process, there. Another explanation for the disagreements may be found in the structural predictions. The high frequency of the cylinder motion implies large deformation velocities. As a consequence the applied material model can not represent the velocity-related structural effects of softening or hardening (Kästner et al., 2012) and under- or overpredicts the structural deformations. Furthermore, the long settlement phase of the x/d-deflections observed in the experiments indicate a problematic structural deformation behavior (slowly increasing bending of the free end of cylinder in x-direction) which is not reproduced by the present numerical model. Unsteady material testings of the polyethylene material applied for the flexible cylinder may lead to further insights to the unsteady deformation behavior and explain the disagreements between the simulations and the experiments.

Figure 233a illustrates the predicted flow in the plane near the cylinder tip ($z/d = 20.63$) at the time phase angle of 78 deg. At this phase angle the structure reaches its maximum deflection in x- and y-directions. On the upper side of the cylinder a large acceleration region is formed. On the lower and backward side of the cylinder tip a wake area is present caused by its prior fast motion through the flow field. Similar to the measured flow fields the broad wake in the range of the cylinder motion and the two pairs of shedding vorticies downstream of it are noticeable (Fig. 233b). Although these phenomena are also visible in the experimental flow results, a more detailed insight into the major three-dimensional flow structures is possible in the predictions. While the shed vorticies in case of a rigid cylinder are almost two-dimensional, due to the bending in the coupled case the vorticies get a three-dimensional shape (Fig. 234). The motion of the cylinder tip produces high vorticity and transfers energy into those flow regions which are only weakly influenced (towards the clamping).

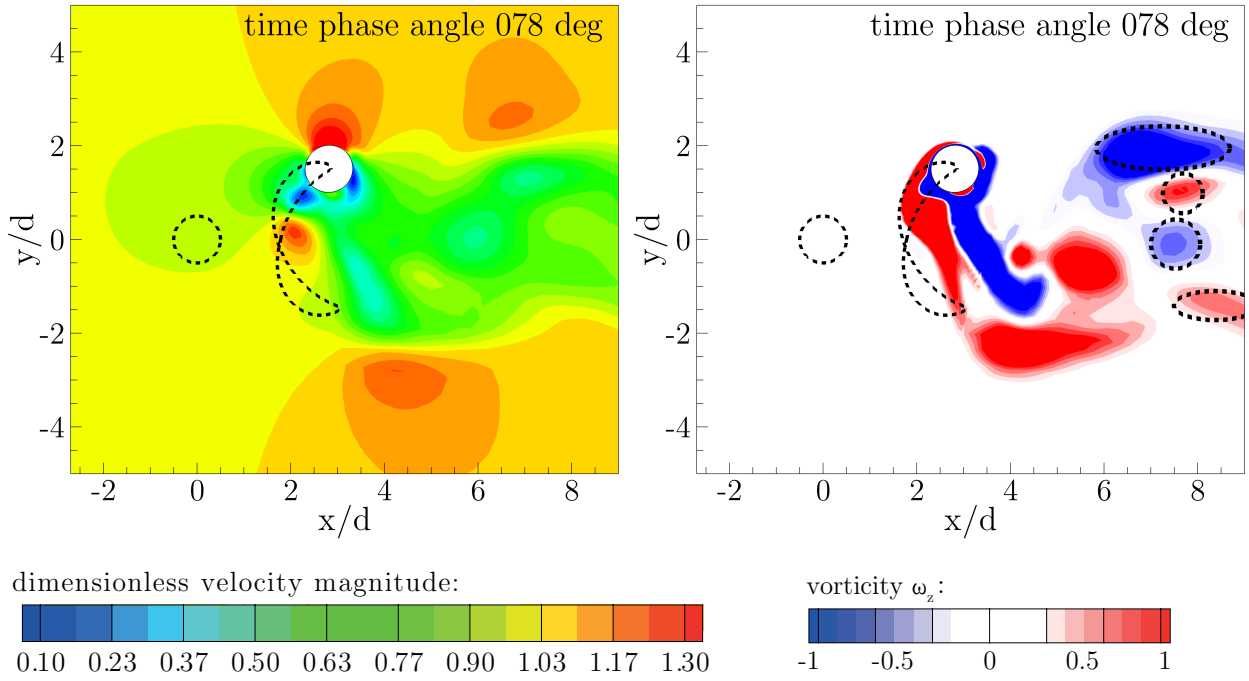

Figure 233: FSI-PfS-4*a*: Predicted flow and structural results: a) Velocity magnitude; b) Vorticity component ω_z both at the phase angle of 78 deg and the monitoring plane $z/d = 20.63$.

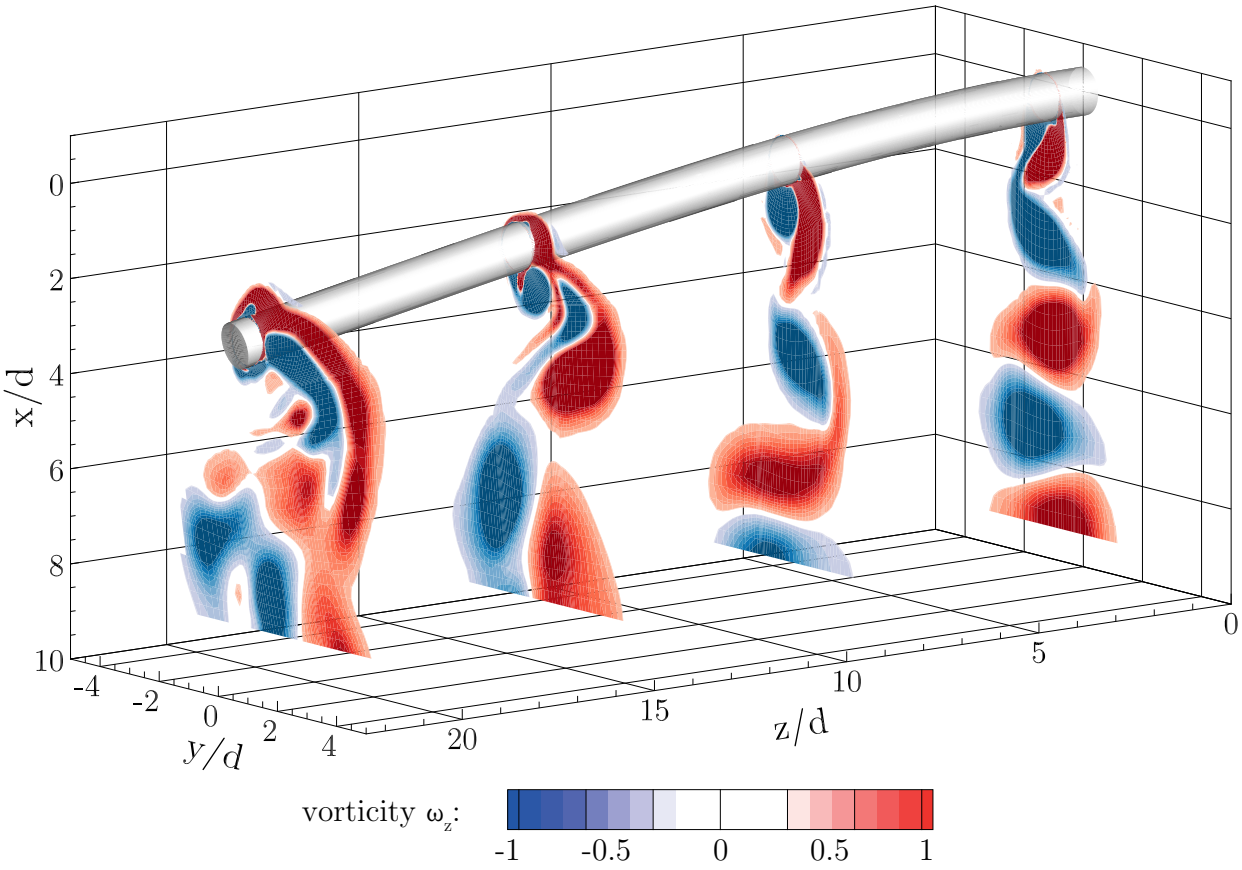

Figure 234: FSI-PfS-4*a*: Predicted flow and structural results: Vorticity magnitude at the phase angle of 204 deg and four monitoring planes at $z/d = 1$, $z/d = 7.5$, $z/d = 15$ and $z/d = 20.63$, respectively.

FSI-PfS-4b

Unfortunately, the numerical prediction of the test case FSI-PfS-4*b* failed for various attempts. Similar to the previous test cases the first coupled simulations are initialized by an unsteady prediction without the FSI coupling. After releasing the flexible cylinder in the center of the 3 × 3 arrangement a strong overshoot of its structural deflections in streamwise x-direction is predicted. In Fig. 235 the result of this FSI computation from an unsteady developed flow is depicted. Remarkable is the strong increase of the x/d-deflections within the first time steps. Only due to the simultaneously appearing large deflections in x- and y-direction, no contact of the flexible cylinder with the rigid cylinders downstream occurs. Despite the small decrease of the structural deflection of the cylinder tip within the following time steps after 0.107 s, the over-prediction of the deformation leads to a fatal contact of the flexible cylinder with the rigid cylinder further downstream. Since the numerical model does not consider structural contacts, the computation is aborted and failed. Since the large drag forces are assumed to be responsible for the structural over-predictions, several computations with changed initial conditions (e.g., quiescent fluid at the FSI release) are performed to solve this issue. Unfortunately, no configuration is able to avoid the over-prediction, and all failed due to the same reason. It is assumed that the coarse computational grid has a large impact on this simulation failure. In the experiments a highly unsteady three-dimensional flow field inside and behind the cylinder array is detected. Due to the coarse grid the predictions can not reproduce the high fluctuations present in flow field leading to a unstable computation. This is also evident by the corresponding convergence behavior of the simulation. In every configuration a disproportionally large number of coupling iterations (≈ 100) are necessary to compute a single time step. Due to the large efforts and the expected low prediction quality on the present coarse numerical grid, no additional tests are performed.

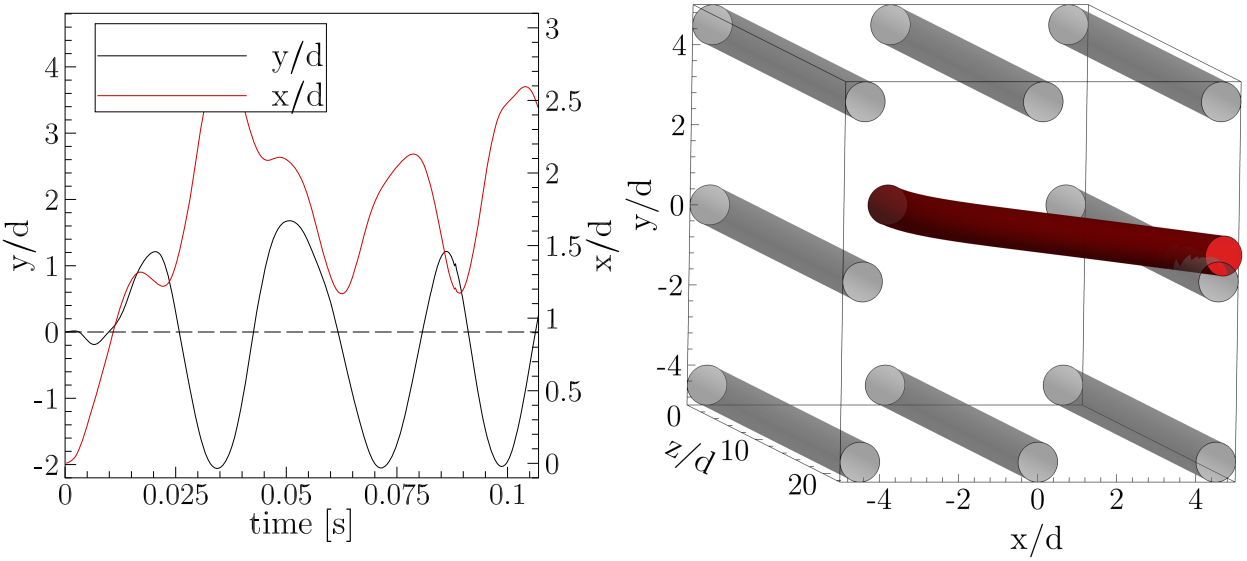

Figure 235: FSI-PfS-4*b*: Numerical structural results: a) Time histories of the x/d- and y/d-displacements of the center of the cylinder at the monitoring plane $z/d = 20.63$, b) illustration of the structural geometry at the last time step of the failed computation.

FSI-PfS-4x - Conclusions

In the computations of FSI-PfS-4x several major problems appear leading to an unsuccessful validation of FSI-PfS-4a and a completely failed prediction of FSI-PfS-4b. In the case of the single cylinder in FSI-PfS-4a a qualitative agreement with the experimental results is achieved for the cylinder trajectory (distorted "8"). However, large quantitative disagreements are found in the structural deflection of the cylinder tip. Here, the y-deflections are strongly over-predicted (+44%) while the x-deflections are strongly under-predicted (−36%). Several reasons are assumed to be responsible for the mismatch (see Table 28). The largest influence is assigned to the coarse computational grid applied in the predictions. Furthermore, velocity-related material effects like softening or hardening are not considered in the present material model. These effects are present in FSI-PfS-4x as indicated by the experimental results discussed in Section 10.1.3.
Related to the same issues the computation of the flexible cylinder within the 3 × 3 cylinder arrangement in FSI-PfS-4b failed completely. Here, the coarse computational grid and the improper material behavior lead to a strong over-prediction of the structural deflections of the cylinder tip. This results in a contact of the flexible cylinder with the rigid cylinder located downstream of it and aborted the computation.

test case	**FSI-PfS-4a**	**FSI-PfS-4b**
simulation	successful	failed
behavior	3D	3D
bending shape	'8'	'('
u_{inflow} [m/s]	1.69 m/s	1.69 m/s
symmetry	✓	–
f_{num} [Hz]	27.03	–
f_{exp} [Hz]	29.39	26.28
error(f)	−8.03%	–
St_{num}	0.128	–
St_{exp}	0.139	0.124
$(y/d)_{\text{num}}$	1.30	–
$(y/d)_{\text{exp}}$	0.90	1.27
error(y/d)	+44.44%	–
$(x/d)_{\text{num,max}}$	2.45	–
$(x/d)_{\text{exp,max}}$	3.85	3.00
error$(x/d)_{\text{max}}$	−36.36%	–
$(x/d)_{\text{num,min}}$	1.30	–
$(x/d)_{\text{exp,min}}$	2.84	2.32
error$(x/d)_{\text{min}}$	−54.22%	–
validation	failed	failed

Table 28: Comparison of the numerical data with the experimental results of FSI-PfS-4x.

11. Conclusions and Outlook

The interaction of a flowing medium and a solid structure is a common physical phenomenon in various technical applications. The better knowledge due to the going research on those multi-physical processes enables their usage and optimization. Common examples for fluid-structure interactions in terms of industrial applications are blade vibrations at turbines, aerodynamic flutter of airfoils or vibrations in tube bundles applied in heat exchangers. Since many applications are a part of complex technical facilities, the precise understanding of FSI phenomena is also a safety issue. A common example is the unexpected vibration of a tube bundle caused by a flow-induced excitation that leads to a fatal and expensive failure of the heat exchanger. Therefore, the prediction of fluid-structure interactions is an increasingly important issue in the design of technical applications. Since the research on FSI phenomena is ongoing for a long time, several methods were developed for their estimation or prediction. Owing to the increase in computational power over the last two decades the numerical prediction of complex multi-physical systems is possible. While various coupling approaches were developed, a lack of fundamental data for their evaluation exists. To fully validate and optimize a coupling approach, the comparison to experimental data is indispensable. Therefore, experiments under clearly defined operating conditions are necessary to develop proven test configurations called test cases or benchmarks.

In the last decade several different FSI test configurations were developed to validate FSI predictions. Very common is the comparison or validation of numerical FSI approaches with other numerical predictions (e.g., the widely-used laminar benchmark of Turek and Hron (2006)). Application-oriented benchmarks (e.g., tension riser studies related to offshore oil exploration) were carried out and provide experimental data but often not comprehensively enough for an extensive validation process of simulation approaches. Since vortex-induced-vibrations (VIV) on cylinders have been a common issue in many industry-relevant applications (e.g., the heat exchanger already mentioned), a lot of test scenarios related to cylinder flows were published. Here, primarily elastically mounted rigid cylinders were exposed to streamwise flows or cross-flows to study the mechanisms of VIV. Since these investigations are well-documented and provide a proven knowledge of the physical coupling between the flow and the structure, also several FSI benchmarks are related to these configurations. Nevertheless, most of these test cases include no structural deformations and therefore no complete data on bidirectional fluid-structure interactions. A comprehensive data base (experimental data of the flow and structural motion) is provided by the studies of Gomes et al. (2010) and Gomes and Lienhart (2013). These studies delivered reliable experimental data on several bidirectionally coupled FSI test cases in the laminar and turbulent flow regime. In Gomes and Lienhart (2013) the structure consists of a rigid rotatable circular cylinder with a thin steel plate attached to it. At the trailing edge of the thin sheet a rectangular mass is attached. Despite the extensive experimental data available for this test case not many successful predictions are published up to now. Several difficulties related to this test case (e.g., the thin geometry and the rotational mount) are reported to impede the predictions.

In summary, the benchmarks available are not sufficient to offer a complete, reliable and computationally feasible data basis for FSI validations in the turbulent regime. Therefore, this thesis

describes and analyzes several newly developed self-exciting multi-DOF (degrees of freedom) FSI test cases based on experimental and numerical methods. These test cases are developed with reference to previous studies and are modified regarding the geometry, material properties and working conditions. The coupled flow and structure responses of the different test cases investigated are chosen with respect to the predictability of the corresponding numerical simulations, the requirements of well-defined and controllable boundary conditions, the reproducibility of the results and the feasibility of precise fluid and structure measurements. By providing an extensive experimental data base reliable measurement data for the validation of FSI methods are available to fill the gap in the literature. A further investigation of the FSI coupling mechanisms analyzes the different geometrical and structural dependencies on the FSI phenomenon. Based on corresponding numerical simulations of each test case their predictability is examined and comparisons between the measurements and calculations are performed.

11.1. Conclusions

Investigated system

The experiments are performed in a water channel (Göttingen type) which was designed and built at LSTM Erlangen by Gomes and Lienhart (2006, 2010, 2013) within the DFG research unit FOR 493 (Bungartz et al., 2010). The channel has a rectangular flow path and includes several rectifiers and straighteners to guarantee an uniform inflow into the test section. The water is put in motion by an axial pump generating inflow velocities up to 6 m/s in the test section (block profile, low turbulence level $\mathrm{Tu}_{\mathrm{inflow}} = 0.022$). The fluid flows from the top to the bottom and is aligned with the gravitational acceleration. Furthermore, the test section possesses windows on three sides to allow optical measurement systems such as particle-image velocimetry and laser line triangulation. The structures investigated are attached at the backplate at the test section and additionally fixed at the front glass plate if necessary.

In the present thesis four different sets of test cases are studied. Every set has its own specific intended purpose of investigation and additionally provides a comprehensive data base for the comparison with numerical data. The first set of test cases FSI-PfS-1x ($\mathrm{Re} \approx 26,000$ to $30,500$) applies a fixed circular cylinder with an attached flexible plate ($u_{\mathrm{inflow}} = 1.18$ to 1.39 m/s). Three different materials are investigated to study their influence on the coupling between fluid and structure. FSI-PfS-1a uses a stiff EPDM rubber for the flexible tail while FSI-PfS-1b applies an even stiffer polyamide plate. In the test configuration of FSI-PfS-1c a soft para-rubber plate is attached to the front cylinder.

The second test case series FSI-PfS-2x ($u_{\mathrm{inflow}} = 1.39$ m/s, $\mathrm{Re} \approx 30,500$) is inspired by the work of Gomes and Lienhart (2010, 2013). Again a circular front cylinder with an attached flexible structure is applied. Similar to the configuration of Gomes and Lienhart (2010, 2013) an additional steel weight is attached at the end of a para-rubber plate. This steel weight ensures a two-dimensional deformation behavior and adds inertia to the coupled system for larger structural deflections. The difference between the two included configurations FSI-PfS-2a and 2b is found in the mount of the front cylinder. While the front cylinder in FSI-PfS-2a is fixed on the backplate of the flow channel, in FSI-PfS-2b the cylinder is rotationally mounted

(similar to the configurations of Gomes and Lienhart (2010, 2013)).
Technical processes which contain FSI phenomena are usually of three-dimensional kind. To take this into account, the test cases FSI-PfS-3x ($u_{\text{inflow}} = 0.55$ to 0.97 m/s, Re $\approx 18,000$ to $32,00$) is developed. Here, the three-dimensional geometry of a tapered front cylinder is suggested to create a three-dimensional flow in its wake inducing three-dimensional structural deformations of the attached rubber plate. FSI-PfS-3x contains two different configurations which differ in the flexible material and the inflow velocities. FSI-PfS-3a uses the stiff EDPM rubber and a high inflow velocity, while FSI-PfS-3b applies the soft para-rubber material and a lower inflow velocity.
The last set of test cases FSI-PfS-4x ($u_{\text{inflow}} = 1.69$ m/s, Re $\approx 13,500$) is application-oriented. As already mentioned, vortex-induced vibrations are common in many technical processes. The configuration of FSI-PfS-4x exposes a single flexible cylinder to a cross-flow (similar to heat exchanger bundles or nuclear fuel rods). One end of the flexible cylinder is fixed at the backplate of the test section, while the opposite end is free to move. The difference between the two configurations FSI-PfS-4a and 4b is that in case of FSI-PfS-4b the flexible cylinder is additionally surrounded by eight rigid cylinders in a 3×3 arrangement.

All cases have in common that the flow around the bluff body is in the subcritical regime. Consequently, the boundary layers at the surface are still laminar, but transition to turbulence takes place in the free shear layers evolving from the separated boundary layers behind the apex of the front body. The flexible structures in FSI-PfS-1x, 2x and 3x are located in the direct wake of the bluff body. There, the common phenomenon of shedding vorticies takes place and creates a von Kàrmàn vortex street. Due to the oscillating behavior of this flow phenomenon also the pressure forces at the interface between the fluid and flexible structure oscillate. Based on this excitation the structure starts to swivel and a self-induced bidirectional fluid-structure interaction takes place. Since all test cases presented in this thesis belong to the turbulent flow regime, the occurring turbulent fluctuations result in cycle-to-cycle variations of the structural deformations (also known as fluctuation-induced excitation mechanism, FIE). Depending on the inflow velocity, the corresponding Reynolds number and the structural properties, several different system excitation mechanisms are possible. As a first case, the extraneously induced excitation (EIE) is the result of fluctuations in the field variables (velocity or pressure) itself (e.g., turbulence). The instability-induced excitations (IIE) are caused by flow instabilities such as interface instabilities, impinging shear layers or vortex shedding. For the instability-induced excitation a fluid resonance appears if the properties of the flow and structure correlate (e.g., the material properties of the structure allows a swiveling motion close to the characteristic frequency of the flow). In this case the system coupling generates a quasi-periodic state (lock-in), where the frequency of the flow instability (here the vortex shedding) and the structure response reach a similar level. Closely connected to IIE is the movement-induced excitation (MIE). Here, the motion of the structure and the thereby occurring forces on their surface amplifies the structural response and thus are again self-induced. In contrast to IIE, MIE is inherently linked to the body movement and disappears if the structure comes to rest. MIE is characterized by large periodic structural motions and is highly affected by the surrounding flow. Both, IIE and MIE enormously influence the flow.

Applied investigation methods

All test cases are investigated using precise measuring techniques and coupled numerical predictions. The experimental investigations of a FSI problem have to describe both, the structure and the fluid coupled in time. Since the turbulent flow causes cycle-to-cycle variations and significant three-dimensional deformations of the structure appears in several test cases, a precise and flexible measuring technique is necessary to determine the structural deflections and the fluid motion.

In all test cases a 2D particle-image velocimetry (PIV) setup is applied to measure the velocity fields of the flow in the xy-plane around the moving structure. The PIV method is a contactless standard technique in experimental fluid mechanics for measuring planar flow fields. A single CCD camera measures the two components of the fluid velocity within the planar section illuminated by a laser light sheet. The fluid is laden by small particles, which are following the flow and reflect the laser light. By taking two images of the reflection fields in a short time interval, a cross-correlation technique can estimate the displacement of the particles using an equidistant grid. Using these displacements and the time interval Δt, the velocity field in the illuminated plane can be calculated.

The structural deformations are measured using a laser line triangulation sensor (LLT). Here, the laser triangulation method is applied. A laser line projected on the surface of the object to be measured is detected by a high-speed line camera which precisely determines small structural displacements. Based on the orientation of the LLT sensor, profiles of the structural deflections in the xy- and the yz-plane can be measured with a high spatial and temporal resolution.

Both, the LLT technique for detecting the structural deflections and the PIV technique for the measurement of the planar flow fields are coupled to cover a complete measurement of the state of the coupled system. As already mentioned, cycle-to-cycle fluctuations are present in the fluid flow and the structural deformations representing a quasi-periodic FSI system. In order to be able to compare numerical results and experimental measurements, the irregular fluctuations are averaged out by using a phase-averaging procedure. In this procedure the single flow and structure measurements are assigned to their specific temporal instant in the swiveling period. Afterwards, similar measurements assigned to the same phase angle are appointed and averaged to reconstruct a mean period of the specific FSI problem. In this phase-averaged result the irregular cycle-to-cycle variations are eliminated and a comparison with numerical predictions is feasible.

In addition to the planar PIV flow measurements, three-dimensional flow measurements with a volumetric particle tracking system (V3V®) developed by TSI® are performed to investigate the behavior of the flow in all spatial directions. Similar to the PIV method particles in the flow are illuminated by a laser light source. Instead of a thin light sheet (PIV) a cubical laser light volume (V3V) is applied. To enable the three-dimensional particle tracking of individual particles, their spatial position is determined by a precise calibration process and the usage of three single CCD cameras defocussed on the flow volume to be investigated. A disadvantage

of this flow measurement technique is the small measurement volume and the reduced spatial resolution compared to the PIV recordings. Therefore, this method is primarily applied to analyze qualitatively the three-dimensional behavior of the flow.
The numerical predictions are carried out by the commercial multi-physics simulation environment of ANSYS® applying the Reynolds-averaged Navier-Stokes equations and the statistical RANS turbulence model (SST) on two- and three-dimensional block-structured grids. The FSI solution procedure is based on an implicit coupling algorithm between the flow solver ANSYS® CFX 14.0 and the structural solver ANSYS® Mechanical 14.0 exchanging the fluid loads at the FSI interface and the resulting structural displacements.

To determine the properties (YOUNG's modulus, the POISSON's ratio and the damping properties) of the elastic materials, several preliminary structural tests are performed. In detail, experimental studies regarding the static, the dynamic and the decay behavior of the materials are performed. The static and the dynamic tests are reproduced by ANSYS® Mechanical 14.0 to evaluate the material properties applied in the coupled numerical FSI predictions. Out of the decay tests further analytical findings on the damping behavior of the materials (EPDM, para-rubber and polyamide) are provided.
For all test cases the structural deflections (maximum and minimum deflections, swiveling frequency and Strouhal number) are determined as a function of the inflow velocity. Here, the individual characteristics of each test configuration are visible and the results are comparable to each other.

Results of FSI-PfS-1x

For FSI-PfS-1x the structural responses of the configurations 1a and 1b to the inflow velocity are quite similar, while the structural response of 1c reveals large deviations compared with the cases 1a and 1b. In FSI-PfS-1a and 1b only one quasi-periodic swiveling mode is observed. Here, the maximum and minimum deflections increase with the inflow velocity until the surrounding flow and the stiff material used for the flexible plate impedes larger structural deflections. The structural response at the finally chosen inflow velocity is characterized by mild deformations in the first swiveling mode (one bending node at the clamping of the flexible plate at the cylinder). The deflections of the flexible plate are smaller than half of the cylinder diameter ($y/D \approx \pm 0.44$) and possess a swiveling frequency of about 7.11 Hz. The additional qualitative three-dimensional flow measurements indicate an almost two-dimensional deformation behavior of the EPDM rubber plate for the phase-averaged reference period. Similar structural deflections are measured for FSI-PfS-1b with peak deflections of about $y/D \approx \pm 0.39$ and a swiveling frequency of about 8.02 Hz. By changing the material of the flexible structure to the soft para-rubber in the case FSI-PfS-1c, the swiveling behavior is significantly changed. The first difference to the cases 1a and 1b is the FSI onset which starts at lower inflow velocities. During the further development with increasing inflow velocities the first swiveling mode (similar appearance as observed in FSI-PfS-1a and 1b) is achieved with large deflections in the order of $y/D \approx \pm 0.6$. In contrast to the other two cases FSI-PfS-1c changes the swiveling

mode at a particular inflow velocity. During this transition the swiveling frequency is almost doubled to a value of about 11.39 Hz and the structural deflections are surprisingly decreased to $y/D \approx \pm 0.41$. Nevertheless, in this mode the deformations become more complex. While in the first swiveling mode only one bending node is located at the clamping of the flexible plate and the front cylinder, in the second swiveling mode an additional bending node at approximately two thirds of the plate length is observed. The flow measurements at the chosen inflow velocity confirm the doubled swiveling frequency by a larger number of shedding vorticies observed in the wake of the structure. Furthermore, the large deformation velocity of the moving structure affects the flow by generating a secondary trailing-edge vortex. This effect is not visible in the flow fields measured for FSI-PfS-1a and 1b.
In general, the system coupling in FSI-PfS-1a and 1b is assumed to be rather weak. That means that the flow is not strongly affected by the mild structural deformations and the medium swiveling frequencies present in both cases. The excitation of the system is identified to be driven by the instability of the vortex shedding present at the front cylinder. Since the vortex shedding frequency is reduced compared to the rigid configuration, it can be assumed that the stiff materials applied for the flexible plate impedes the vortex shedding like a splitter plate. Despite this frequency reduction the velocity distribution of the flow fields is rather unaffected which indicates the presence of an instability-induced excitation. In the configuration of FSI-PfS-1c the FSI coupling not only alters the lock-in frequency of the system. It also strongly affects the flow by generating the secondary trailing-edge vorticies. This indicates that the movement-induced excitation mode is found for this test configuration. The coupled two-dimensional flow and structure measurements of the benchmarks FSI-PfS-1a and 1b are reported in Breuer and Kalmbach (2011). Further contributions related to FSI-PfS-1a with extensive comparisons to numerical predictions are presented in De Nayer et al. (2012, 2014) and published at the ERCOFTAC/QNET website (http://qnet-ercoftac.cfms.org.uk).

Results of FSI-PfS-2x

The second set of FSI test cases (FSI-PfS-2x) is focused on large two-dimensional structural deformations. While the first series of test cases FSI-PfS-1x is concerned with different elastic materials to examine their influence on the FSI coupling, the second series FSI-PfS-2x employs the same material and an additional steel weight attached to the para-rubber plate. However, by applying two different test case configurations, the influence of the rotational DOF of the front body on the structural response is also examined.
The detailed measurements concerning the finally chosen inflow velocity for both benchmark cases revealed quasi-periodic and nearly symmetric structural deflections for both test cases. In general, the deflections of both configurations are large (FSI-PfS-2a: $y/D \approx \pm 0.65$, $f = 11.25$ Hz; FSI-PfS-2b: $y/D \approx \pm 0.9$, $f = 8.16$ Hz) compared to the first set of test cases FSI-PfS-1x. The additional steel weight at the end of the structure increases the inertia of the system that leads to larger deflections and the modified swiveling behavior (second swiveling mode). The assumption that the steel weight forces the system to a two-dimensional flow and structure response is proven by the additional qualitative three-dimensional flow measure-

ments. The release of the rotational DOF of the front cylinder in FSI-PfS-2*b* further increases once more the structural deflections due to its expanded range of influence. Furthermore, the special configuration of FSI-PfS-2*b* allows a rigid-body motion (i.e. a front cylinder rotation with a nearly rigid plate attached) for the lowest inflow velocities. The first swiveling mode is also present for low inflow velocities and the corresponding excitation frequencies are smaller than the second natural frequency of the structure. Nevertheless, the second swiveling mode of the structure is dominant in both test cases. The transition between the first and second mode again comes along with a doubling of the vortex shedding frequency of the fluid and the corresponding swiveling frequency of the structure in both test cases. The resulting frequency after the transition phase exceeds also the second eigenfrequency of the structure.
Referring to the FSI excitation sources, it is assumed that the instability-induced excitation (IIE) is responsible for the excitations in the first swiveling mode for low inflow velocities. With increasing inflow velocities, i.e., the investigation at the final inflow velocity of $u_{\text{inflow}} = 1.385$ m/s, the flow excitations are large enough to modify the whole system state and indicate a movement-induced excitation mode (MIE). This statement is supported by the eigenfrequency analysis of both test cases. For the chosen inflow velocity the swiveling frequencies are higher than the first and second eigenfrequencies of the structure. The investigation of the test case FSI-PfS-2*a* with coupled two- and three-dimensional flow and structure measurements is published in Kalmbach and Breuer (2012, 2013b) and at the ERCOFTAC/QNET website (http://qnet-ercoftac.cfms.org.uk).

Results of FSI-PfS-3*x*

In the third series of test cases FSI-PfS-3*x* a more complex front body geometry is applied to set-up three-dimensional FSI test cases in terms of structural deflections and fluid flow. In order to maintain most of the measures of the two-dimensional test cases FSI-PfS-1*x* and 2*x*, the front cylinder is replaced by a cone (the small cone diameter is equal to the former cylinder diameter D, while the large cone diameter measures $1.5 \cdot D$). According to the spanwise enlargement of the cone, the flexible plate attached to it is adapted to the new geometry. Both test cases FSI-PfS-3*a* and 3*b* are limited to moderate structural deflections in one dominant swiveling mode. A quasi-periodic state of the structural deformations and the fluid flow is reached in both cases but by applying different inflow velocities. Due to the increased complexity of the flow according to the three-dimensional geometry of the front body, only one quasi-periodic oscillation state (first swiveling mode) is noticed in contrast to the presence of two swiveling modes, e.g., in FSI-PfS-2*x*. In the present state a fully three-dimensional deformation of the flexible structure appears within the oscillation period. For FSI-PfS-3*a* a wave-like deformation of the plate propagates from the large cone diameter to the small cone diameter with decreasing structural deflections ($(y/D)_{\text{large}} \approx \pm 0.54$, $(y/D)_{\text{middle}} \approx \pm 0.46$, $(y/D)_{\text{small}} \approx \pm 0.22$) and a swiveling frequency of about $f = 5.77$ Hz. This behavior is consistent with the assumption of higher fluid loads caused by the larger shedding vorticies on the large side of the cone in contrast to its opposite side proven by the PIV measurements at different planes. The stiff EPDM rubber supports or eventually enables this wave-like deflection behavior. In FSI-PfS-3*b*

a different deflection behavior is observed. Here, the middle section of the plate reaches the extrema first followed by the parts downstream the large and later the small cone diameter. The structural deflections of the phase-averaged period are determined to $(y/D)_{\text{large}} \approx \pm 0.66$, $(y/D)_{\text{middle}} \approx \pm 0.56$, $(y/D)_{\text{small}} \approx \pm 0.30$ and a swiveling frequency of about $f = 3.20$ Hz. It is assumed that the soft para-rubber decreases the deformation resistance in comparison with the EPDM rubber and therefore the local characteristics of the entire structure deformation. However, in both cases the structural deflections are limited to the dimension of the front body (similar to the two-dimensional test cases without a steel weight FSI-PfS-1x) with mild variations towards the large end of the cone and stronger fluctuations downstream of the small cone diameter. Thus, the swiveling behavior of the flexible plate is strongly affected by the applied material of the rubber plate. Beside the three-dimensional deflection behavior, the low YOUNG's modulus of the para-rubber plate (FSI-PfS-3b) also reduces the critical inflow velocity of the FSI onset. As a consequence the destabilization of the quasi-periodic swiveling state commences earlier compared with the EPDM rubber in FSI-PfS-3a. In both test cases the fluctuations of the deflections increase towards the small cone diameter. This indicates that the flow works against the "lock-in" swiveling state of the system. More precisely the vortex shedding frequency naturally rises along the decreasing cone diameter while the attached flexible plate forces an uniform vortex shedding frequency. It is assumed that at the smaller end of the cone the physical coupling between the flow and the structure is eventually more sensitive and leads to the increased variations in the deflections there.
Since the three-dimensional vorticies (existence proven by three-dimensional flow measurements) are generated by the effect of the three-dimensional geometry of the bluff body, the instability-induced excitation (IIE) is assumed to be responsible for the FSI coupling in both configurations. The main instability source is determined to be the vortex shedding. The limitation to the first swiveling mode and the moderate deflections in the range of the local cone diameter are not able to alter the system coupling. Thus, the movement-induced excitation (MIE) state does not appear. The investigations concerning FSI-PfS-3a are published in Kalmbach et al. (2013).

Results of FSI-PfS-4x

The last test cases FSI-PfS-4x are developed with respect to an application-oriented FSI benchmark. In the two cases considered the flexible structure is a long, thin polyethylene cylinder which is exposed to a free-stream flow (FSI-PfS-4a) and a disturbed flow within a 3×3 cylinder arrangement (FSI-PfS-4b). Both configurations show a strong dependence on the inflow velocity. Due to the different configurations both test cases show individual structural responses to the increasing inflow velocities. FSI-PfS-4a is characterized by large fluctuations of the structural deflections for low inflow velocities. By passing a critical inflow velocity the structural motion gets more stable and its response (two pair (2P) vortex shedding mode) is comparable to experimental investigations carried out in the literature referring to elastically mounted cylinders. In this mode the motion of the structure causes the shedding of four alternately rotating vorticies within a period. In FSI-PfS-4a this 2P flow state is characterized by

large quasi-periodic deflections of the cylinder tip slightly smaller than one cylinder diameter in y-direction ($y/d \approx \pm 0.9$) and very large deflections in x-direction ($2.8 < x/d < 3.9$) while the swiveling frequency is of the order of 30 Hz.
The same flexible cylinder applied in FSI-PfS-4a is surrounded by eight rigid cylinders in a 3×3 arrangement in the second test case FSI-PfS-4b. In comparison to the free-stream case of FSI-PfS-4a the additional structures nearby reveal a strong influence on the structural behavior of the elastic cylinder. Especially for higher inflow velocities the structural response is quasi-periodic with large deflections in x- ($2.3 < x/d < 3.0$) and y-direction ($-1.3 < x/d < 1.3$) with a swiveling frequency of about 26 Hz. For the detailed investigations at the inflow velocity $u_{\text{inflow}} = 1.69$ m/s the motion path of the cylinder tip is described by a distorted eight in FSI-PfS-4a, while the response in FSI-PfS-4b forms an open "C". According to the high oscillation frequencies of the cylinder in the order of 30 Hz and the associated large accelerations and velocities in both physical domains and both test configurations, the phase-averaged flow field measurements provide only a limited insight into the underlying physics of the system.
The classification into the excitation mechanisms is rather difficult. For lower inflow velocities the EIE and the IIE modes are assumed to be present. The EIE is characterized by a broad frequency spectrum and tiny deflections related to the low turbulent fluctuations present in the inflow. At higher inflow velocities the structural deformation increases and the mode transition from EIE to IIE takes place. Here, the flow is strongly influenced by the motion of the flexible cylinder indicating the MIE mode. However, the instability of the vortex shedding is still present and mainly controls the swiveling behavior of the system. Therefore, it can be assumed that a simultaneous excitation of IIE and MIE is present for higher inflow velocities. In FSI-PfS-4b the onset of FSI also refers to the EIE mode. In contrast to FSI-PfS-4a the velocity fluctuations at the inflow are assumed to be less responsible for the weak structural oscillations present for low inflow velocities. Here, the extraneous excitation due to the surrounding cylinders causing stronger flow fluctuations are assumed as the main excitation source in this system state present over a broad range of inflow velocities. Similar to FSI-PfS-4a a mode transition from EIE to IIE takes place. For a further increase of the inflow velocities the excitation modes IIE and MIE are assumed to be present simultaneously.

Results of the coupled CFD/CSD predictions

The numerical predictions using ANSYS® lead to satisfactory results for the two-dimensional test cases (FSI-PfS-1x and 2x) and less reasonable results for the three-dimensional test configurations (FSI-PfS-3x and 4x). The predictions reproduce the experiments with minor errors (errors between 3% and 8% for the y-displacements and errors between 5% and 8% for the swiveling frequency) of each test case of FSI-PfS-1x. Both, the structural deformations and the flow field (including the characteristic flow phenomena, i.e., the acceleration areas on the upper and lower side of the cylinder, the stagnation point in front of the cylinder, the wake area past the cylinder and the shear layers on both sides of the structure) are well predicted in size and location compared with the experimental results. Similar findings are observed for the predictions of FSI-PfS-2x. Since the different configuration of FSI-PfS-2x compared to

FSI-PfS-1x allows large structural deflections, a special concern is put on the deformation of the two-dimensional block-structured mesh. For FSI-PfS-2a only minor errors lower than 6% for the structural deflections and the swiveling frequency compared to the experimental data are found. In the case of FSI-PfS-2b the additional rotational degree of freedom of the front cylinder increases the complexity of the prediction. Once again the large deflections require an effective mesh deformation and a special concern on the coupling conditions. Here, a larger number of coupling iterations is necessary to converge the solution taking the more complex physics of this test case into account. Compared to the experimental data an error of 11% for the y-displacements and an error of 6% for the swiveling frequency is achieved.
The predictions of the three-dimensional test cases FSI-PfS-3x reveal major problems in the modeling of the coupled system. According to the experimental results a three-dimensional deformation behavior of the flexible plate is present in both test cases. That means that the lateral sides of the rubber plate tend to its center and leave their initial z-plane. However, in the predictions the lateral sides of the rubber plate are bound to a fixed geometry of the structural domain. Therefore, a displacement in z-direction may generate an unphysical/undefined space in the fluid domain. Since this issue could not be solved in the present work, a large mismatch to the structural results of the experiments is found. Here, mismatches regarding the displacements, the swiveling mode and the corresponding phase delays of the flexible plate are observed.
In the computations of FSI-PfS-4x several major problems appear leading to an unsuccessful validation of FSI-PfS-4a and a completely failed prediction of FSI-PfS-4b. In the case of the single cylinder in FSI-PfS-4a a qualitative agreement with the experimental results is achieved for the cylinder trajectory (distorted "8"). However, large quantitative disagreements are found in the structural deflection of the cylinder tip. Here, the y-deflections are strongly over-predicted (+44%) while the x-deflections are strongly under-predicted (−36%). Several reasons are assumed to be responsible for the mismatch (see Table 28). The largest influence is assigned to the coarse computational grid applied in the predictions. Furthermore, velocity-related material effects like softening or hardening are not considered in the present material model. These effects are present in FSI-PfS-4x as indicated by the experimental results discussed in Section 10.1.3.
Related to the same issues the computation of the flow around the flexible cylinder within the 3×3 cylinder arrangement in FSI-PfS-4b failed completely. Here, the coarse computational grid and the improper material behavior lead to a strong over-prediction of the structural deflections of the cylinder tip. This results in a contact of the flexible cylinder with the rigid cylinder located downstream and aborted the computation.

In summary, this thesis carried out an extensive experimental investigation concerning several FSI-benchmark configurations in the turbulent flow regime. While the first test cases FSI-PfS-1x are rather simple to predict, the simulations of the test cases FSI-PfS-2x, 3x and 4x are more difficult due to their increased physical complexity. Despite, the failed numerical predictions of the three-dimensional test cases, the main objectives of this thesis are accomplished.

11.2. Outlook

The problems regarding the predictions of the three-dimensional test cases would be a reasonable topic for further numerical studies. Especially, the issues of the artificially introduced strains caused by the applied problematic boundary conditions concerning the test cases FSI-PfS-3x require a deeper analysis. Since in this thesis a rather classical implicit coupling algorithm based on the finite-volume method is applied, a further reproduction using other FSI approaches like the immersed boundary method or the Lattice Boltzmann method are considerable. Maybe these approaches help to decrease the high computational costs of FSI predictions by reducing the time for remeshing or by distributing the FSI computations to a large amount of processing units (e.g, GPUs[23]).

Regarding the test cases itself several other variations of the presented configurations are possible. Since FSI simulations become more and more popular for industrial applications, more application-oriented test cases are reasonable. Especially, the offshore industry developing offshore wind turbines are highly interested in computational methods for predicting the interaction of oscillating flows (e.g., periodic waves or tidal conditions) and the fundament of offshore structures.

While application-based test cases often are not of simple geometry, eventually other measurement techniques have to be applied. For a higher precision regarding three-dimensional structural deformations a stereoscopic high-speed camera system would provide an enormous benefit in spatial and temporal resolution in comparison to the LLT measurement technique applied in this thesis. However, measurement techniques with high temporal resolution are always limited concerning the recording time and often very expensive. Here, further enhancements in data storage and the increasing demand of high-speed action cameras in the customer market will more easily allow the scientific usage of this technique in the future. Similar approaches are considerable for the flow measurement techniques, especially for three-dimensional systems like the V3V system.

[23]GPU, graphical processing unit, provides strong abilities in parallel processing by using large numbers of processing cores (often > 100).

References

Adrian, R., 2005. Twenty years of particle-image velocimetry. Experiments in Fluids 39 (2), 159–169.

Adrian, R. J., 1984. Scattering particle characteristics and their effect on pulsed laser measurements of fluid flow: Speckle velocimetry vs. particle-image velocimetry. Appl. Opt. 23 (11), 1690–1691.

Adrian, R. J., 1991. Particle-imaging techniques for experimental fluid mechanics. Annual Review of Fluid Mechanics 23 (1), 261–304.

Amann, M. C., Bosch, T., Myllyla, R., Rioux, M., Lescure, M., 2001. Laser ranging: A critical review of usual techniques for distance measurement. Optical Engineering 40 (1), 10–19.

Amatya, D., Troolin, D., Longmire, E., 2009. 3D3C velocity measurements downstream of artificial heart valves. In: 8th Int. Symp. on Particle-Image Velocimetry - PIV09, Melboune, Australia, August 25–28, 2009.

Anderson, E., Szewczyk, A., 1997. Effects of a splitter plate on the near wake of a circular cylinder in 2 and 3-dimensional flow configurations. Experiments in Fluids 23 (2), 161–174.

ANSYS, 2011a. ANSYS CFX Theory Guide, Release 14.0.

ANSYS, 2011b. ANSYS System Coupling User's Guide, Release 14.0.

ANSYS, 2011c. Theory Reference for the Mechanical ANSYS Parametric Design Language (APDL) and Mechanical Applications, Release 14.0.

Apelt, C. J., West, G. S., 1975. The effects of wake splitter plates on bluff-body flow in the range $10^4 <$ Re$< 5 \times 10^4$. part 2. Journal of Fluid Mechanics 71 (01), 145–160.

Balint, T. S., Lucey, A. D., 2005. Instability of a cantilevered flexible plate in viscous channel flow. Journal of Fluids and Structures 20 (7), 893 – 912.

Barker, D. B., Fourney, M. E., 1977. Measuring fluid velocities with speckle patterns. Opt. Lett. 1 (4), 135–137.

Barth, T., Jesperson, D., 1989. The design and application of upwind schemes on unstructured meshes. AIAA Journal 89 (0366).

Bathe, K., Zhang, H., Ji, S., 1999. Finite-element analysis of fluid flows fully coupled with structural interactions. Computers & Structures 72 (1), 1–16.

Berkovic, G., Shafir, E., 2012. Optical methods for distance and displacement measurements. Adv. Opt. Photon. 4 (4), 441–471.

Blasius, H., 1908. Grenzschichten in Flüssigkeiten mit kleiner Reibung. Z. Math. Phys 56, 1–37.

Blevins, R. D., 1990. Flow-induced vibration. New York, NY (USA), Van Nostrand Reinhold Co., Inc.

Bouffard, J., Cabana, A., Chaouki, J., Bertrand, F., 2013. Experimental investigation of the effect of particle cohesion on the flow dynamics in a spheronizer. AIChE Journal 59, 1491–1501.

Breuer, M., 2002. Direkte Numerische Simulation und Large-Eddy Simulation turbulenter Strömungen auf Hochleistungsrechnern. Habilitationsschrift, Universität Erlangen–Nürnberg, Berichte aus der Strömungstechnik. Shaker Verlag, Aachen.

Breuer, M., 2013. Numerische Strömungsmechanik - Vorlesungsskript. Helmut-Schmidt Universität, Hamburg.

Breuer, M., De Nayer, G., Münsch, M., Gallinger, T., Wüchner, R., 2012. Fluid-structure interaction using a partitioned semi-implicit predictor-corrector coupling scheme for the application of large-eddy simulation. Journal of Fluids and Structures 29, 107–130.

Breuer, M., Kalmbach, A., 2011. Experimental investigations on fluid-structure interactions based on particle-image velocimetry. In: Thess, A., Resagk, C., Ruck, B., Leder, A., Dopheide, D. (Eds.), Proc. der 19. Gala–Fachtagung 'Lasermethoden in der Strömungsmesstechnik', Sept. 6–8, 2011. Universität Ilmenau, Germany, pp. 35–1–35–8.

Bungartz, H.-J., Mehl, M., Schäfer, M. (Eds.), 2010. Fluid-Structure Interaction II: Modeling, Simulation, Optimization. Vol. 73 of Lecture Notes in Computational Science and Engineering, LNCSE. Springer, Heidelberg.

Bungartz, H.-J., Schäfer, M. (Eds.), 2006. Fluid-Structure Interaction: Modeling, Simulation, Optimization. Vol. 53 of Lecture Notes in Computational Science and Engineering, LNCSE. Springer, Heidelberg.

Bunge, U., Gurr, A., Thiele, F., 2003. Numerical aspects of simulating the flow-induced oscillations of a rectangular bluff body. Journal of Fluids and Structures 18 (34), 405 – 424.

Cadafalch, J., Oliva, A., Perez-Segarra, C., Costa, M., Salom, J., 1999. Comparative study of conservative and nonconservative interpolation schemes for the domain decomposition method on laminar incompressible flows. Numerical Heat Transfer, Part B: Fundamentals 35 (1), 65–84.

Cantwell, B., Coles, D., 1983. An experimental study of entrainment and transport in the turbulent near wake of a circular cylinder. Journal of Fluid Mechanics 136 (1), 321–374.

Castigliano, C., 1879. Thorie de l'quilibre des systmes lastiques et ses applications.

Chang, C., Kumar, R., Bernitsas, M., 2011. VIV and galloping of single circular cylinder with surface roughness. Ocean Engineering 38 (16), 1713 – 1732.

Chaplin, J. R., Bearman, P. W., Cheng, Y., Fontaine, E., Graham, J. M. R., Herfjord, K., Huera Huarte, F. J., Isherwood, M., Lambrakos, K., Larsen, C. M., Menegheni, J. R., Moe, G., Pattenden, R. J., Triantafyllou, M. S., Willden, R. H. J., 2005a. Blind predictions of laboratory measurements of vortex-induced vibrations of a tension riser. Journal of Fluids and Structures 21, 25–40.

Chaplin, J. R., Bearman, P. W., Huera Huarte, F. J., Pattenden, R. J., 2005b. Laboratory measurements of vortex-induced vibrations of a vertical tension riser in a stepped current. Journal of Fluids and Structures 21, 3–24.

Cierpka, C., 2007. Zeitaufgelöste PIV-Untersuchungen zur Strömungskontrolle mittels elektromagnetischer Kräfte in schwach leitfähigen Fluiden. Ph.D. thesis, Forschungszentrum Dresden, Germany.

Clarke, T. A., Grattan, K. T. V., Lindsey, N. E., 1991. Laser-based triangulation techniques in optical inspection of industrial structures. Proc. SPIE 1332, 474–486.

De Nayer, G., Breuer, M., 2014. Numerical FSI investigation based on LES: Flow past a cylinder with a flexible splitter plate involving large deformations (FSI-PfS-2a). Int. Journal of Heat and Fluid Flow 50, 300–315.

De Nayer, G., Breuer, M., Kalmbach, A., 2012. Fluid-structure interaction in turbulent flows: LES predictions and PIV measurements. In: Eberhardsteiner, J., Böhm, H., Rammerstorfer, F. (Eds.), Proc. of the 6th European Congress on Computational Methods in Applied Sciences and Engineering (ECCOMAS 2012), Sept. 10–14, 2012. Vienna University of Technology, Austria.

De Nayer, G., Kalmbach, A., Breuer, M., Sicklinger, S., Wüchner, R., 2014. Flow past a cylinder with a flexible splitter plate: A complementary experimental-numerical investigation and a new FSI test case (FSI-PfS-1a). Int. Journal of Computer and Fluids 99, 18–43.

Degroote, J., Bathe, K., Vierendeels, J., 2009. Performance of a new partitioned procedure versus a monolithic procedure in fluid-structure interaction. Computers and Structures 87, 793–801.

Degroote, J., Bruggeman, P., Haelterman, R., Vierendeels, J., 2008. Stability of a coupling technique for partitioned solvers in FSI applications. Computers and Structures 86 (23–24), 2224–2234.

Demirdžić, I., Perić, M., 1988. Space conservation law in finite-volume calculations of fluid flow. International Journal for Numerical Methods in Fluids 8 (9), 1037–1050.

Demirdžić, I., Perić, M., 1990. Finite volume method for prediction of fluid flow in arbitrarily shaped domains with moving boundaries. International Journal for Numerical Methods in Fluids 10 (7), 771–790.

Dhopade, P., Neely, A., Young, J., 2010. Fluid-structure interaction of gas turbine blades. In: 17th Int. Australasian Fluid Mechanics Conference, Auckland, Australia, December 5–9, 2010.

Dorsch, R. G., Häusler, G., Herrmann, J. M., 1994. Laser triangulation: Fundamental uncertainty in distance measurement. Appl. Opt. 33 (7), 1306–1314.

Dudderar, T. D., Simpkins, P. G., 1977. Laser speckle photography in a fluid medium. Nature (270(5632)), 45–47.

Dütsch, H., Durst, F., Becker, S., Lienhart, H., 1998. Low-Reynolds-number flow around an oscillating circular cylinder at low Keulegan-Carpenter numbers. Journal of Fluid Mechanics 360, 249–271.

Farhat, C., Geuzaine, P., Grandmont, C., 2001. The discrete geometric conservation law and the non-linear stability of ALE schemes for the solution of flow problems on moving grids. Journal of Computational Physics 174 (2), 669–694.

Farhat, C., van der Zee, K. G., Geuzaine, P., 2006. Provably second-order time-accurate loosely-coupled solution algorithms for transient non-linear computational aeroelasticity. Computer Methods in Applied Mechanics and Engineering 195 (17-18), 1973–2001.

Ferziger, J., Peric, M., 2002. Computational Methods for Fluid Dynamics, 3rd Edition. Springer.

Formaggia, L., Gerbeau, J. F., Nobile, F., Quarteroni, A., 2001. On the coupling of 3D and 1D Navier-Stokes equations for flow problems in compliant vessels. Computer Methods in Applied Mechanics and Engineering 191 (6-7), 561–582.

Förster, C., 2007. Robust methods for fluid-structure interaction with stabilised finite elements. Ph.D. thesis, Department of Construction Analysis, University Stuttgart, Germany.

Förster, C., Wall, W. A., Ramm, E., 2007. Artificial added mass instabilities in sequential staggered coupling of non-linear structures and incompressible viscous flows. Computer Methods in Applied Mechanics and Engineering 196 (7), 1278–1293.

Fujarra, A., Pesce, C., Flemming, F., Williamson, C., 2001. Vortex-induced vibration of a flexible cantilever. Journal of Fluids and Structures 15 (3-4), 651–658.

Fukunaga, K., 1990. Introduction to Statistical Pattern Recognition. Academic Press.

Gauss, C., 1821, 1823, 1826. Theoria combinationis observationum erroribus minimis obnoxiae; Translation: Three essays concerning the calculation of probabilities as the basis of the Gaussian law of error propagation‘ by Stewart, G. W. 1987.

Geller, S., Kollmannsberger, S., Bettah, M., Krafczyk, M., Scholz, D., Düster, A., Rank, E., 2010. An explicit model for three-dimensional fluid-structure interaction using LBM and p-FEM. In: Bungartz, H.-J., Mehl, M., Schäfer, M. (Eds.), Fluid-Structure Interaction

II. Vol. 73 of Lecture Notes in Computational Science and Engineering. Springer Berlin Heidelberg, pp. 285–325.

Glück, M., Breuer, M., Durst, F., Halfmann, A., Rank, E., 2001. Computation of fluid-structure interaction on lightweight structures. Journal of Wind Engineering and Industrial Aerodynamics 89 (14-15), 1351–1368.

Gomes, J. P., 2012. Fluid-structure interaction-induced oscillation of flexible structures in uniform flows. Ph.D. thesis, Lehrstuhl für Strömungsmechanik, Universität Erlangen-Nürnberg, Germany.

Gomes, J. P., Lienhart, H., 2006. Experimental study on a fluid-structure interaction reference test case. In: Bungartz, H.-J., Schäfer, M. (Eds.), Fluid-Structure Interaction – Modelling, Simulation, Optimization. Vol. 53 of Lecture Notes in Computational Science and Engineering, LNCSE. Springer, Heidelberg, pp. 356–370.

Gomes, J. P., Lienhart, H., 2010. Experimental benchmark: Self-excited fluid-structure interaction test cases. In: Bungartz, H.-J., Mehl, M., Schäfer, M. (Eds.), Fluid-Structure Interaction II – Modelling, Simulation, Optimization. Vol. 73 of Lecture Notes in Computational Science and Engineering, LNCSE. Springer, Heidelberg, pp. 383–411.

Gomes, J. P., Lienhart, H., 2013. Fluid-structure interaction-induced oscillation of flexible structures in laminar and turbulent flows. Journal of Fluid Mechanics 715, 537–572.

Gomes, J. P., Münsch, M., Breuer, M., Lienhart, H., 2010. Flow-induced oscillation of a flat plate – A fluid-structure interaction study using experiment and LES. In: Dillmann, A., Heller, G., Klaas, M., Kreplin, H., Nitsche, W., Schröder, W. (Eds.), New Results in Numerical and Experimental Fluid Mechanics VII, Contr. to the 16. STAB/DGLR Symposium, Nov. 3–5, 2008, Aachen, Germany. Vol. 112 of Notes on Numerical Fluid Mechanics and Multidisciplinary Design. Springer, Heidelberg, pp. 347–354.

Gomes, J. P., Yigit, S., Lienhart, H., Schäfer, M., 2011. Experimental and numerical study on a laminar fluid-structure interaction reference test case. Journal of Fluids and Structures 27 (1), 43–61.

Goyder, H., 2002. Flow-induced vibration in heat exchangers. Chemical Engineering Research and Design 80 (3), 226–232.

Hall, J., 2006. Problems encountered from the use (or misuse) of Rayleigh damping. Earthquake Engineering & Structural Dynamics 35 (5), 525–545.

Heil, M., 2004. An efficient solver for the fully coupled solution of large-displacement fluid-structure interaction problems. Computer Methods in Applied Mechanics and Engineering 193 (1-2), 1–23.

Hill, D., Troolin, D., Walters, G., Lai, W., Sharp, K., 2008. Volumetric 3-component velocimetry (V3V) measurements of the turbulent flow in stirred tank reactors. In: 14th Int. Symp. on Appl. Laser Techniques to Fluid Mechanics, Lisbon, Portugal, July 7–10, 2008.

Hinsch, K. D., 2002. Holographic particle-image velocimetry. Meas. Sci. Technol. 13, R61–R72.

Hsiao, F., Chiang, C., 1998. Experimental study of cellular shedding vortices behind a tapered circular cylinder. Experimental Thermal and Fluid Science 17, 179–188.

Hsiao, F., Pan, J., Chiang, C., 1993. The study of vortex shedding frequencies behind tapered circular cylinders. ASME-Publications-PVP 245, 103–103.

Hübner, B., Seidel, U., 2007. Partitioned solution to strongly coupled hydroelastic systems arising in hydro turbine design. In: 2nd IAHR Int. Meeting of the Workgroup on Cavitation and Dynamic Problems in Hydraulic Machinery and Systems, Timisoara, Romania, October 24–26, 2007.

Hübner, B., Walhorn, E., Dinkler, D., 2004. A monolithic approach to fluid-structure interaction using space-time finite elements. Computer Methods in Applied Mechanics and Engineering 193 (23-26), 2087–2104.

Ikenouchi, M., Kakuno, T., Inoue, H., Sato, T., 1982. Fundamental investigation on wind resistant design of bridges. Mitsui Zosen Technical Review 116, 31–38.

Jagadeesh, C., 2009. Dynamics of vortex shedding from slender cones. Ph.D. thesis, Queen Mary University of London.

Jansen, K., Shakib, F., Hughes, T., 1992. Fast projection algorithm for unstructured meshes. In: Atluri, S. (Ed.), Computational Nonlinear Mechanics in Aerospace Engineering. AIAA. AIAA.

Jeong, J., Hussain, F., 1995. On the identification of a vortex. Journal of Fluid Mechanics 285, 69–94.

Jones, W. P., Launder, B. E., 1972. The prediction of laminarization with a two-equation model of turbulence. International Journal of Heat and Mass Transfer 15 (2), 301–314.

Kabinejadian, F., Leo, H., Danpinid, A., Cui, F., Zhang, Z., Ho, P., 2013. Particle image velocimetry (PIV) flow measurements of carotid artery bifurcation with application to a novel covered carotid stent design. In: Long, M. (Ed.), World Congress on Medical Physics and Biomedical Engineering May 26-31, 2012, Beijing, China. Vol. 39 of IFMBE Proceedings. Springer Berlin Heidelberg, pp. 1441–1444.

Kalmbach, A., Breuer, M., 2012. Investigations on fluid-structure interactions using volumetric particle-image velocimetry. In: Proc. of 16th Int. Symp. on Applications of Laser Techniques to Fluid Mechanics, July. 9–12, 2012, Lisbon, Portugal.

Kalmbach, A., Breuer, M., 2013a. Complementary experimental and numerical investigations on a new vortex-induced fluid-structure interaction benchmark (FSI-PfS-2a). In: Proc. of ANSYS Conference and CADFEM Users Meeting (ACUM 2013), Mannheim, Germany 19–21 June.

Kalmbach, A., Breuer, M., 2013b. Experimental PIV/V3V measurements of vortex-induced fluid-structure interaction in turbulent flow - A new benchmark FSI-PfS-2a. Journal of Fluids and Structures 42, 369–387.

Kalmbach, A., De Nayer, G., Breuer, M., 2013. A new turbulent three-dimensional FSI benchmark FSI-PfS-3a: Definition and measurements. In: Proc. of 5th Conf. on Computational Methods in Marine Engineering (MARINE 2013), Hamburg, Germany, 29–31 May.

Kaminsky, R., Dumont, K., Weber, H., Schroll, M., Verdonck, P., 2007. PIV validation of blood-heart valve leaflet interaction modelling. Int. J. Artif. Organs 30 (7), 640–648.

Kästner, M., Obst, M., Brummund, J., Thielsch, K., Ulbricht, V., 2012. Inelastic material behavior of polymers: Experimental characterization, formulation and implementation of a material model. Mechanics of Materials 52, 40–57.

Khalak, A., Williamson, C., 1996. Dynamics of a hydroelastic cylinder with very low mass and damping. Journal of Fluids and Structures 10, 455–492.

Klimanov, M. M., 2009. Triangulating laser system for measurements and inspection of turbine blades. Measurement Techniques 52 (7), 725–731.

Koci, L., Milovanovi, G., 1997. Shape preserving approximations by polynomials and splines. Computers & Mathematics with Applications 33 (11), 59–97.

Kompenhans, J., Raffel, M., Dieterle, L., Dewhirst, T., Vollmers, H., Ehrenfried, K., Willert, C., Pengel, K., Kähler, C., Schröder, A., Ronneberger, O., 2000. Particle-image velocimetry in aerodynamics: Technology and applications in wind tunnels. Journal of Visualization 2 (3-4), 229–244.

Krätzig, W., Meskouris, K., Link, M., 1996. Der Ingenieurbau, Baustatik, Baudynamik. Ernst & Sohn Verlag, Berlin, Ch. Baudynamik und Systemidentifikation, pp. 365–518.

Kuethe, A., Schetzer, J., 1959. Foundations of Aerodynamics, 2nd Edition. John Wiley & Sons, New York.

Küttler, U., Wall, W. A., 2009. Vector extrapolation for strong coupling fluid-structure interaction solvers. Journal of Applied Mechanics 76, 021205.1–021205.7.

Lammering, R., 2011. Technische Mechanik - Vorlesungsskript. Helmut-Schmidt Universität, Hamburg.

Launder, B., Spalding, D., 1974. The numerical computation of turbulent flows. Computer Methods in Applied Mechanics and Engineering 3 (2), 269–289.

Lee, H., Lee, T., Chang, Y., 2013. Numerical simulation of flow-induced bi-directional oscillations. Journal of Fluids and Structures 37, 220–231.

Lee, J., Shin, J., SangHwan, L., 2012. Fluid-structure interaction of a flapping flexible plate in quiescent fluid. Computers & Fluids 57, 124–137.

Lee, J., You, D., 2013. Study of vortex-shedding-induced vibration of a flexible splitter plate behind a cylinder. Physics of Fluids 25, 11081–1–11081–17.

Lesoinne, M., Farhat, C., 1996. Geometric conservation laws for flow problems with moving boundaries and deformable meshes, and their impact on aeroelastic computations. Computer Methods in Applied Mechanics and Engineering 134 (1), 71–90.

Liu, H., Zhang, S., Kathiresan, R., Kobayashi, T., Lee, C., 2012. Development of piezoelectric microcantilever flow sensor with wind-driven energy harvesting capability. Applied Physics Letters 100 (22), 223905–1–223905–3.

Löhner, R., Yang, C., 1996. Improved ALE mesh velocities for moving bodies. Communications in Numerical Methods in Engineering 12 (10), 599–608.

Lumley, J., 1981. Coherent structures in turbulence. In: Transition and Turbulence. Vol. 1. pp. 215–242.

Melling, A., 1997. Tracer particles and seeding for particle-image velocimetry. Measurement Science and Technology 8 (12), 1406–1416.

Menter, F., 1992. Influence of freestream values on k-ω turbulence model predictions. AIAA Journal 30 (6), 1657–1659.

Menter, F., 1993. Zonal two-equation k-ω turbulence model for aerodynamic flows. AIAA Journal 29 (6), 1598–1605.

Menter, F., Sharkey, P., Yakubov, S., Kuntz, M., 2006. Overview of fluid-structure coupling in ANSYS-CFX. In: 25th Int. Conf. on Offshore Mechanics and Arctic Engineering, Volume 4: Terry Jones Pipeline Technology; Ocean Space Utilization; CFD and VIV Symposium, Hamburg, Germany, June 4–9, 2006.

Menter, F. R., 1994. Two-equation eddy-viscosity turbulence models for engineering applications. AIAA Journal 32 (8), 269–289.

Menter, F. R., Kuntz, M., Langtry, R., 2003. Ten years of industrial experience with the SST turbulence model. International Journal of Heat and Mass Transfer 4, 625–632.

micro Epsilon, 2013. scanCONTROL 2D/3D laser scanner (laser profile sensors) - technical details.

Mie, G., 1908. Beiträge zur Optik trueber Medien, speziell kolloidaler Metallösungen. Annalen der Physik 25 (03), 377–445.

Mok, D. P., 2001. Partitionierte Lösungsansätze in der Strukturdynamik und der Fluid-Struktur-Interaktion. Ph.D. thesis, Institut für Baustatik, Universität Stuttgart, Germany.

Moretti, P. M., 1993. Flow-induced vibrations in arrays of cylinders. Annual Review of Fluid Mechanics 25 (1), 99–114.

Narasimhamurthy, V., Andersson, H., Pettersen, B., 2009. Cellular vortex shedding behind a tapered circular cylinder. Physics of Fluids 21, 044106.1 – 044106.12.

Nasdala, L., 2010. FEM-Formelsammlung Statik und Dynamik: Hintergrundinformationen, Tipps Und Tricks. Vieweg + Teubner Verlag, Wiesbaden.

Naudascher, E., Rockwell, D., 1994. Flow-induced Vibrations: An Engineering Guide. AA Balkema, Rotterdam, Holland.

Nobile, F., 2001. Numerical approximation of fluid-structure interaction problems with application to haemodynamics. Ph.D. thesis, Ecole Polytechnique Féderale de Lausanne, Switzerland.

Oertel, H., Ruck, S., 2012. Bioströmungsmechanik. Vieweg+Teubner Verlag, Wiesbaden.

Ohmi, K., Li, H. Y., 2000. Particle tracking velocimetry with new algorithms. Meas. Sci. Technol 11, 603–616.

Okamoto, K., Nishio, S., Saga, T., Kobayashi, T., 2000. Standard images for particle-image velocimetry. Measurement Science and Technology 11 (6), 685–691.

Özcan, M., 2011. Determining seam profile tracking of very narrow butt welding on sheet metal. Scientific Research and Essays 6 (23), 5040–5048.

Païdoussis, M., 2006. Real-life experiences with flow-induced vibration. Journal of Fluids and Structures 22 (6-7), 741–755.

Païdoussis, M., Li, G., 1992. Cross-flow-induced chaotic vibrations of heat-exchanger tubes impacting on loose supports. Journal of Sound and Vibration 152 (2), 305–326.

Palma, J., Silva Lopez, A., 2007. Advances in Turbulence XI. Springer Proceedings in Physics, Heidelberg.

Parisch, H., 2012. Festkörperkontinuumsmechanik. Vieweg+Teubner Verlag, Wiesbaden.

Pereira, F., Gharib, M., 2002. Defocusing digital particle-image velocimetry and the three-dimensional characterization of two-phase flows. Meas. Sci. Technol 13, 683–694.

Pereira, F., Stuer, H., Graff, E. C., Gharib, M., 2006. Two-frame 3D particle tracking. Meas. Sci. Technol. 17, 1680–1692.

Pesce, C., Fujarra, A., 2002. Vortex-induced vibrations experiments with an elastically mounted cylinder in water. In: 12th Int. Offshore and Polar Engineering Conf., Kitakyushu, Japan, May 26-31. The International Society of Offshore and Polar Engineers, pp. 502–509.

Piccirillo, P., van Atta, C., 1993. An experimental study of vortex shedding behind linearly tapered cylinders at low Reynolds number. Journal of Fluid Mechanics 246, 163–195.

Pickering, C. J. D., Halliwell, N. A., Sep 1984. Laser speckle photography and particle-image velocimetry: photographic film noise. Appl. Opt. 23 (17), 2961–2969.

Raffel, M., Willert, C., Kompenhans, J., 1998. Particle-Image Velocimetry, A Practical Guide. Springer Verlag, Berlin, Heidelberg.

Rayleigh, L., 1877. Theory of Sound. Dover Publications, New York.

Reddy, J., 2004. Introduction to the Finite-Element Method. Mcgraw-Hill.

Reynolds, W. C., Hussain, A., 1972. The mechanics of an organized wave in turbulent shear flow. Part 3. Theoretical models and comparisons with experiments. Journal of Fluid Mechanics 54 (2), 263–288.

Robertson, I., Sherwin, S., 1999. Free-surface flow simulation using hp-spectral elements. Journal of Computational Physics 155 (1), 26–53.

Santiago, J. G., Wereley, S. T., Meinhart, C. D., Beebe, D. J., Adrian, R. J., 1998. A particle-image velocimetry system for microfluidics. Experiments in Fluids 25 (4), 316–319.

Scarano, F., 2013. Tomographic PIV: Principles and practice. Meas. Sci. Technol. 24, 1–28.

Schäfer, M., Sternel, D., Becker, G., Pironkov, P., 2010. Efficient numerical simulation and optimization of fluid-structure interaction. In: Bungartz, H.-J., Mehl, M., Schäfer, M. (Eds.), Fluid-Structure Interaction II. Vol. 73 of Lecture Notes in Computational Science and Engineering. Springer Berlin Heidelberg, pp. 131–158.

Schäfer, M., Turek, S., Durst, F., Krause, E., Rannacher, R., 1996. Benchmark computations of laminar flow around a cylinder. In: Hirschel, E. (Ed.), Flow Simulation with High-Performance Computers II. Vol. 48 of Notes on Numerical Fluid Mechanics (NNFM). Vieweg+Teubner Verlag, pp. 547–566.

Schildhauer, M., 2011. Simulation von Fluid-Struktur-Interaktion mit ANSYS-CFX. Master's thesis, Fakultät Maschinen- und Energietechnik, Hochschule für Technik, Wirtschaft und Kultur Leipzig, Germany.

Schlichting, H., Gersten, K., 2004. Boundary-Layer Theory, 8th Edition. Springer, Berlin, Heidelberg.

Shinde, V., Marcel, T., Hoarau, Y., Deloze, T., Harran, G., Baj, F., Cardolaccia, J., Magnaud, J., Longatte, E., Braza, M., 2014. Numerical simulation of the fluid-structure interaction in a tube array under cross-flow at moderate and high Reynolds number. Journal of Fluids and Structures 47 (0), 99 – 113.

Shinohara, K., Sugii, Y., Aota, A., Hibara, A., Tokeshi, M., Kitamori, T., Okamoto, K., 2004. High-speed micro-PIV measurements of transient flow in microfluidic devices. Measurement Science and Technology 15 (10), 1965–1970.

Sieber, G., 2001. Numerical simulation of fluid-structure interaction using loose coupling methods. Ph.D. thesis, Department of numerical methods in mechanical engineering, Technical University Darmstadt, Germany.

Siegel, S., Cohen, K., Seidel, J., McLaughlin, T., 2007. State estimation of transient flow fields using double proper orthogonal decomposition (DPOD). In: King, R. (Ed.), Active Flow Control. Vol. 95 of Notes on Numerical Fluid Mechanics and Multidisciplinary Design (NNFM). Springer Berlin Heidelberg, pp. 105–118.

Sirovich, L., 1987. Turbulence and the dynamics of coherent structures. I - Coherent structures. II - Symmetries and transformations. III - Dynamics and scaling. Quart. Appl. Math 45 (1), 561590.

Su, Y., Evans, A. G. R., Brunnschweiler, A., Ensell, G., 2002. Characterization of a highly sensitive ultra-thin piezoresistive silicon cantilever probe and its application in gas flow velocity sensing. Journal of Micromechanics and Microengineering 12 (6), 780.

Teixeira, P., Awruch, A., 2005. Numerical simulation of fluid-structure interaction using the finite-element method. Computers & Fluids 34 (2), 249–273.

Thomas, P., 1992. On the influence of the Basset history force on the motion of a particle through a fluid. Physics of Fluids 4, 2090.

Troolin, D., Longmire, E., 2008. Volumetric 3-component velocity measurements of vortex rings from inclined exits. In: 14th Int. Symp. on Appl. Laser Techniques to Fluid Mechanics, Lisbon, Portugal, July 7–10, 2008.

Tropea, C., Yarin, A., Foss, J., 2007. Handbook of Experimental Fluid Mechanics. Springer Verlag, Berlin / Heidelberg.

TSI, 2007. V3V System - Volumetric 3-Component Flow Measurement and Visualization - Users Guide. Vol. A.

Tucker, P. G., Rumsey, C. L., Spalart, P. R., Bartels, R. B., Biedron, R. T., 2005. Computations of wall distances based on differential equations. AIAA Journal 43 (3), 539–549.

Turek, S., Hron, J., 2006. Proposal for numerical benchmarking of fluid-structure interaction between an elastic object and laminar incompressible flow. In: Bungartz, H.-J., Schäfer, M. (Eds.), Fluid-Structure Interaction. Vol. 53 of Lecture Notes in Computational Science and Engineering, LNCSE. Springer, Heidelberg, pp. 371–385.

Turek, S., Hron, J., Razzaq, M., Wobker, H., Schäfer, M., 2010. Numerical benchmarking of fluid-structure interaction: A comparison of different discretization and solution approaches. In: Bungartz, H.-J., Mehl, M., Schäfer, M. (Eds.), Fluid-Structure Interaction II – Modelling, Simulation, Optimization. Vol. 73 of Lecture Notes in Computational Science and Engineering, LNCSE. Springer, Heidelberg, pp. 413–424.

Vierendeels, J., Degroote, J., Annerel, S., Haelterman, R., 2010. Stability issues in partitioned FSI calculations. In: Bungartz, H.-J., Mehl, M., Schäfer, M. (Eds.), Fluid-Structure Interaction II – Modeling, Simulation, Optimization. Vol. 73 of Lecture Notes in Computational Science and Engineering, LNCSE. Springer, Heidelberg, pp. 83–102.

von Kàrmàn, T., 1930. Mechanische Aehnlichkeit und Turbulenz. Nachrichten von der Gesellschaft der Wissenschaften zu Göttingen, Fachgruppe 1 (Mathematik) 5, 58–76.

Wall, W. A., 1999. Fluid-Struktur-Interaktion mit stabilisierten Finiten Elementen. Ph.D. thesis, Institut für Baustatik, Universität Stuttgart, Germany.

Wall, W. A., Ramm, E., 1998. Fluid-structure interaction based upon a stabilized (ALE) finite element method. IVth World Congress on Computational Mechanics, June 29 - July 2, 1998, Barcelona, Spain.

Wang, X., 1999. Analytical and computational approaches for some structure interaction analyses. Computers and Structures 72, 423–433.

Watanabe, S., Kato, H., 2003. Stereo PIV applications to large-scale low-speed wind tunnels. In: American Institute of Aeronautics and Astronautics, 41st Aerospace Sciences Meeting and Exhibit, Reno, USA. 6-9 January, 2003.

Weaver, D., Fitzpatrick, J., 1988. A review of cross-flow induced vibrations in heat exchanger tube arrays. Journal of Fluids and Structures 2 (1), 73–93.

Webster, D. R., Longmire, E. K., 1998. Vortex rings from cylinders with inclined exits. Physics of Fluids 10 (2), 400–416.

Wilcox, D., 1988. Re-assessment of the scale-determining equation for advanced turbulence models. AIAA Journal 26 (11), 1299–1310.

Willert, C. E., Gharib, M., 1992. Three-dimensional particle-imaging with a single camera. Experiments in Fluids 12, 353–358.

Williamson, C., Govardhan, R., 2004. Low-Reynolds-number flow around an oscillating circular cylinder at low Keulegan-Carpenter numbers. Annu. Rev. Fluid Mech. 36, 413–455.

Wolf, E., Kähler, C., Troolin, D., Kykal, C., Lai, W., 2009. Time-resolved volumetric separation measurement in a towing tank using the TSI-V3V measurement system. In: 8th Int. Symp. on Particle-Image Velocimetry - PIV09, Melboune, Australia, August 25–28, 2009.

Yamamoto, C., Meneghini, J., Saltara, F., Fregonesi, R., Ferrari, J., 2004. Numerical simulations of vortex-induced vibration on flexible cylinders. Journal of Fluids and Structures 19 (4), 467–489.

Yang, H., Xiao, F., 2014. Instability analyses of a top-tensioned riser under combined vortex and multi-frequency parametric excitations. Ocean Engineering 81 (0), 12 – 28.

Zdravkovich, M., 1997. Flow Around Circular Cylinders, volume 1 Edition. Oxford Science Publications, Oxford University Press Inc., New York.

Zhao, M., Kaja, K., Xiang, Y., Yan, G., 2013. Vortex-induced vibration (VIV) of a circular cylinder in combined steady and oscillatory flow. Ocean Engineering 73 (0), 83–95.

Zienkiewicz, O., 1977. The Finite Element Method, 6th Edition. McGraw-Hill.

Lebenslauf

von Andreas Kalmbach, geboren am 12.08.1983 in Oranienburg

Bildungsweg:

04/2009 - 12/2013	Promotionsstudium, Helmut-Schmidt-Universität / Universität der Bundeswehr Hamburg - Professur für Strömungsmechanik "Experimental investigations on vortex-induced fluid-structure interaction benchmarks and corresponding numerical RANS predictions"
04/2008 - 09/2008	Diplomarbeit, Max-Planck-Institut für Dynamik komplexer technischer Systeme, Otto von Guericke Universität, Magdeburg "Experimentelle Charakterisierung der Strömungsverhältnisse in einem Biowave Reaktor"
10/2004 - 09/2008	Studium, Fachhochschule für Technik und Wirtschaft, Berlin Ingenieurswissenschaft, Umweltverfahrenstechnik, Fachbereich 2
08/1996 - 05/2003	Abitur, Marie-Curie-Gymnasium, Hohen Neuendorf

Berufserfahrung:

10/2014 -	Versuchsingenieur, Siemens AG, Berlin
04/2009 - 12/2013	Wissenschaftlicher Mitarbeiter, Professur für Strömungsmechanik der Helmut-Schmidt-Universität / Universität der Bundeswehr Hamburg
10/2006 - 02/2007	Praktikum, LAR Process Analysers AG, Berlin
05/2006 - 04/2008	Studentische Hilfskraft, Fachhochschule für Technik und Wirtschaft, Berlin
07/2004 - 09/2004	Vorpraktikum, A & B Maschinen- & Anlagenprojektierung GmbH, Berlin
06/2003 - 03/2004	Grundwehrdienst, Sanitätsregiment 32, Leitsanitätszentrum 320, Weißenfels